Synthesis of Helical van der Waals Crystals with Tunable Twist

By

Yin Liu

A dissertation submitted in partial satisfaction of the

requirements for the degree of

Doctor of Philosophy

in

Engineering – Materials Science and Engineering

in the

Graduate Division

of the

University of the California, Berkeley

Committee in charge:

Professor Jie Yao, Chair

Professor Junqiao Wu

Professor Sayeef Salahuddin

Fall 2019

Abstract

Synthesis of helical van der Waals crystals with tunable twist

by

Yin Liu

Doctor of Philosophy in

Engineering – Materials Science and Engineering

University of California, Berkeley

Professor Jie Yao, Chair

Helicity, a geometric property rendering an object nonsuperimposable on its own mirror image is ubiquitous in Nature. Inorganic crystals can grow into helical form, which is of great interest from the perspective of fundamental material science as well as application. Various inorganic crystals can be grown into helically twisted form on different scales ranging from nanoscale to mesoscale and to macroscale. The natural growth of twisted macroscopic quartz crystals in the bulk form has been documented and studied for centuries. On the nanoscale, quantum dots (QD), nanowires and carbon nanotube into helical structures. Those helical crystals have intriguing optoelectronics properties including rotatory optical activity and circular dichroisms in both absorption and photoluminescence as well as unique stereoselectivity in chemical reactions. These properties render inorganic crystals good potential of applications in polarization optics, chiroptical sensing, enantioselective catalyst and biomedical imaging. The material science responsible for forming these twisted inorganic crystals, nevertheless, remains largely mysterious and elusive.

In recent years, twisted van der Waals materials with rotational stacking of two-dimensional materials have attracted tremendous attention. The twist angle strongly affects the electronic states, excitons and phonons of the twisted structures through interlayer coupling, giving rise to exotic optical, electric, excitonic and spintronic behaviors. In twisted bilayer graphene, at certain twist angles, long-range periodicity associated with moiré patterns introduces flat electronic bands and highly localized electronic states, resulting in Mott insulating behavior and superconductivity. Theoretical studies suggest that these twist-induced phenomena are common to layered materials such as transition-metal dichalcogenides, black phosphorus and germanium monoselenide. In contrast to electronic band structure of the twisted bilayer graphene, unique features such as one-dimensional flat electronic band may emerge in those twisted 2D materials with different structures and symmetries.

The ability to manipulate the twisting topology of van der Waals structures offers a new degree of freedom through which to tailor their electrical and optical properties. Twisted van der Waals materials are usually created using mechanical exfoliation and a transfer-stacking method, but limitations exist to extend this method to a variety of two-dimensional materials. In contrast,

bottom-up growth methods could provide an alternative means to create twisted van der Waals structures. This dissertation explores the bottom-up synthesis of twisted van der Waals materials. We demonstrate that the Eshelby twist associated with a screw dislocation (a chiral topological defect), can drive the formation of twisted van der Waals materials.

The Eshelby twist is a continuous crystallographic twist generated by the torsional force of an axial screw dislocation in a one-dimensional structure. It has been shown to result in growth of helically twisted nanowires of various materials. This mechanism potentially provides a means to create twisted van der Waals (vdW) structures. Materials such as germanium sulfide (GeS) can grow into nanowires along the vdW stacking direction (the cross-plane direction), and introducing Eshelby twist into such nanowires naturally leads to twist between the successive layers.

We synthesized twisted GeS crystals at both nanoscale and mesocscale. In the synthesis method, GeS nanowires with axial screw dislocations are first grown along the stacking direction, yielding vdW nanowires with Eshelby twist. These wires possess continuous twists in which the total twist rates are defined by the radii of the nanowires, consistent with Eshelby's theory. Further radial growth of those twisted nanowires that are attached to the substrate leads to an increase in elastic energy, as the total twist rate is fixed by the substrate. The stored elastic energy can be reduced by accommodating the fixed twist rate in a series of discrete jumps in the twisting profile. This yields mesoscale twisting structures consisting of a helical assembly of nanoplates demarcated by atomically sharp interfaces with a range of twist angles.

The twisting profiles of the structures are tunable. We show that the twisting profile can be tailored by controlling the radial size of the structure. The twisting morphology gradually transitions from initial continuous twisting to intermediate twisting (consisting of both continuous twisting between the twist boundaries and discrete twisting at the boundaries) and eventually to discrete twisting with increasing radial size. This allows us to control the twisting profile and angles at twist interfaces by controlling the radial growth of the structure.

We also demonstrate that the twist rate and period can be tailored by tailoring the radii of the dislocated nanowires first grown in the VLS process. This is achieved by adding GeSe into the growth, which modulates the size of the droplets catalyzing the VLS process, therefore modulating the radii of the nanowires. The chemical modulation demonstrates good potential to tailor the twist rate and period of helical vdW crystals, enabling a new freedom to modulate optoelectronic properties and chiral light-matter interactions.

Last, we explored the anisotropic propagation of surface phonon polaritons in GeS, enabled by the strong in-plane anisotropy of the crystal structure. We demonstrate that GeS thin films at thickness of tens of nanometers support strongly anisotropic surface phonon polaritons in the far-infrared range. The dispersion relations of these phonon polaritons can be tuned by varying the thickness of the GeS film.

To my family

Table of Contents

Acknowledgements

First of all, I would like to show my sincere gratitude to my advisor, professor Jie Yao, who has inspired me to take chance to explore and learn a lot of new things in material science and photonics and guided me all the way toward graduation. I am in great debts to his patience, kindness and invaluable suggestions.

I must also thank many past and present colleagues in the Yao group. Special thanks to Sujung Kim, Zixuan Fang, Fuyi Yang and Michael Wang, who significantly contribute to the work presented in this dissertation. Among others, Shuren Lin, Shuai Lou, Kyle B Tom, Yang Deng, Zilun Gong, Rui Chen, Qingjun Wang and Jinhua Cao are great labmates who are very helpful in the course of my doctoral study.

Outside the lab, I have many fantastic collaborators. Characterization of the materials was largely performed in the National Center for Electron Microscopy and the Molecular Foundry at Lawrence Berkeley National Laboratory. I want to thank Dr. Emory Chan in the Molecular Foundry, who I have been working with for years. Emory is always friendly and extremely supportive of my research in the Foundry. Characterization using transmission electron microscopy was primarily performed in the National Center for Electron Microscopy. I must thank Professor Mary Scott, Ruopeng Zhang, Chengyu Song, Karen Bustillo and professor Andy Minor in the National Center for Electron Microscopy for their help with the electron microscopy. I want to thank Jie Wang, Jiangiuo Wen and Dafei Jin in the Argonne national lab, who also contributed to the TEM analysis. I am also deeply grateful to my theorist collaborators, Professor Daryl Chrzan and Haoye Sun for providing substantial insights into the growth mechanism of twisted germanium sulfide.

I would like to thank other members of my committee, professor Junqiao Wu and professor Sayeef Salahuddin for their help with my qualification exam and the preparation of the dissertation.

Last, to my family. I want to thank my parents and grandparents for their understanding and support. I must also thank my wife Ruijuan who has been with me for the last ten years. Her emotional support, encouragement and constant love are extremely important for me to survive my Ph.D.

List of Figures

Chapter 1 Introduction

1.1 Twisted van der Waals materials and twistronics

Tremendous research interest has recently been focused onto twisted two-dimensional (2D) materials since the interplay of the structural chirality with the spin and valley degrees of freedom of these materials enables a diversity of intriguing optical, electric, and magnetic properties.[1-8] To create these twisted structures, atomic layers of van der Waals (vdW) crystals are vertically stacked in a layer-by-layer configuration with controlled twist angle. The stacking can vary the lattice registry, significantly affecting the electron states and the conductivity through the interlayer coupling. This leads to widely tunable optoelectronic properties of those structures. For instance, twisted bilayer and multilayer graphene exhibit a large optical dichroism (a different absorption of left- and right-handed light), which can be tuned by controlling the rotation angle between the layers.[1]

More interestingly, the twist between the atomic layers creates rotational *Moiré* patterns with long-range periodicity, resulting in unconventional optical, electrical and magnetic properties. Flat electronic bands form in twist bilayer graphene at a series of twist angles, in which kinetic energies of electrons slowly vary with their momentum. In these flat bands, electrons become strongly correlated, giving rise to characteristics of Mott insulator and superconductivity.[4,5] In stark contrast, these insulating and superconducting states are absent in monolayer graphene. The twist angles at which the flat electronic bands are formed are referred to as 'Magic angles'. More recently, it has been discovered that the insulating states in magic-angle twisted bilayer graphene exhibit exotic ferromagnetism. [8]

Research on twisted bilayer graphene has led to the fast growing of the research field, so-called "twistronics", which is focused on how the twist angle affects optical and electrical properties of 2D materials.[9] Beyond bilayer graphene, "twistronics" study may be extended to other 2D materials. Theoretical studies suggest the twist-induced localization and the formation of flat bands are phenomena common to various 2D materials such as transition metal dichalcogenides (TMDC), black phosphorus and germanium selenide (GeSe). [10-12] Unique benefits can be derived from those twisted 2D materials, which have different structures and symmetries in contrast to graphene. Ab initio calculation has shown that flat bands appear at the edge of conduction band in twisted bilayer GeSe at small twist angles.[12] Close look on those "flat bands", however, reveals that the bands are entirely flat along one direction of the rectangle lattice and become dispersive (kinetic energies of electrons vary with their momentum) in the other lattice direction. Electronic states in these "flat band" have a distribution of charge density like one dimensional chains, resulting from anisotropic rectangular lattice of monolayer GeSe. This one-dimensional charge distribution is in stark contrast to the two-dimensional charge distribution in the twisted bilayer graphene. Twisted bilayer GeSe with such electronic states has been proposed as a novel one-dimensional system for studying strongly correlated physics that arises in one-dimensional systems.

1.2 Method to form twisted van der Waals materials

Fabrication of twisted vdW materials usually starts with mechanical exfoliation of 2D materials at monolayer or multilayer thickness from a bulk crystal. Those exfoliated materials are then transferred to stack in sequence with controlled twist angles. The transfer and stacking of individual 2D materials may be challenging. The twist interface should be clean and smooth; contaminants or bubbles at the interface can degrade the optoelectronics properties. More importantly, accurate rotational alignment of the constituent materials is required for accurately controlling the twist angles since electronic properties of the twisted materials are very sensitive to the twist angle.

Methods to fabricate twisted graphene have been developed for the studies of graphene twistronics, enabling exceptional capability to control the twist angle.[2,13-15] These methods utilize hexagonal boron-nitride (hBN) flakes to pick up and transfer the graphene flakes. Briefly, a hBN flake is exfoliated on a silicon oxide surface. A polydimethysiloxane (PDMS) block coated with polypropylene carbonate (PPC) is then used to pick up hBN from silicon oxide surface. This is enabled by the stronger adhesion force between the polymer and the hBN in comparison with the adhesion force between the hBN and the silicon oxide surface. The hBN transferred on the polymer block is then placed in contact with a part of a graphene flake. Since good adhesion exists between hBN and graphene, the part of the graphene flake in contact with hBN can be selectively detached from the original graphene flake. The detached graphene is rotated by a certain angle (twist angle) and placed in contact with the remnant part of the original graphene flake. The remnant graphene flake is picked up and stacked with the first graphene flake at the twist angle, forming a twisted bilayer graphene adhered with the hBN on the block polymer. The two pieces of graphene are obtained from the same flake such that they initially have same crystal orientation. The twist angle of the twisted bilayer graphene thus can be accurately controlled by the rotation angle. Last, the graphene/hBN stack is released from the polymer block and transferred onto another substrate for measurements. The polymer block can be heated up to temperatures above the glass-transition temperature of the polymers to drop down the graphene/hBN stack. Figure 1.1 schematically shows the “pick-up” and “ drop-down” procedure for the assembly of 2D heterostructures. This procedure can be repeated to fabricate multilayer twisted graphene/hBN stacks. A similar method has been used to fabricate twisted materials formed by TMDCs; Accurate control of twist angle in the twisted TMDC , nevertheless has not been achieved. [16]

The transfer-stacking approach has not yet been used to create twisted structures of a variety of 2D materials. Limitations may exist to apply the hBN mediated pick-up and transfer method to other 2D materials since the interaction between the hBN with other 2D materials may not be sufficiently strong for the transfer. In contrast, facile crystal growth methods could provide an alternative means to create twisted vdW structures. Previous study has reported the synthesis of twisted bilayer molybdenum disulfide at a range of twist angles using chemical vapor deposition (CVD). In this dissertation, we explore the possibility to use bottom-up method to synthesize twisted vdW material with novel twisting morphologies.

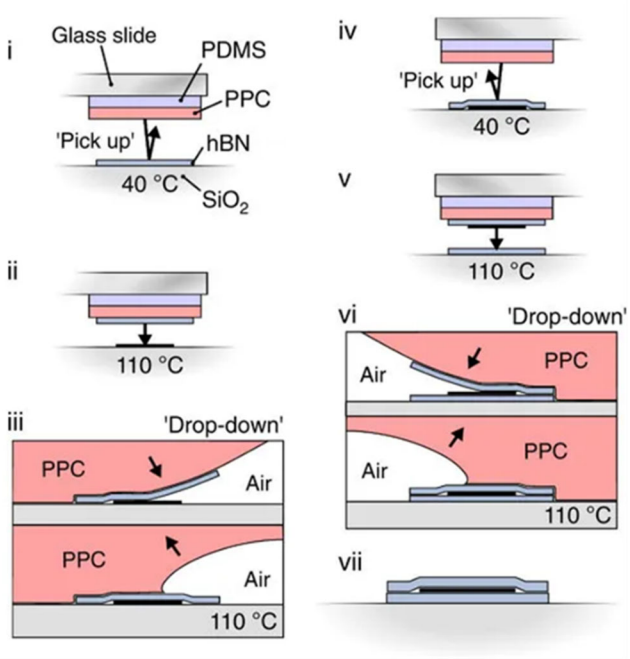

Figure 1.1 Schematic showing the process for assembly of 2D heterostructures by pick-up and drop-down. PPC coated PDMS block mounted on glass slides are used to pick up and release 2D materials. Figure adapted from[14].

1.3 Growth of twisted crystals

Various inorganic crystals can be grown into twisted form on different scales ranging from nanoscale to mesoscale and to macroscale.[17] For instance, the natural growth of twisted macroscopic quartz crystals, also known as "gwindel" quartz has been documented and studied for centuries.[18] On the nanoscale, quantum dots (QD), nanowires and carbon nanotube can be grown from gaseous and solution phases into helical structures. [19]

Different mechanisms have been identified for the growth of twisted materials. Quantum dots including CdSe, CdS and ZnS QDs have been synthesized into chiral forms with the presence of stereospecific chiral molecules such as penicillamine.[19] The chirality of QDs is determined by the chirality of the capping molecules/ligands. Those chiral QDs exhibit circular dichroism (CD), showing different absorption of left-hand and right-hand circular polarized light. [19]

Nanowires can also grow into chiral forms via the mechanism of Eshelby twist.[20-23] In 1960s, J. D. Eshelby predicted that an axial screw dislocation at the center of a thin whisker can result in a twist in the whisker.[24,25] As a result, the elastic energy associated with the screw dislocation is reduced. In Eshelby's theory, the twist rate $\alpha = \kappa \frac{b}{A}$ where b is the Burgers vector of the screw dislocation, κ is the geometrical prefactor that depends on the shape of the cross section and A is cross sectional area of the whisker. The twist (so-called Eshelby twist) has been identified as an intriguing mechanism for the growth of helical nanowires. Screw dislocations can be present in the middle of nanowires, resulting in nanowires with crystallographic twist. The screw dislocation intersects a crystal facet, giving rise a monolayer spiral step-edge centered on the dislocation. The step-edge persists while the nanowire is growing; attaching constituent atoms

of the nanowire to the step-edge retain the spiral shape of the edge. The screw dislocation provides a spiral growth front driving the one-dimensional growth of nanowire. The dislocation mediated growth is considered in the Burton-Cabrera-Frank theory, which has been shown as important mechanism for crystal growth under the condition where the thermodynamic driving force for the growth is low or moderate. [26] The screw dislocation and its resultant Eshelby twist in the nanowires have led to the growth of twisted nanowires of various material including lead sulfide (PbS), lead selenide (PbSe), zinc oxide (ZnO), cadmium selenide (CdSe), cuprous oxide (CuO), indium phosphide (InP) and copper.[20-23,27,28] For instance, "pine tree" like nanowires of PbS and PbSe with helical branches have been synthesized through the dislocation driven growth. (Figure 1.2) [20,22] In these helical "pine tree" structures, fast growth of trunk nanowire is driven by a screw dislocation whereas slow growth of branch nanowire is driven by the vapor-liquid-solid (VLS) process. The helical rotation of the branches is the consequence of the Eshelby twist.

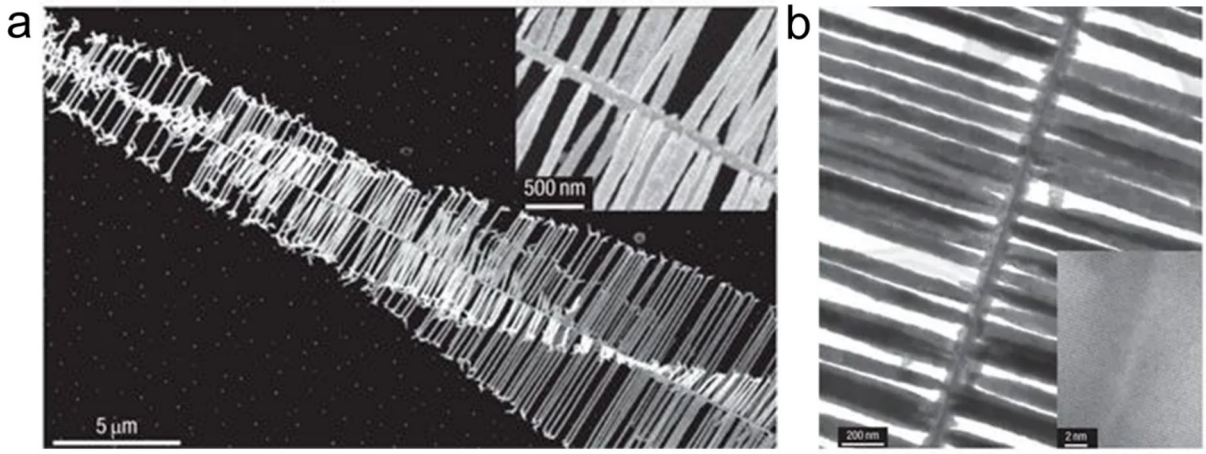

Figure 1.2 (a) Scanning electron microscopic (SEM) image of "pine-tree" like PbSe nanowires. Inset:high-resolution SEM. (b) transmission electron microscopic image (TEM) of a single chiral branched NW with screw dislocation line (black) in the center. Inset: High resolution TEM image of the dislocation. Images adapted from[22].

This inspiring mechanism of Eshelby twist potentially provide a unique means to create twisted vdW structures. Materials such as germanium sulfide (GeS), indium selenide(In_2Se_3), and bismuth selenide(Bi_2Se_3) can grow into nanowires with the growth direction to be the vdW stacking direction (the cross-plane direction).[29-31] Introducing Eshelby twist into such nanowires naturally leads to twist between the successive layers. Even though screw dislocations in layered vdW materials are well known, the Eshelby twist has not been considered in those materials since screw dislocation in those materials have relatively large lateral size (larger than a few micrometers) resulting in negligible Eshelby twist. This dissertation utilizes the mechanism of Eshelby twist to grow twisted vdW materials.

1.4 Layered germanium monosulfide (GeS)

This dissertation explores the growth of the twisted GeS via the mechanism of Eshelby twist. GeS is layered IV-VI monochalcogenide semiconductor with an indirect band gap of ~ 1.6 eV. Other widely studied compounds in this material family are tin selenide(SnSe), tin sulfide (SnS) and germanium selenide(GeSe), which are isostructural with GeS. Bulk GeS has an orthorhombic crystal structure in the space group of Pcmn (with a=4.29Å b=3.64Å and c=10.42Å) which is formed by covalent bonding within atomic layers and vdW bonding between the layers. Each layer has a corrugated layered structure with strong in-plane anisotropy between the zigzag and armchair directions, which is analogous to the structure of black phosphorus. Figure 1.3 shows the crystal structure of GeS. The anisotropic crystal structure of GeS leads to strong anisotropy in the optoelectronic properties including polarization-dependent optical absorption/photoluminescence and anisotropic photoconductivity, which is attractive for application in photodetectors and optical computing. [32-35] Like in most 2D materials, the optoelectronic properties of GeS is dependent on its thickness. In the monolayer limit, exotic multiferroic behavior with coupled ferroelectricity and ferroelasticity is predicted to exist in GeS at temperatures above room temperature, providing good potential to be used for 2D non-volatile memories.[36]

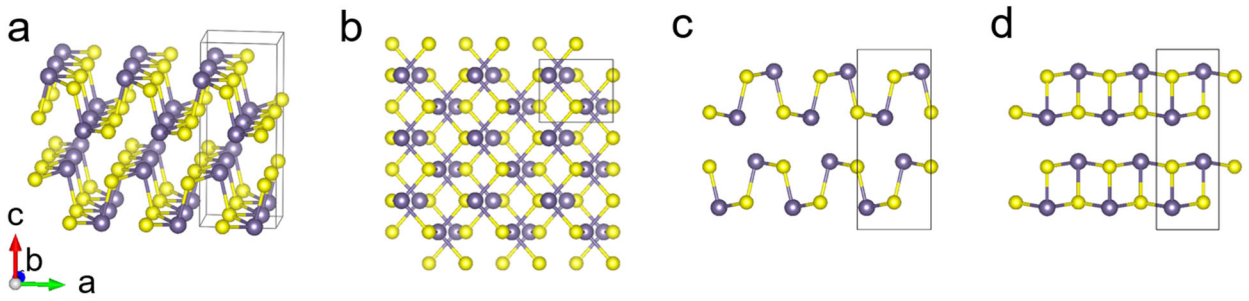

Figure 1.3 (a) Perspective view of the crystal structure of the IV-VI compounds. Purple: Ge atoms. Yellow: S atoms.The unit cell is shown with a framed box. Crystal structure viewed along c direction (b), b direction (c) and a direction (d), respectively.

1.5 Synthesis of GeS nanowires

The most widely used method to synthesize nanowires is vapor-liquid-solid (VLS) method, which has been used to synthesize nanowires of various materials. In typical VLS growth, a low-melting-point liquid alloy droplet is first formed as catalyst. Gaseous precursor species incorporate through the surface of the droplet, supersaturating the droplet. This results in the growth at the droplet-nanowire interface. The droplet acts as a channel for the one dimensional growth of the nanowire. The size of the droplet defines the radius of the nanowire.

GeS nanowires have been grown using the gold catalyzed VLS process.[29,37] Despite the different growth parameters used in those previous studies, most majority of the GeS nanowires have growth direction to be the vdW stacking direction. Such growth behavior of GeS nanowires suggests that incorporating screw dislocation into those GeS nanowires may result in a twist between the interlayers via the Eshelby twist, resulting in the growth of GeS crystals with

intriguing twisting morphology. The incorporation of the screw dislocation may be achieved by judiciously using proper growth conditions. We note that in addition to GeS, other layer materials such as indium selenide(In_2Se_3) and bismuth selenide (Bi_2Se_3) have been reported to grow into nanowires with the growth direction to be the vdW stacking direction (cross-plane), akin to the GeS nanowires.[30,31] In those previous studies, such nanowires growing along vdW stacking direction, however, either accounted for a small fraction of the synthesized wires or could be synthesized with better yield within a narrow range of growth parameters. The growth directions of nanowire are synergistically influenced by a combination of factors such as temperature, diameter, surface energies of crystal facets and interface energies between the material and catalyst. In contrast to the growth of GeS nanowire, significant effort may be required to tailor and optimize the growth direction to be along the cross-plane direction for the those materials. This dissertation, therefore, selects GeS as the material to demonstrate the dislocation-driven twist growth of vdW crystals.

1.6 Organization of the dissertation

The remainder of the dissertation is organized as follows:

In chapter 2, we demonstrate that the Eshelby twist, which is associated with a screw dislocation can drive the formation of twisted GeS structures on scales ranging from the nanoscale to the mesoscale. In the synthesis, axial screw dislocations are introduced into nanowires growing along the stacking direction, yielding van der Waals nanostructures with continuous twisting. The total twist rates of the nanowires are defined by their radii, consistent with Eshelby's theory. Further radial growth of those twisted nanowires yields mesoscale twisting structures consisting of a helical assembly of nanoplates demarcated by atomically sharp interfaces with a range of twist angles. We further show that the twisting topology can be tailored by controlling the radial size of the structure.

In chapter 3, we demonstrate that the twist rate and twisting periods of the twisted crystals can be tailored by tailoring the diameters of the nanowires that are first grown by the VLS process. In doing so, we added germanium selenide (GeSe) into the precursor to grow the twisted nanowires, which chemically modulates the size of the catalyst droplets, therefore tuning the radii of the nanowires. Increased concentration of GeSe in the precursor leads to twisted nanowires with increasing diameters. This decreased the twist rate and increased the period of the twisted crystals. Increasing the Se concentration from x=0 to x=0.11 in the $GeS_{1-x}Se_x$ precursor decreases the twist rate from 0.59 rad/μm to 0.22 rad/μm, corresponding to an increase in the twist period from 8 μm to 15 μm. In addition to tuning the twist rate, adding GeSe provide a route to compositional engineering of the twisted vdW crystals for tunable optoelectronic properties.

In chapter 4, we propose that orthorhombic layered GeS supports the propagation of the strongly anisotropic surface phonon polaritons (SPhPs). SPhPs are electromagnetic modes result from the coupling of the ionic polarization in the material with external electromagnetic field. Chapter 4 first introduces the concept of surface phonon polaritons with emphasis on the recent studies on the phonon polaritons in van der Waals materials. Using semi-analytical analysis and full wave simulation, we demonstrate GeS films support strongly anisotropic phonon polaritons in the terahertz (THz) range. Moreover, our simulations show that these SPhPs are strongly dependent on the film thickness. As the thickness of the film decreases, dispersion of the SPhPs markedly changes and the supported SPhPs become more confined and intense.

Chapter 2 Twisted van der Waals crystals of GeS

2.1 Synthesis of the twisted GeS

Twisted GeS structures were synthesized on silicon substrates by using a chemical vapor transport method with gold as a catalyst. The synthesis was performed using a horizontal tube furnace with a diameter of 1 inch. The temperature profile of the furnace was measured with a thermocouple. Figure 2.1 shows a schematic diagram of the furnace and the temperature profiles of the furnace for different heating temperatures at the source site. The substrates used for the synthesis were Si(100) substrates with natural oxidization and thermally oxidized Si(100) substrates with 300 nm silicon oxide. Gold catalyst, 3 nm thick, was deposited on those substrates and was patterned to form microbars in a width of tens of micrometers that are spaced by a few hundred micrometers, using photolithography and electron-beam evaporation deposition. Before the synthesis, the furnace was pumped down to a base pressure of 5 mTorr and flushed with argon gas blended with 4% hydrogen several times. In the synthesis, GeS powder (Sigma-Aldrich) was placed at the centre of the tube and heated to evaporate at a fixed pressure flowing with Ar/4% H_2 carrier gas. The substrates were placed 10–12 cm downstream from the GeS source. Typical growth conditions utilize pressures of 1–2 Torr, flow rates of 20–50 standard cubic centimeters per minute (sccm), source temperatures of 400–450 °C, deposition temperatures of 350–400 °C and a growth time of 20 min.

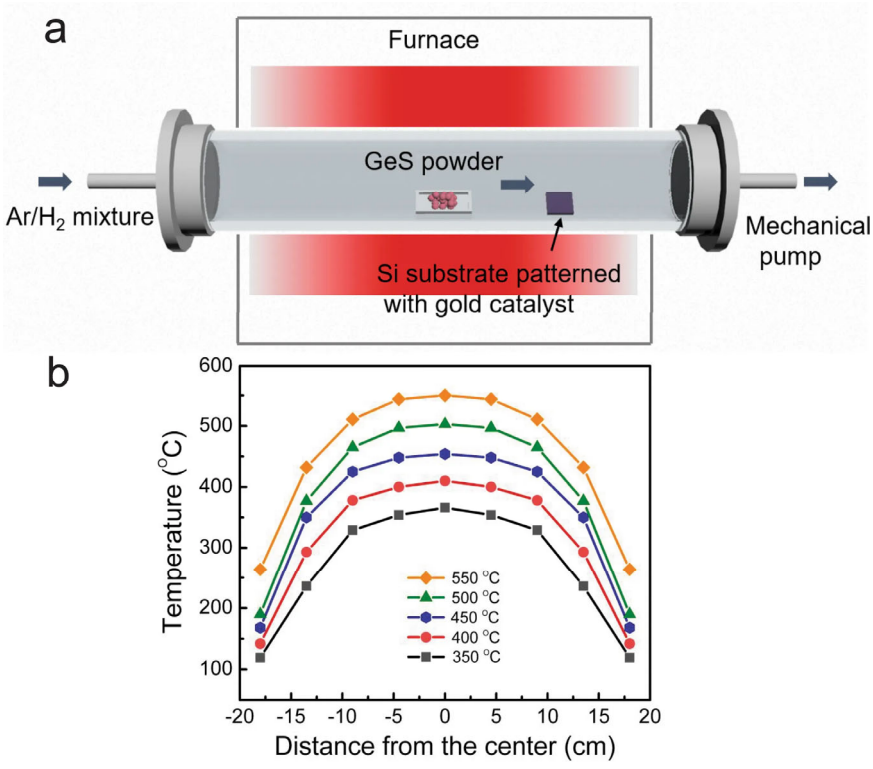

Figure 2.1 (a) Schematic diagram of the furnace used for the synthesis of the twisted GeS crystals. (b) Temperature profiles of the furnace for heating temperatures of 350 °C, 400 °C, 450 °C, 500 °C and 550 °C at the source site.

2.2 Twisting morphology of the GeS crystals

A representative scanning electron microscopy (SEM) images of a mesoscale crystal is presented in figure 2.2a,b, showing a well-defined helicoidal morphology. The synthesized crystals have varying twist periods ranging from 2 μm to 20 μm, with total lengths up to hundreds of micrometers, and radial sizes ranging from several hundred nanometers to more than 10 μm. These mesoscale crystals have a three-dimensional architecture consisting of periodically rotating nanoplates with a thickness of several hundred nanometers, as is revealed by cross-sectional transmission electron microscopy (TEM) (Figure 2.2c) and cross-sectional SEM images acquired through consecutive focused ion beam (FIB) milling along the twist axis of the structure (Figure. 2.2d). Statistical analysis suggests approximately equal numbers of left-handed and right-handed crystals (Figure 2.3).

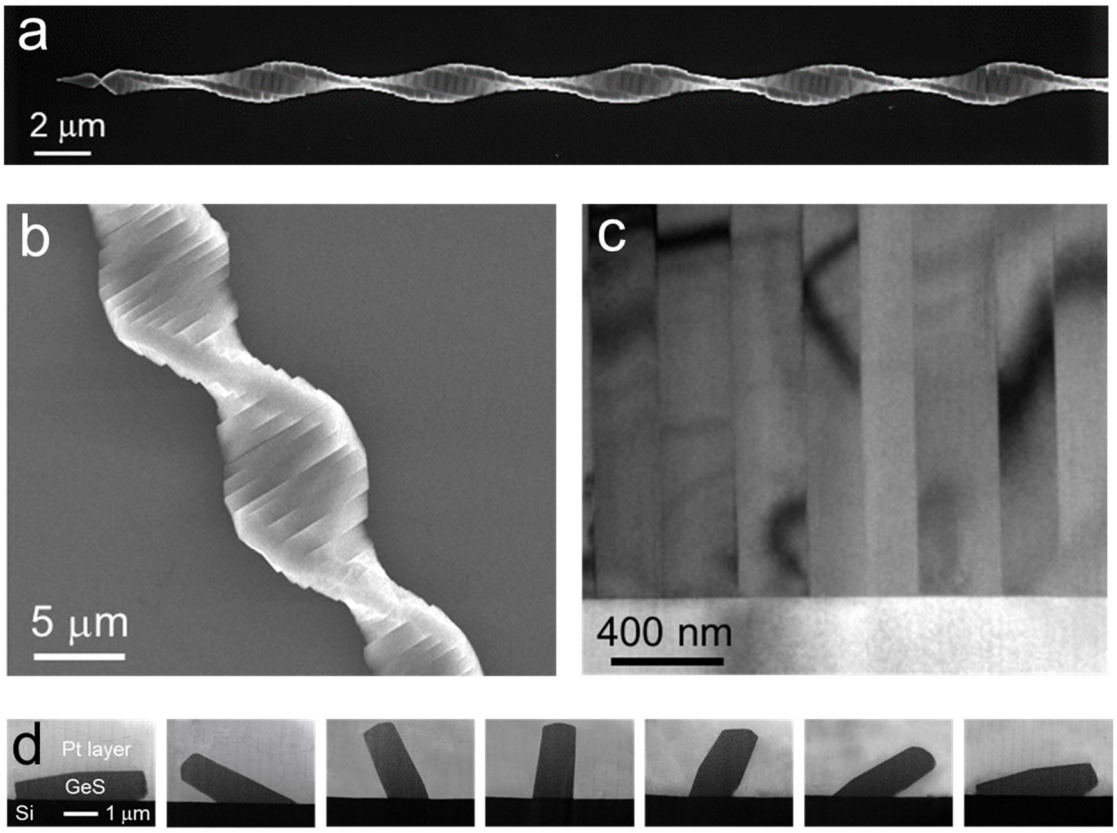

Figure 2.2 (a) and (b) SEM images showing the twisting morphology of a mesoscale GeS crystal. (c) Cross-sectional TEM image of a twisted crystal. The surface normal of the cross-section is perpendicular to the twist axis. (d) A series of SEM images showing the evolution of radial cross-sections within one period of a twisted structure.

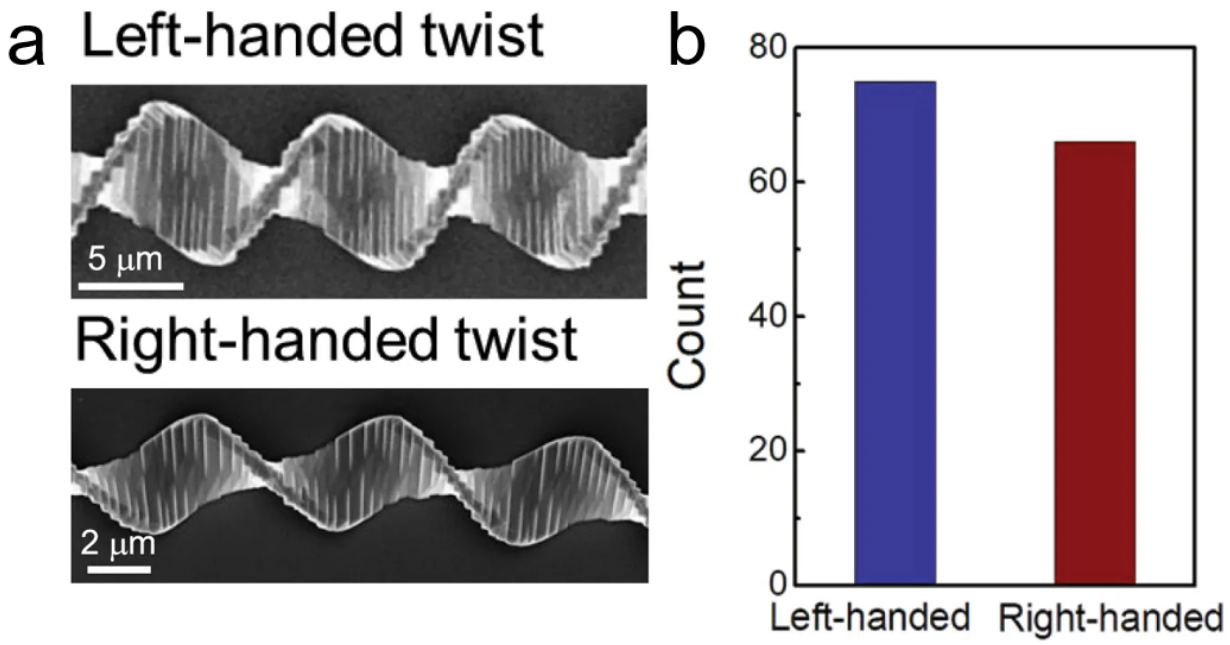

Figure 2.3 (a) Representative SEM micrographs showing mesoscale twisted structures with opposite helicity. (b) Histogram showing that the population of left-handed structures is approximately equal to the population of right-handed structures. The measured ratio of left-handedness to right-handedness is 74:67.

2.3 Compositional and structural analysis

Quantitative chemical analysis using energy dispersive spectroscopy (EDS) of the structure indicates a 1:1 atomic ratio of Ge:S. (Figure 2.4) The crystallinity and orientation of the twisted structures were examined by scanning Laue X-ray microdiffraction (μSXRD) with submicrometer spatial resolution on beamline 12.3.2 of the Advanced Light Source synchrotron at the Lawrence Berkeley National Laboratory [38]. The sample was raster scanned with a 0.5 μm step size and a Laue pattern collected at each step. The Laue patterns were then indexed using the XMAS software, providing orientation map of the sample. Crystal structure of GeS is shown in figure 2.5. The structure is in the space group of Pcmn with a axis to be the armchair direction and b axis to be the zigzag direction. X-ray crystal orientation maps of the structure (Figure 2.6 a,b) show that the twist axis of the crystal is along the c axis (the cross-plane direction), and the vdW planes, defined by the a and b axes in Fig. 1c, periodically rotate about the c axis with a period of ~ 4 μm such that there is a total twist of 180° in a single period (that is, between two adjacent minimum widths as seen in Figure 2.2a). In addition, we performed Laue X-ray diffraction on a twisted GeS with larger period (~15 μm), which further confirms the periodic twisting structure. X-ray microdiffraction analysis on the structure with large period/ a small crystallographic twist reveals more details on the crystallography of the twist. The analysis suggests that the widest portion in a period has its b axis aligned with the substrate normal while the narrowest portion in the period has its a axis aligned with the substrate normal. This growth phenomenon may result from the structural anisotropy of GeS.

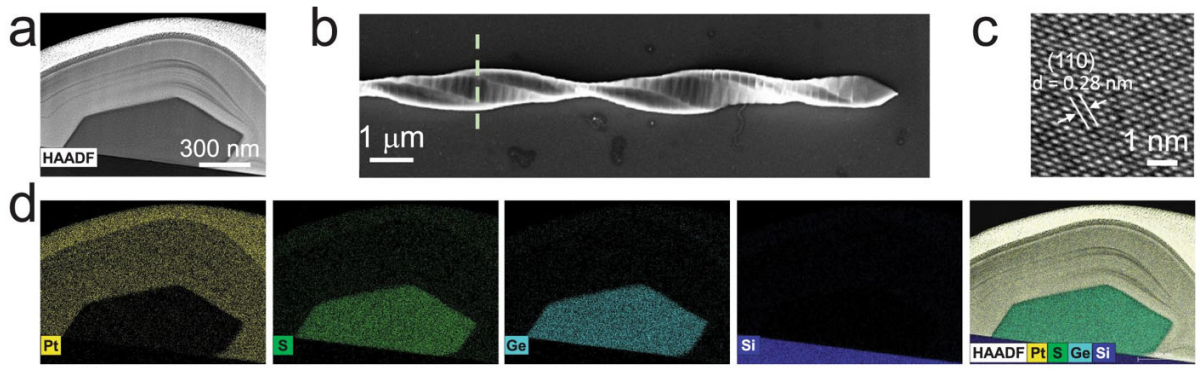

Figure 2.4 Chemical analysis of mesoscale twisted GeS using energy-dispersive X-ray spectroscopy (EDS). (a) HAADF-STEM image of a cross-sectional lamellar sample with its normal perpendicular to the twist axis prepared by FIB milling. (b) SEM image showing the crystal used to prepare the TEM sample. The dashed line represents the location of the cross-section. (c) High-resolution TEM (HRTEM) image of the cross-section confirming that the twist axis is aligned with the [001] direction. (d) STEM-EDS elemental map of the cross-section verifying that the structure is a compound consisting of Ge and S in an atomic ratio of 1:1.

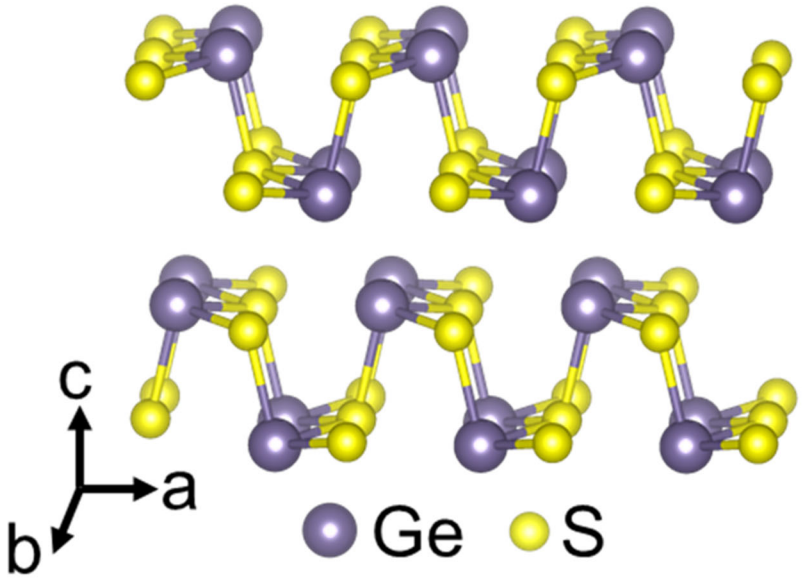

Figure 2.5 Layered crystal structure of GeS

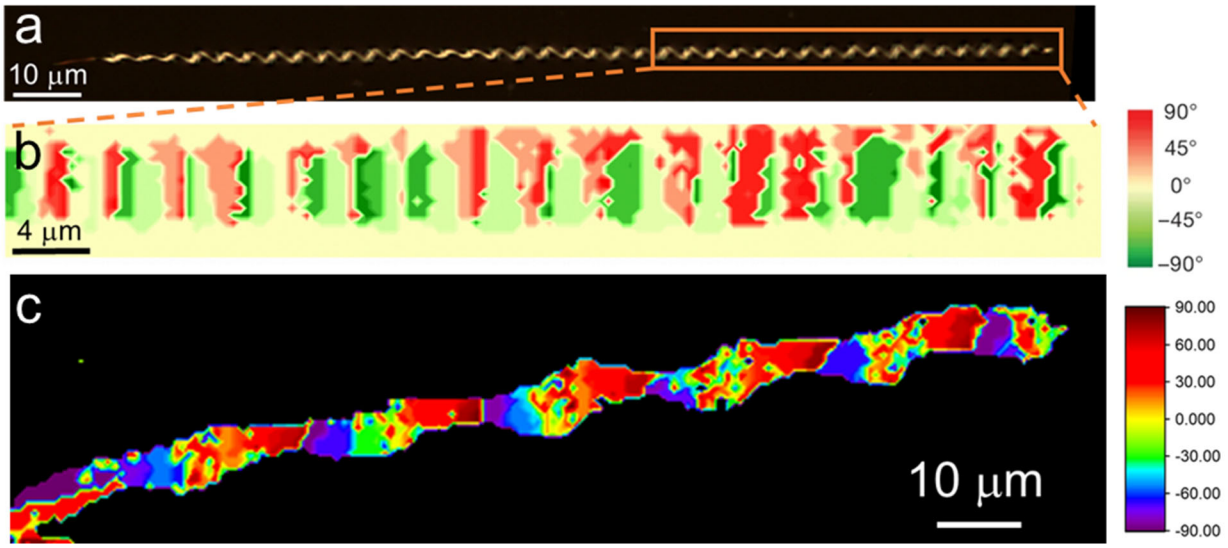

Figure 2.6 Optical micrograph (a) and crystal orientation map (b) of a twisted structure generated by X-ray Laue microdiffraction analysis. The orientation angle is defined by the angle between the b axis and the norm of the substrate. The region of the X-ray analysis is highlighted by the orange box in (a). (c) Additional X-ray microdiffraction analysis on a twisted GeS crystal with a period of about 15 µm. The orientation angle in the X-ray orientation map is also defined by the angle between the b axis and the normal to the substrate.

2.4 Twist interfaces and twist angles

Atomic-resolution scanning transmission electron microscopy (STEM) confirms that the nanoplates are single crystals in the space group Pcmn and that the twist interface between the nanoplates is atomically sharp (Figure 2.7). The twist angle at this interface is 10.27° (as determined from the change of tilt angle needed to tilt each of the two crystals to the [010] zone axis; Figure. 2.7 a, b). The twist interface was also characterized by plan-view TEM of the stacking nanoplates with the incident electron beam along the twist axis (Fig. 2.8 a–f). The lamellae sample containing two adjacent stacking nanoplates was prepared with the surface normal along the twist axis using FIB milling. Electron diffraction patterns indicate a misorientation angle of 7.5° between the two nanoplates (Figure. 2.8b, c), and double diffraction patterns were clearly observed from the twist boundary (Figure 2.8d). The double diffraction in reciprocal space reflects long-range ordering with a period of 2.26 nm in real space, which agrees well with the simulated rotational moiré pattern (Figure 2.8e, f). In addition to TEM, we used electron backscattering diffraction (EBSD) to measure twist angles (Figure 2.9). In total, 15 twist angles were measured on six twist structures. The values of the measured twist angles are 10.6°, 16°, 6.8°, 10.3°, 13.9°, 7.1°, 8.3°, 14°, 9.6°, 10.2°, 14°, 6.7°, 8.7°, 10.27° and 7.5°. This is a range from 6.8° to 16° with an average of 10.3° and standard deviation of 3°. Further estimates of the twist angles were based on the number of nanoplates or interfaces per period, obtained from SEM imaging, given the fact that each period has a total twist of 180 degree. The distribution of twist angles obtained this way

follows a Gaussian profile ranging from 5 degree to 18 degree with a most probable value of around 10 degree (Figure 2.10) which is in good agreement with the direct measurements.

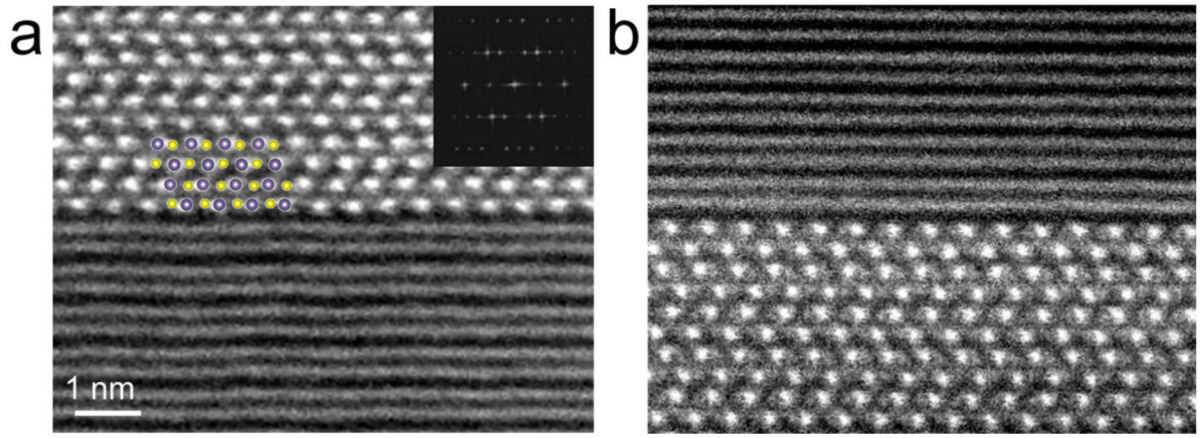

Figure 2.7 Optical micrograph (a) and crystal orientation. High-angle annular dark-field scanning transmission electron microscopy (HAADF-STEM) image showing the atomically sharp interface between two nanoplates in a twisted structure with the upper crystal on the [010] zone axis. A structural model of GeS with labelled Ge atoms (blue) and S atoms (yellow) is superimposed on the STEM image. The inset shows the fast Fourier transform (FFT) pattern of the upper crystal.

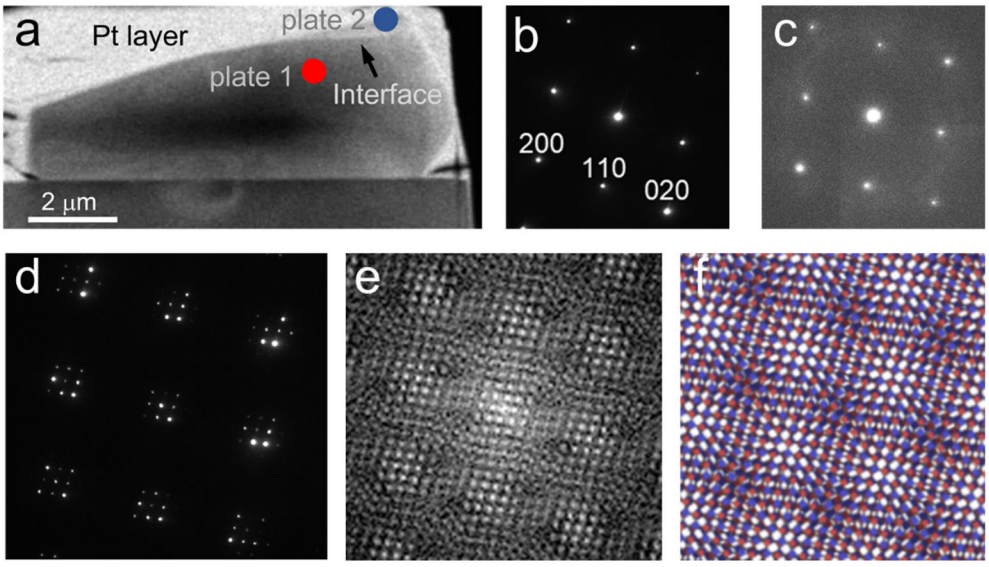

Figure 2.8 (a) Using FIB, a lamellae sample containing two adjacent stacking nanoplates was prepared with the surface normal along the twist axis. After the thinning of the sample, the largest fraction of the sample consists of a single nanoplate (either the top or the bottom one), while a smaller fraction preserves the twist interface between the two nanoplates. The arrow shows the location of the twist interface. The red and blue dots show the locations that respectively contain the single upper plate and the single lower plate. (b) and (c) Selected area electron diffraction (SAED) patterns for the [001] zone axis acquired from a plan-view TEM sample containing two stacking nanoplates. SAED patterns were acquired on the top crystal (b) and bottom crystal (c), suggesting a misorientation angle of 7.5° between those two crystals. (d) Double diffraction pattern acquired from the twist interface of the two nanoplates. (e) Inverse FFT images of the double diffraction pattern and the simulated rotational moiré pattern (f), illustrating the long-range periodicity in real space.

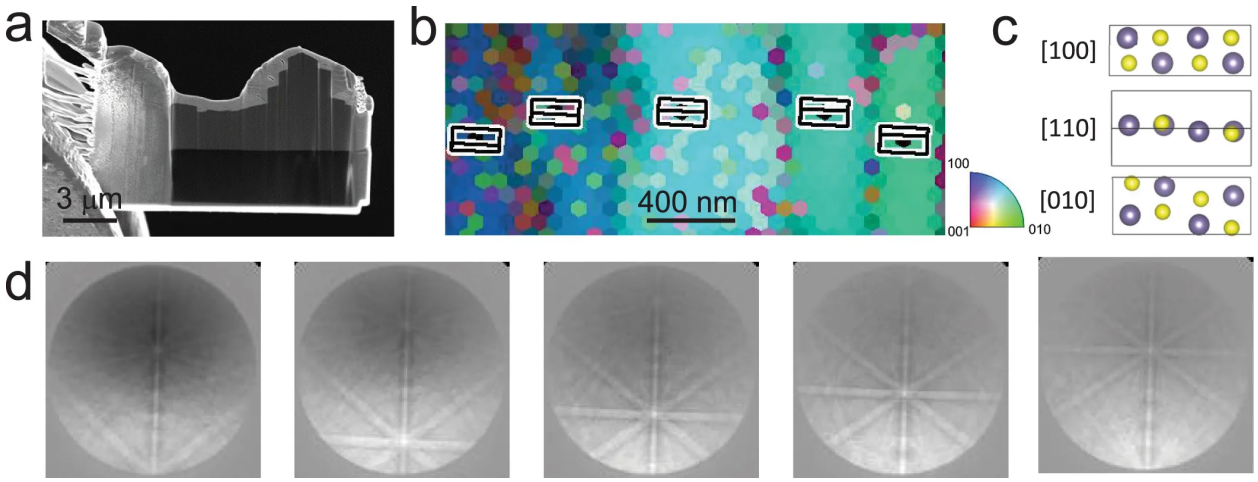

Figure 2.9 (a) SEM image of a specimen used for EBSD. The lamellar sample is prepared by FIB milling with surface normal perpendicular to the twist axis of the structure. b, Representative EBSD orientation map of the nanoplates with the 2D projection of the unit cell superimposed. The unit cell projection shows the crystal orientation of the nanoplates at that point. The misorientations of the plates (that is, the differences between the crystal orientations of adjacent nanoplates) are quantified to be 10.2°, 14°, 6.7° and 8.7°. c, Unit cell of GeS viewed along the [100], [110] and [010] directions. d, Corresponding EBSD patterns acquired from five adjacent nanoplates. Note that 13 twist angles were measured on four mesoscale twisted structures using EBSD, and a representative measurement is shown in this figure. In addition, two twist angles were measured using the TEM (shown in Fig. 2).

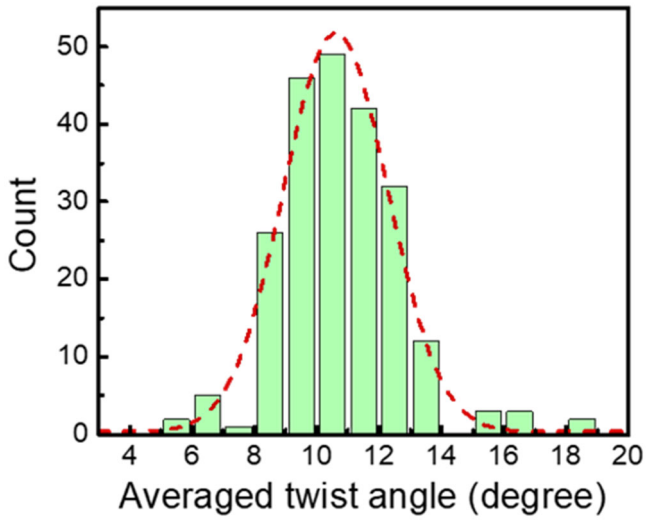

Figure 2.10 Distribution of twist angle estimated by counting the number of interfaces per period using SEM imaging.

2.5 GeS nanowires with the Eshelby twist

This mesoscopic twist originates from Eshelby twist in the dislocated nanowires that were first grown via the gold-catalyzed vapour–liquid–solid (VLS) method. The VLS growth of the GeS nanowires have been previously reported, showing the growth direction is along the c-axis. [29,37] In contrast to prior work, the VLS grown nanowires grown on substrate in our studies clearly shows a morphological twist (Figure 2.11a) ,which is reminiscent of the Elsheby twist in one-dimensional materials. Eshelby predicted that an axial screw dislocation at the center of a thin whisker will result in a twist that relieves the elastic energy associated with the screw dislocation.[24,25] The twist rate is $\alpha=\kappa b/A$ where b is the magnitude of the Burgers vector b of the screw dislocation, κ is a prefactor related to the geometry of the whisker, and A is the cross-sectional area of the whisker.

We confirmed the existence of the Eshelby twist through TEM studies. In TEM (Figure 2.11b) and high-resolution TEM images (Figure 2.11c), a line defect is evident at the center of the nanowire. Convergent beam electron diffraction (CBED) shows that the nanowire has a crystallographic twist (Figure 2.11 b). The CEBD analysis utilizes a sub-nanometer electron probe, enabling determining the crystal orientation of a local segment of the nanowire. The result shows that the orientation of the nanowire changes from [110] direction to [210] direction and to [310] direction over an approximate distance of 1.4 micrometer. This corresponds to a 24 degree of rotation about the c-axis, amounting to a twist rate of 0.3 rad/μm which is comparable to the twist rate of mesoscopic crystals. The twist rate is comparable to the twist rates reported in nanowires of covalent semiconductors.[20,22]

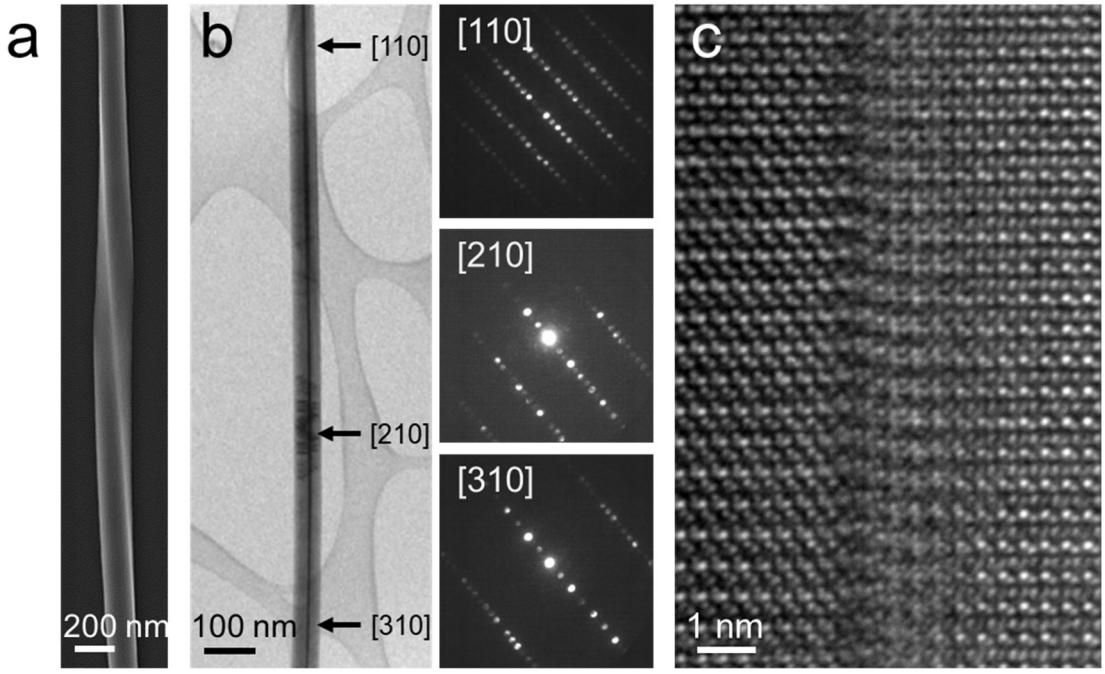

Figure 2.11 (a) SEM image of a twisted nanowire adhering to a substrate. (b)TEM image of a nanowire with Eshelby twist (left) and corresponding CBED patterns (right) taken from different locations on the nanowires, suggesting that the crystal orientation changes from direction [110] to [210] and then to [310] with respect to the incident electron beam. The locations are marked with black arrows. Note the CBED patterns are rotated 38° anticlockwise with respect to the image of the nanowire. (c) High-resolution TEM image of the dislocation.

Burgers vector analysis was performed on the basis of g · b contrast in TEM images (Figure 2.12). In this analysis, the dislocation is imaged with different g reflections in the reciprocal space and the Burgers vector can be determined based on the invisibility criterion that dislocation becomes invisible or weakly contrast when g.b =0. To perform the analysis, the nanowire is first tilted on [210] zone axis. Next, the sample is further tilted to create strong two beam condition for different diffraction spots in the diffraction pattern. Dark-field (DF) images of the dislocation are respectively taken for g= (002) and g =($2\bar{1}0$). For g = (002), high contrast of the dislocation is observed while for g= ($2\bar{1}0$), the dislocation become invisible . As such, the direction of Burgers vector is determined to be along the [001] growth direction (c axis), confirming the screw character of the dislocation.

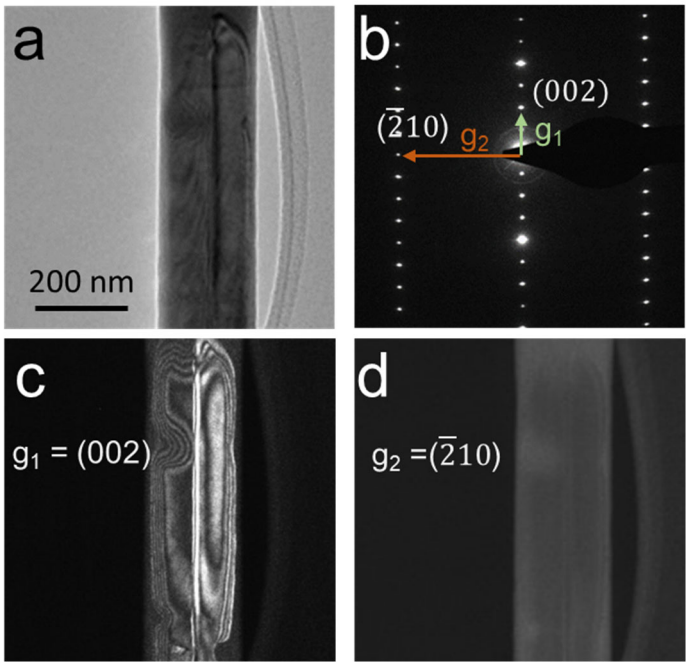

Figure 2.12 (a) TEM image of another nanowire with axial dislocation tilted on the [120] zone axis. (b) Corresponding SAED pattern for the nanowire in (a) . The arrows in the SAED pattern highlight the reflections used for g · b analysis. (c) and (d), Dark-field TEM images under the two-beam condition showing high (c) and low (d) contrast of the dislocation when g_1 = (002) and g_2 = $(\bar{2}10)$ are excited, respectively.

To grow nanowires with the Eshelby twist, we had to optimize growth parameters including pressures and carrier gas flow rates. For non-optimal growth conditions, almost all of the synthesized nanowires are synthesized with no twist (Figure 2.13).

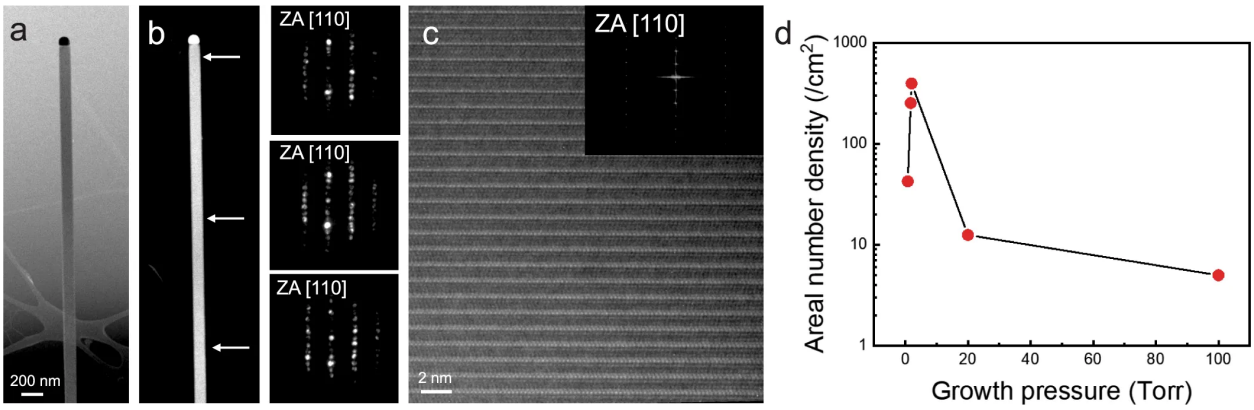

Figure 2.13 (a) TEM image of a normal nanowire without a dislocation produced at a growth pressure of 5 Torr. (b) Corresponding STEM image of the nanowire (left) and CBED patterns acquired from three different locations on the nanowire (right)), showing the absence of the Eshelby twist. The white arrows in the STEM images show the locations where the CBED patterns are collected. (c) HRTEM image of the normal nanowire showing that the growth direction of the nanowire is along the c axis. The inset is the FFT pattern of the HRTEM image suggesting the image is taken on the [110] zone axis (ZA). (d) Areal number density (the number of twisted structures per unit area of the substrate) of twisted GeS structures as a function of the growth pressure. In this experiment, the flow rate of Ar/H_2 carrier gas

and the source temperature were fixed at 50 sccm and 450 °C, respectively. The growth of dislocated nanowires is achieved with typical growth pressures in the range 1–2 Torr and a flow rate of 20–50 sccm, whereas the yield of nanoscale and mesoscale twisted GeS drops when the growth pressure deviates from optimum.

2.6 Origin of the twist in the GeS crystals

Further radial growth on those nanowires with the Eshelby twist results in mesoscale twisted GeS. This is illustrated by the twisted GeS structure consisting of both twisted nanowires and twisted mesoscale structures, as is shown in Figure 2.14a. Since the axial growth is driven by VLS process in the presence of a dislocation, the axial growth has more rapid kinetics than the radial growth which is in agreement with Burton-Cabrera-Franck's theory of crystal growth. [26] Thus the axial growth to form the nanowires and the radial growth are largely decoupled and occur in sequence. We found that the gold nanoparticle that catalyzes the VLS growth of the nanowire was present at the tip of the mesoscale structure (Figure 2.14b), with a size proportional to the period of the structure; here, a large catalyst particle corresponds to a large period. The twist rates of the mesoscale structures are 0.2–1.1 rad μm^{-1}, comparable to the measured twist rate of the GeS nanowire. Further analysis established a good linear relationship between the overall twist rate of the mesoscale structure and the inverse of the cross-sectional area of the catalyst particle at its contact with GeS. The size of the catalyst particle at the tip of mesoscale structures approximately represents the radial size of the nanowires first axially grown by the VLS process (Figure 2.14c). The relationship between the twist rate and catalyst size effectively reflects the relationship between the twist rate and cross-sectional area of the VLS-grown nanowires (Figure 2.14d), revealing the Eshelby twist mechanism underpinning the formation of the discretely twisting structure. Fitting of the results using the Eshelby model gives a reasonable magnitude of 1.75 nm for κb, which is between one and two lattice constants along the c axis (c = 1.04 nm). This magnitude agrees with the fact that the Burgers vector tends to be the shortest lattice vector (c) to reduce the elastic energy. For a more accurate evaluation of the Burgers vector from the Eshelby model, the anisotropic crystal structure and the complex cross-section of the nanowire should be considered, to correct the overestimation of area arising from our assumption of a circular cross-section and to determine the prefactor κ.[25]

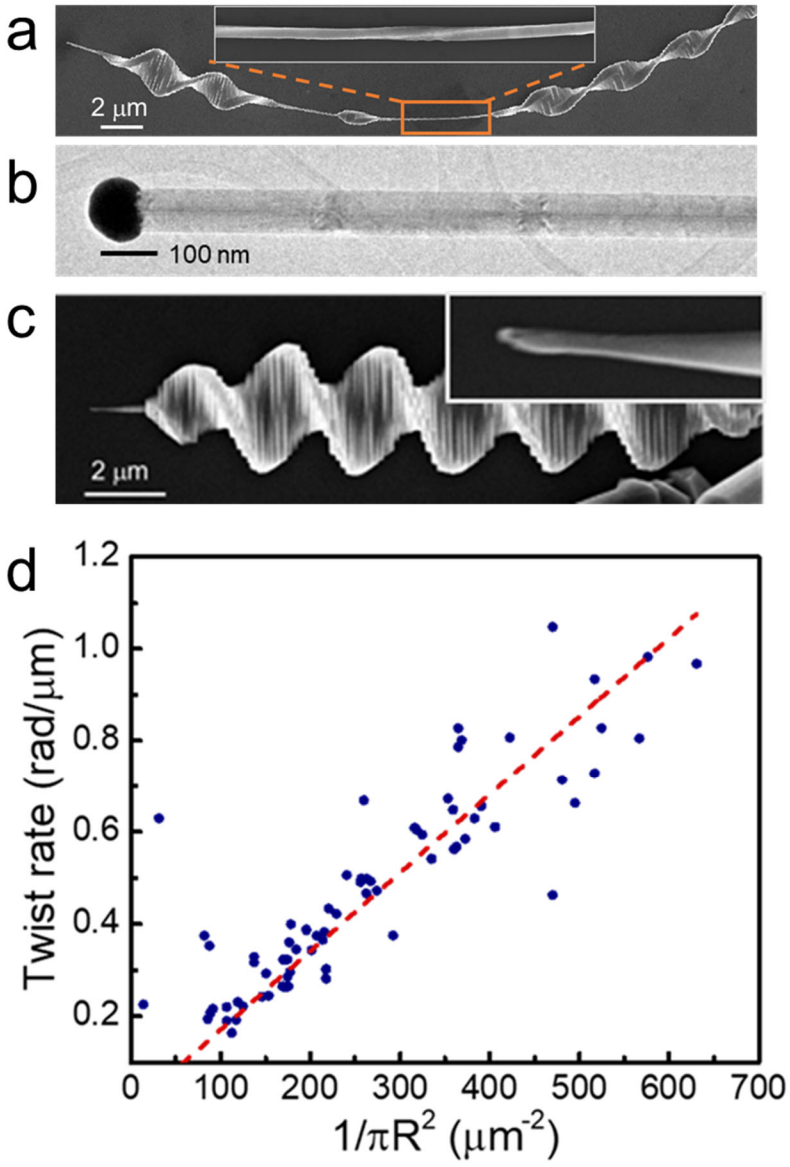

Figure 2.14 (a) SEM image of a structure with varying radial size that is formed by non-uniform growth of rotating nanoplates on a twisted nanowire. The inset of a highlights the twisting morphology of the nanowire. (b)TEM image showing the gold catalyst (black particle) at the tip of a dislocated nanowire. (c) SEM image showing a gold nanoparticle at the tip of a mesoscale twisted structure. Inset, the high-magnification SEM image showing the gold nanoparticle (bright spot) at the tip. (d)Scatterplot of twist rate measured on 73 individual twisted crystals as a function of the inversed contact areas $(\pi R^2)^{-1}$ between gold nanoparticles and the tip. The dashed red line is a least-squares linear fit through the data.

2.7 Discretized twist in the GeS

Although the Eshelby twist is essential, it cannot completely account for the discretization of the mesoscopic twist. For free-standing nanowires, radial growth increases the rigidity of the material, which counteracts the torque applied by the axial dislocation, resulting in the untwisting of the nanowire. This untwisting is in agreement with Eshelby's theory, which shows that the twist

rate inversely scales with the cross-sectional area, so that at a radius of a few micrometers, in the Eshelby model, the twist rate becomes negligible.[39] Thus, the high twist rates in the mesoscale twisted GeS that are comparable to the twist rate of dislocated nanowires cannot be interpreted through the Eshelby model alone. The key to the formation of the discretized twisting in the structure is the interaction of the dislocated nanowire with the substrate. During growth, some of the free-standing dislocated nanowires adhere to the substrate. Unlike the free-standing nanowires, further radial growth of the nanowires pinned by the substrate does not result in untwisting, and the high twist rate of the initial nanowire would thus be preserved. This invariance in the twist rate with radial growth is the mechanism that permits us to detect the Eshelby twist in mesoscale GeS (Fig. 2.14d). Our experiments (Figure 2.15) verify that the overall twist rate of a pinned structure remains almost constant with increasing radial size, and the twist rate of the mesoscale structure equals the twist rate of the initial nanowire upon substrate pinning.

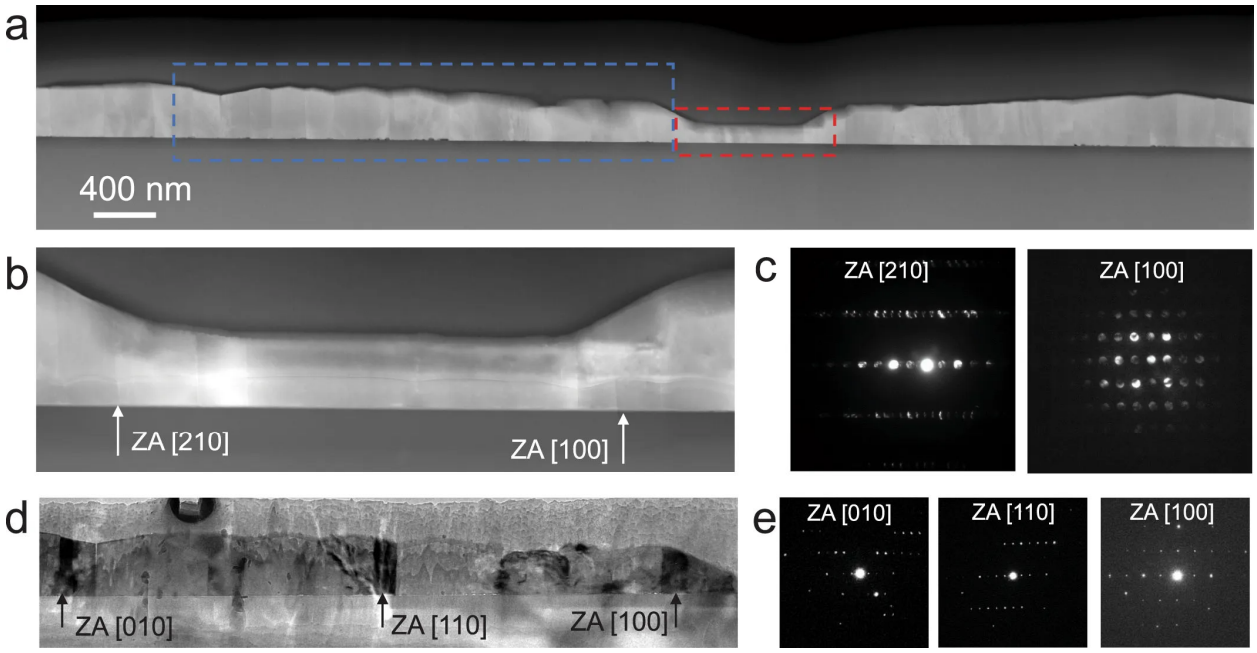

Figure 2.15 (a) STEM image of a cross-sectional sample prepared from a twisted structure pinned on a substrate. This twist structure was formed by non-uniform radial growth on a twisted nanowire (similar to the structure shown in Fig. 4a), showing varying radial sizes for different portions of the structure. To verify the invariance of the total twist rate in the radial growth of a pinned structure, we used electron diffraction to measure the twist rates of different portions with varying radial sizes in the structure. b, Magnified STEM image of a thin portion highlighted by the dashed red box in a. c, CBED patterns for the [210] and [100] zone axes collected at locations marked by arrows in b. This suggests that the thin portion has a twist of 23° over a length of 970 nm, amounting to a twist rate of 0.4 rad mm^{-1}. d, Magnified TEM image showing a thick portion highlighted by the dashed blue box in a. e, SAED patterns for the [010], [110] and [100] zone axes collected at locations marked by arrows in d. This suggests that the thick portion has a twist of 90° over a length of 4 μm, giving rise to a twist rate of 0.4 rad mm^{-1} as well. This electron diffraction analysis shows that twist rates at different portions with varying radial sizes in the structure are almost same, despite the significant difference in their radial size. Note that the thick portion has a radial size (about 450 nm) two times larger than that of the thin portion (about 150 nm). This result suggests that the overall twist rate of the structure is determined by the twist rate of the nanowire upon substrate pinning, and further radial growth does not result in untwisting that decreases the twist rate. The high twist rate of the initial nanowire with Eshelby twist is therefore preserved during radial growth.

Without the freedom to untwist, the volumetric elastic strain energy of the pinned nanowires rapidly builds up with radial growth. At a critical radial size, rotational slip of atomic layers is enabled by the weak interlayer vdW bonding in GeS to relieve the strain energy, resulting in the formation of twist boundaries and the discretization of the structure. The reduction of strain energy is counteracted by the increase in interfacial energy associated with the twisted interfaces, and this interplay defines the final twisting morphology. The elastic strain energy of the mesoscale structure is revealed by photoluminescence measurements (Figure 2.16). The photoluminescence emission peak is redshifted by 30 meV (from 748 nm to 766 nm) from the outer region, where the photoluminescence emission is consistent with the emission of strain-free GeS (1.65eV)[33], to the central region of the structure. This result indicates the existence of torsional strain around the center of the structure, in accordance with modification of bandgaps induced by screw dislocations as suggested in previous studies.[40,41]

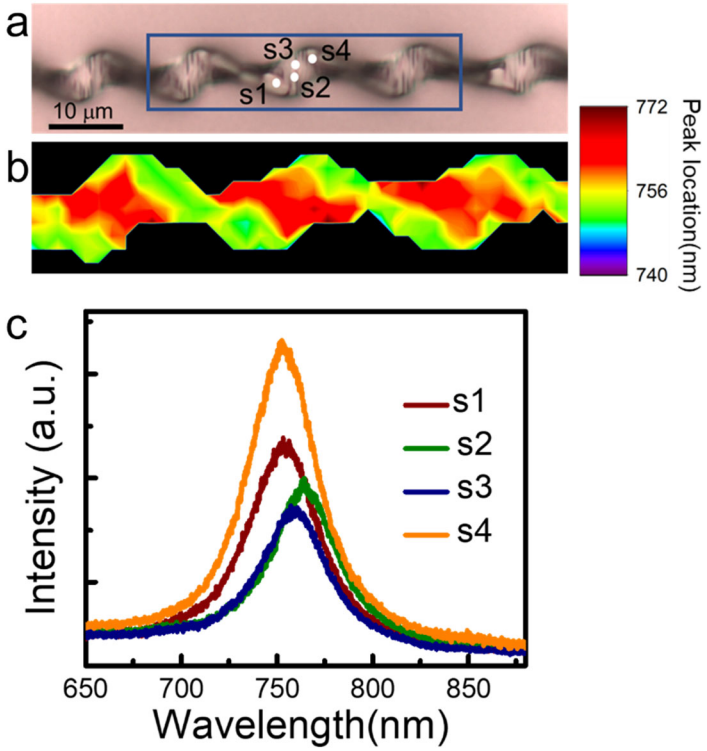

Figure 2.16 (a) Optical photo of a twisted GeS structure and corresponding photoluminescence spectral map (b) of peak wavelength position (bottom). The blue frame shows the area for the photoluminescence mapping. e, Photoluminescence spectra acquired on on spots s1 to s4 marked in (a), showing the variation of peak position.

2.8 Theoretical model

The energy competition that leads to the discretized twist can be explained using a model rooted in the Eshelby twist and the associated strain energy, the fact that the nanowires are adhered to the substrate, and the notion of a critical thickness for misfit dislocations to arise. This model was developed by our theorist collaborators Professor Daryl Chrzan and Haoye Sun in University of California Berkeley.

To illustrate this energy competition to form the discretized twist, the change in total energy, ΔE_{tot} was calculated for each segment of the nanowire of length ΔL, upon introducing a twist boundary into a pinned twisted nanowire with a twist rate defined by the initial radius of the nanowire, R_i upon its adhesion to the substrate. We propose that ΔE_{tot} has two contributions:

$$\Delta E_{tot} = \Delta E_{elastic} + \Delta E_{dis}$$

namely, a term $\Delta E_{elastic}$ due to the change in elastic energy in each segment of the wire with length ΔL and a term ΔE_{dis} due to the introduction of the misfit dislocations defining a twist boundary. The $\Delta E_{elastic}$ is found to be dependent on both the spacing between the twist boundaries ΔL and the radial size of pinned nanowire. Figure 2.17 displays ΔE_{tot} for a pinned nanowire with R_i= 36 nm as a function of ΔL for three different values of radius. The result suggests a critical radius R_c ,above which introducing twist boundaries with a finite spacing ΔL becomes energetically favorable. The critical radius depends on the initial radius, R_i that defines the twist rate of the pinned nanowire; a small initial radius corresponding to a large twist rate results in a small critical radius. The radial size of dislocated nanowires for our growth ranges from 30 to 100 nm, giving rise to critical radii ranging from 40 to 150 nm.

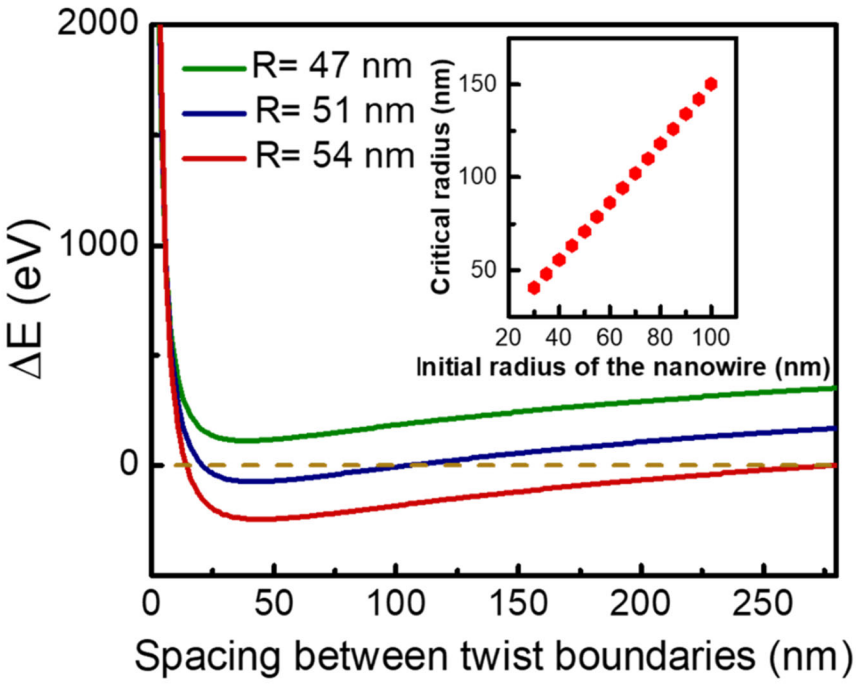

Figure 2.17 The change in the total energy for a nanowire with twist rate defined at R_i= 36 nm as a function of the spacing between the twist boundaries ΔL for three different values of nanowire radii. The inset shows the change of critical radius as a function of the initial radius R_i that defines the twist rate of the pinned structure.

2.9 Full details of the theoretical model

Full details of Chrzan and Sun's theoretical model are provided in the following.

We can build a semi-quantitative model for the process to estimate the spacing of the twist boundaries. We assume that the nanowire can, at all times, be modeled as a cylindrical wire with radius *R*. The wire grows very rapidly in the initial stages, due to the VLS process and the screw dislocation along the wires axis. The radius of the nanowire at this stage is assumed to be R_i. Growth to radii beyond that of the gold droplet, however, is much slower, and is mediated by direct deposition. The screw dislocation along the axis of the nanowire introduces a net torsion into the wire, and this torsion leads to the so-called Eshelby twist [24,25], where the twist rate of the wire, α, is given by:

$$\alpha = \frac{b_a}{\pi R_i^2} \qquad (1)$$

where b_a is the Burgers vector of the axial screw dislocation.

In the initial growth process, the wire comes into contact with the substrate and bonds to it. The result of this bonding is that the total twist rate of the wire is fixed to be given by α throughout the remainder of the growth process. As the radius of the wire increases during the growth process, the equilibrium twist rate is reduced below that of Eq. (1). However, since the wire is fixed to have a net twist rate given by Eq. 1, this leads to an excess of torsional strain energy stored in the wire. We hypothesize that this excess strain energy can be reduced by the introduction of twist boundaries into the nanowire. These twist boundaries can reduce the torsional strain energy in the cylinder, but introduces an array of misfit dislocations to define the twist boundary. The interplay between these two effects can define the critical thickness separating twist boundaries. [42]The critical distance so defined represents a lower limit on the spacing of the twist boundaries, as kinetic effects might lead to larger spacings than those predicted by the model.
We will first assume that we can model the nanowire as a cylinder of radius *R* that is growing along the z- direction. The total change in elastic energy upon introducing twist boundaries with a spacing Δl can be computed. The twist boundaries are defined by two perpendicular arrays of screw dislocations that are introduced into the wire in crossed pairs. The introduction of *n* pairs of dislocations, each with Burgers vector b_m, at a spacing $d = \frac{2R}{n}$ within the plane of the twist boundary creates a twist boundary with the twist angle, θ, given by [43]:

$$\theta = \frac{b_m}{d} = \frac{b_m}{2R} n. \qquad (2)$$

We then note that the change in elastic energy in a wire of length Δl, upon introducing the twist boundary described by Eq. (2), $\Delta E_{elastic}$, is given by:

$$\Delta E_{elastic} = -n \frac{b_a\, b_m K_s R^3}{4R_i^2} + n^2 \frac{{b_m}^2 K_s\, \pi R^2}{16\, \Delta l}. \qquad (3)$$

Here, K_s is the torsional shear modulus of the material.

The reduction in elastic energy, Eq. (3), is countered by the introduction of *n* pairs of misfit dislocations. The energy of these dislocations, E_{dis} , is taken to be, approximately,

$$E_{dis} = n \frac{R}{\pi} K_e b_m^2 \log\left(\frac{\Delta l}{\beta b_m}\right), \qquad (4)$$

with βb_m the core radius of the misfit dislocations defining the twist boundary, and K_e the elastic constant governing the line energy of the dislocation computed from anisotropic elasticity theory.[43-46] For simplicity, we take both sets of screw dislocations defining the twist boundary to have the same Burgers vector, and we assume all have the same length, $2R$.

These two contributions can be summed to give the total change in energy upon introduction of a twist boundary with n pairs of misfit dislocations [42] at intervals of Δl. We choose to measure all lengths in terms of b_m, all elastic constants in terms of K_s, and all energies in units of $K_s b_m^3$. In non-dimensional form, the expression for the change of energy, ΔE_{tot}, for wire of radius R with the twist rate fixed at a radius R_i, becomes:

$$\Delta E_{tot} = \frac{1}{16} nR \left(R \left(-\frac{4 b_a R}{R_i^2} + \frac{n\pi}{\Delta \mathrm{l}} \right) + \frac{16}{\pi} K_e \log \left[\frac{\Delta l}{\beta} \right] \right), \qquad (5)$$

where all variables now refer to their dimensionless versions.

Equation (5) enables exploration of the relationship between twist boundary spacing and the materials properties. There are only three constants that appear in Eq. (5): β, b_a and K_e. The parameter β defines the core radius of the misfit dislocations. Typically, one expects β to be the order of 1, and we choose to set $\beta = 1$. The in-plane lattice parameters of GeS (according to the Materials Project Database [46]) are given by $a_o = 0.36$ nm and $b_o = 0.44$ nm. We choose a_o to set our length scale. With this choice, the dimensionless axial Burgers vector length becomes $b_a = 2.889$.

We begin by considering ΔE_{tot} as a function of Δl, at fixed values of R_i and R. Determination of the exact value for K_e is beyond the scope of this project. Based on rough calculations, we estimate that $K_e = 3/4$. Extended Data Fig. 10 displays the change in total energy for a cylinder with dimensionless twist radius defined at radius $R_i = 100$ (i.e. 36 nm, comparable to the experiment) for three different values of R. Note that there is a critical value for R at which it becomes possible to introduce the misfit dislocations. When R exceeds this value, the dislocations can be introduced over a finite range of Δl's. This unusual dependence is simple to understand. For small Δl, the twist rate is markedly decreased through the introduction of a single twist boundary. However, as Δl grows, the average twist rate reduction due to each twist boundary decreases. The result is that if Δl is too large, the reduction in torsional strain energy due to a single twist boundary cannot be large enough to generate the dislocations of the twist boundary.

The critical Δl's predicted by the model at the critical R are too small, hovering near 30 nm, whereas the experiment indicates values nearer to 200 nm. There are many potential origins for this discrepancy, but we believe that the kinetics of misfit dislocation introduction are the most significant. Observe that for a cylinder, again with the twist radius fixed at $R_i = 100$, that with $R = 130$, introducing a twist boundary always increases the energy. However, for a cylinder of radius $R = 140$, a twist boundary can be introduced, and that for $R = 150$, it is possible to have separations between twist boundaries as high as approximately 800 in dimensionless units while still reducing the total energy. Reinserting dimensions into these equations, the model predicts that twist boundaries can be introduced into the nanowire when its radius approaches 50 nm, and by the time the wire is 54 nm in radius, the critical spacing range over which a twist boundary

would be stable, Δl, includes thicknesses ranging from 18 nm to 288 nm. It is likely that introduction of the misfit dislocations to create the twist boundaries will require the overcoming of kinetic limitations, and that the nanowire will continue to grow radially while these kinetic limitations are being overcome. Given the sensitivity to the radius of the wire, the separations agree well with the experimental observations, especially given the simplicity of the model.

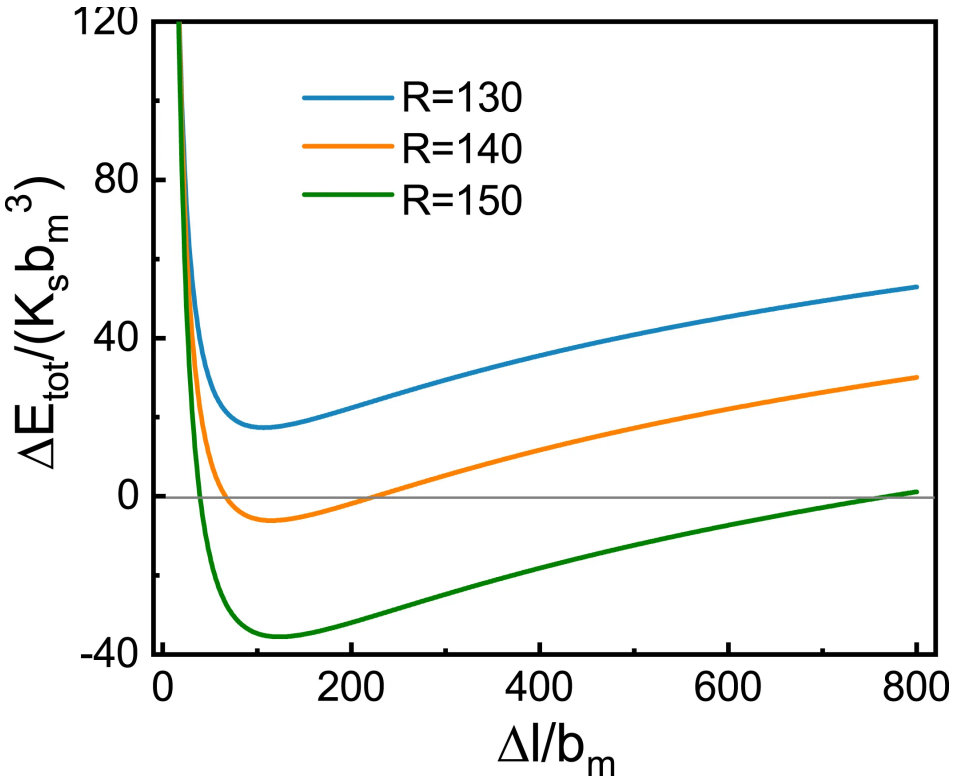

Figure 2.18 (a) The total change in energy upon introduction of one dislocation pair into a nanowire of radius R (dimensionless), given that the initial twist rate of the wire is set at $R_i = 100$. Note that for these conditions there is a critical value of R necessary to introduce misfit dislocations, as well as a critical thickness. Note also that the energy is only reduced over a range of Δl.

2.10 Evolution of the twisting topology with the radial growth

To provide further insight into the dependence of the twisting topology on the radial size of the structure, we examined a twisted nanowire pinned on the substrate with a radius of around 150nm. Since the nanowire strongly adheres to the substrate, we use FIB to prepare a cross-sectional lamellae sample to perform the TEM investigation. The nanowire is segmented with the presence of both transverse boundaries and a dislocation line in the middle, in contrast to free standing nanowires (Figure 2.11) that only has the dislocation. In contrast to the sharp orientation change and large twist angle observed in the microscale twisted structure (Figure 2.8), a very small misorientation of the crystals exists across the boundary, which is suggested by HRTEM images and the corresponding fast Fourier transform patterns (Figure 2.19b,c). In addition, we use dark-field imaging to verify that the twist in the nanowire is continuous. In Figure 2.19k, a series of dark-field TEM images shows that the [020] diffraction band progressively shifts when the sample is continuously rotated about its twist axis by tilting the TEM holder. As such, the nanostructure has both twist boundaries with very small twist angles and an almost continuous twisting profile,

exemplifying an intermediate twisting state at the onset of formation of the twist boundary.Thus, the 150 nm radial size of the nanowire approximates the critical radius to form the twist boundary. This value is in reasonable agreement with the range of critical radii calculated from our theoretical model (Figure 2.17).

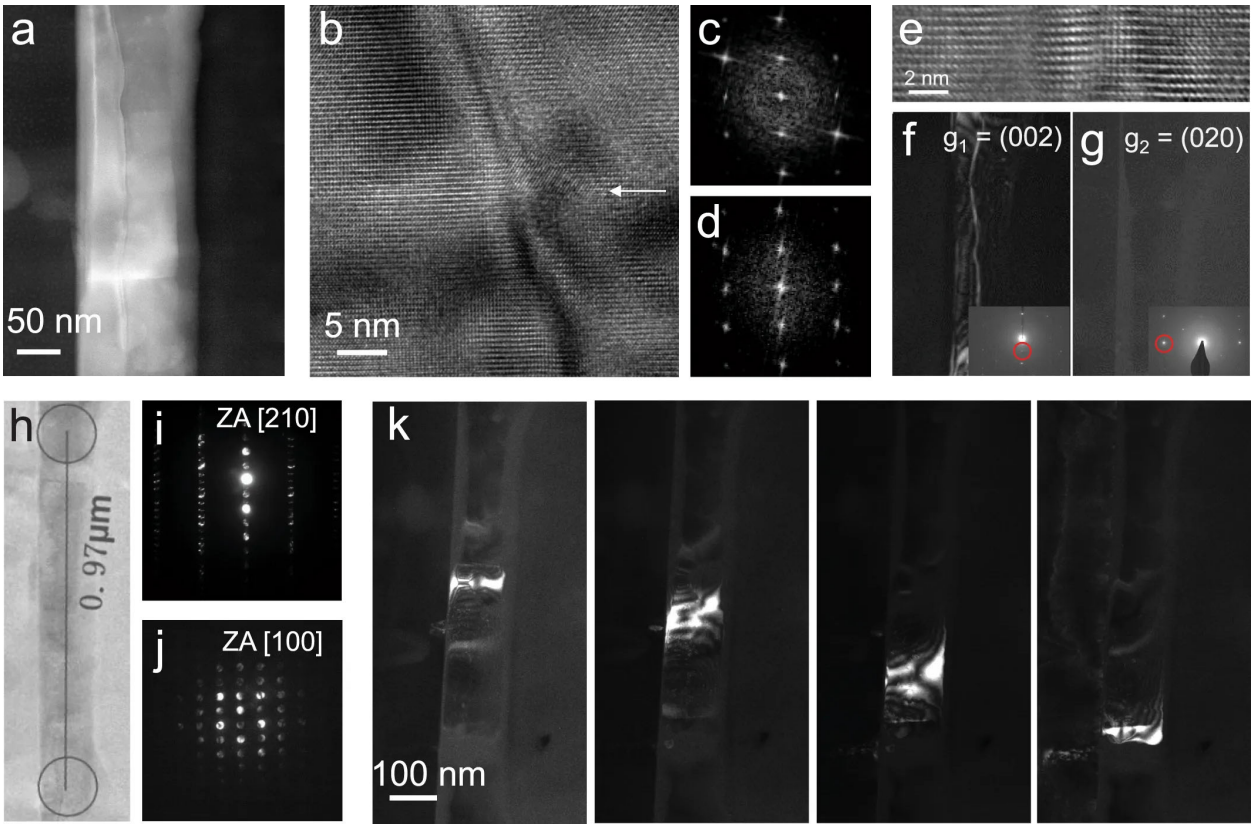

Figure 2.19 Twisted GeS nanostructure in an intermediate twisting state (a) Low-magnification STEM image of a nanostructure growing horizontally on a substrate. The nanowire had an approximate radial size of 200 nm and height of 150 nm with a twisting morphology that can be clearly observed by SEM imaging. We note that this nanostructure is the thin part of the sample shown in Figure 2.15. In contrast to free-standing nanowires (Fig. 2.11) that have only a screw dislocation, the nanowire was segmented with the presence of both transverse boundaries and a dislocation line in the middle. (b)HRTEM view of a boundary. The white arrow shows the boundary. (c) and (d) FFT patterns of the two crystals across the boundary. The HRTEM imaging and the corresponding FFT patterns confirm that the crystals across the boundary have almost the same orientation and thus the boundary takes on a very small twist angle. (e) HRTEM image of the screw dislocation. (f) , (g) Burgers vector analysis, based on the g · b contrast. To perform the analysis, the nanowire was first tilted to the [100] zone axis. Next, the sample was further tilted to create two-beam conditions for different diffraction spots in the diffraction pattern. Dark-field images of the dislocation were taken for g = (002) (f) and g = (020) (g). The insets show the excitation of reflections for the dark-field imaging in which the selected reflections are marked with red circles. For g = (002), high contrast of the dislocation is observed in the dark-field image (f), whereas for g = (020), the dislocation becomes invisible in the image (g). We have therefore determined the Burgers vector of the dislocation to be along the [001] direction, which is the same as for the dislocated nanowires that were grown vertical and free-standing. (h), Low-magnification cross-sectional TEM image of the nanowire. (i), (j) CBED patterns for the [210] and [100] zone axes are collected at locations marked by circles in a, which were separated by 970 nm. This suggests a twist of 23° about the c axis within this length, amounting to a twist rate of 0.4 rad μm^{-1}, which is comparable to the twist rate of mesoscale crystals. k, A series of dark-field TEM images showing that the [020] diffraction band progressively shifts when the sample is continuously rotated about its twist

axis by tilting the TEM holder; this dark-field imaging verifies that the crystallographic twist of the nanowire is almost continuous.

This result also reveals the gradual transition of the twisting morphology from continuous twisting to intermediate twisting consisting of both continuous twisting between the twist boundaries and discrete twisting at the twist boundaries and eventually to discrete twisting with increasing radial size (schematically shown in Figure 2.20a). The initial dislocated nanowires are continuously twisting. Then interlayer slip occurs to form twist boundaries as a consequence of radial growth of those wires adhered to the substrate and the initial axial dislocation is cut into segments by the twist boundaries.. The twist angles of those boundaries are initially small, and significant continuous twist exists within the nano-segments. Such intermediate twisting state is exemplified by the nanowire under investigation (Figure 2.19). With further radial growth, further interlayer slip occurs to enlarge the twist angle at those boundaries and the continuous twist within the nano-segments decreases. When the structure eventually grows up to a few micrometers in radial size, the twisting profile becomes almost discrete and minimal twist exists in the nanoplates. This evolution of the twisting morphology is illustrated by Figure 2.20b. This allows us to control the twisting profile and twist angles at twist interfaces by controlling the radial growth of the structure.

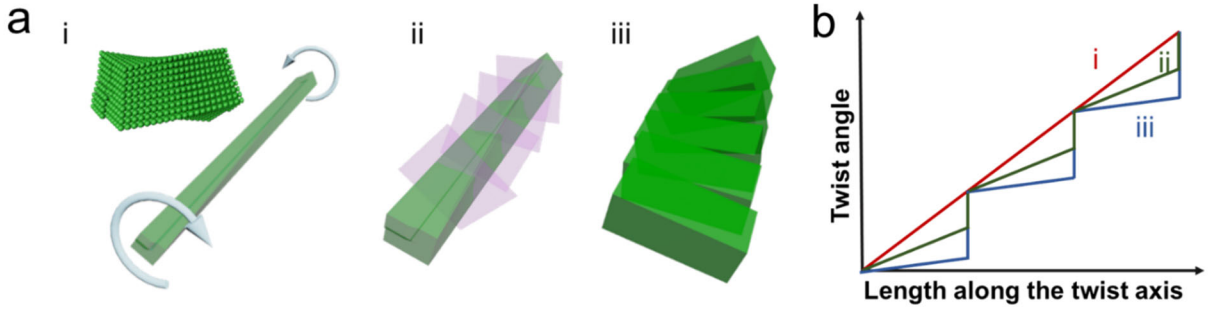

Figure 2.20 (a) Schematics showing the evolution of twisting morphology in GeS structure with increasing radial size. i, The growth of nanowire with Eshelby twist. The inset shows a schematic of the atomic structure of the Eshelby twist. ii, Interlayer slip that forms the twist grain boundary. iii, Further radial growth giving rise to the discretely twisting morphology. (b) Schematic diagram showing the twisting profile transitions from a continuous twist to a discrete twist, corresponding to states i–iii in a.

2.11 Synthesis of twisted GeSe using dislocated GeS nanowires as seeds

To demonstrate the versatility of the mechanism to form mesoscale twisted vdW structures, we successfully grew mesoscale twisted germanium selenide (GeSe) structures using twisted GeS nanowires as the seeds. The results are shown in Figure 2.21. The GeSe structures produced by the seeded growth show similar morphology with discrete twisting like the twisted GeS. SEM/EDS analysis on these structures suggest an almost 1:1 atomic ratio of Ge:Se. To synthesize the twisted GeSe structures, twisted GeS nanowires were first grown via the VLS method. Next, GeSe was deposited on the GeS nanowires in a second growth using the CVT method at a source temperature of 400°C. To achieve such seeded growth, it is crucial to minimize the exposure of the GeS nanowires to air in the procedure of sample extraction and loading to avoid the oxidation at the

surface GeS. . The synthesis of the GeSe/GeS hybrid structure further confirms the mechanism that radial growth on the dislocated nanowires fixed by the substrate gives rise to the mesoscale discretized structures. These results suggest that the discretization mechanism underpinning the formation of mesoscale twisted GeS can be used to produce other mesoscale twisted vdW structures.

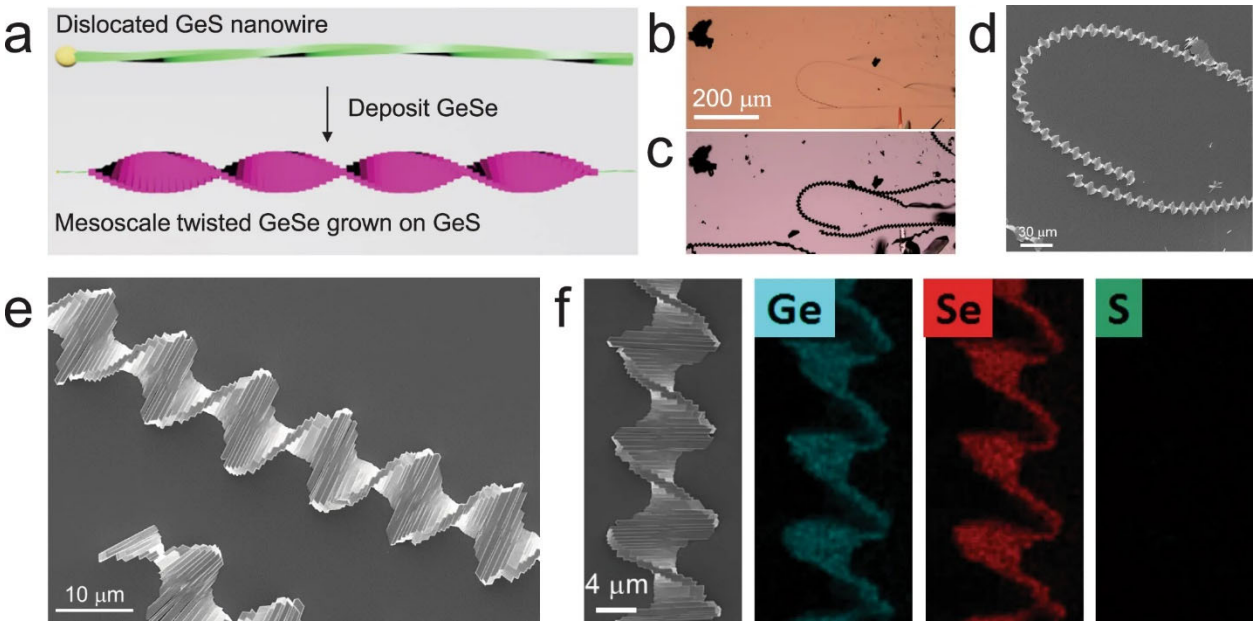

Figure 2.21 (a) Schematic showing the synthesis of mesoscale twisted GeSe structures. Twisted GeS nanowires were first grown via the VLS method. In a second growth, GeSe was deposited on the GeS nanowires using the chemical vapour transport method. (b), Optical image of dislocated GeS nanowires. (c), Optical image of mesoscale twisted structures synthesized through depositing GeSe on those twisted GeS nanowires. d, e, SEM images of twisted GeSe structures at low magnification (d) and at high magnification (e). f, SEM image (left) and corresponding EDS elemental maps of the structure. Quantitative chemical analysis using EDS suggests an almost 1:1 atomic ratio of Ge to Se.

2.12 Transfer of twisted GeS crystals to other substrates

The as-grown mesoscale GeS crystals show good adhesion to the substrate with silicon oxide surface. We developed a wet-transfer method enabling transferring those crystals to arbitrary substrates.

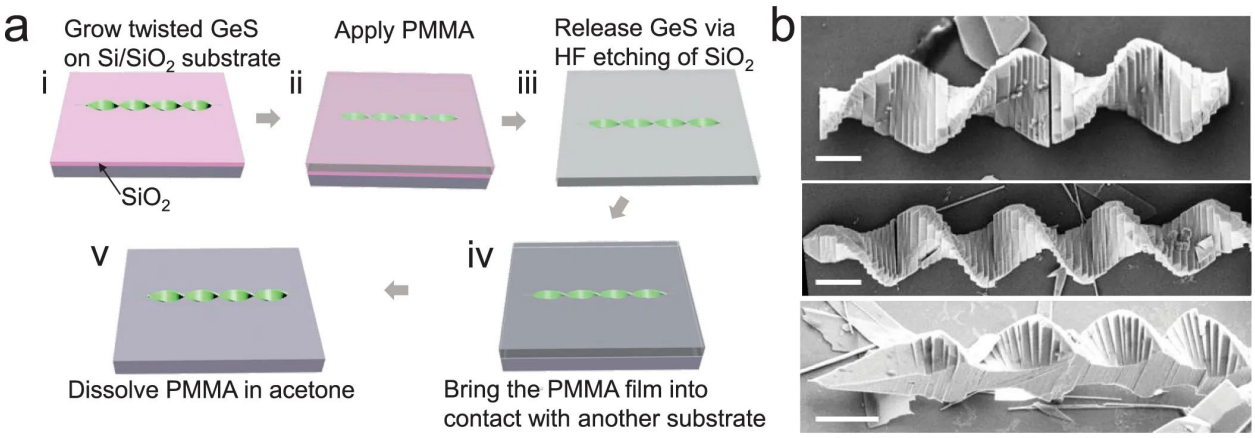

Figure 2.22 (a) Schematic showing a facile processing scheme to transfer twisted GeS crystals to other substrates. i, Twisted crystals were first grown on a thermally oxidized Si/SiO_2 substrate. These crystals adhered well to the substrate. ii, Polymethyl methacrylate (PMMA) was applied on the substrate. iii, The SiO_2 layer was etched using hydrofluoric acid, and the crystals were transferred to the PMMA film. iv, The PMMA film with the crystals was brought into contact with another substrate. v, The GeS crystals were transferred to the substrate by dissolving PMMA in acetone. b, SEM images of the GeS crystals after the transfer. Scale bar, 4 μm

Chapter 3 Chemically modulating the twist rate of helical van der Waals crystals

3.1 Motivation

Helical crystals with twisting topologies could render attractive applications in polarization optics, chiroptical sensing, enantioselective catalyst and biomedical imaging. The ability to manipulate the twist of van der Waals structures offers a new degree of freedom through which to tailor their electrical and optical properties. We synthesized twisted van der Waals GeS crystals at both the nanoscale and the mesoscale, utilizing the Eshelby twist mechanism associated with axial screw dislocations.[47] Dislocated germanium sulphide (GeS) nanowires with Eshelby twist are first grown along the van der Waals stacking direction. In Eshelby's theory, the twist rate of the dislocated nanowire is given by , $\alpha = \kappa \frac{b}{A}$, where b represents the magnitude of Burgers vector of the screw dislocation, κ is the geometrical prefactor associated with the cross-sectional shape and A is cross sectional area of the nanowire.[39] The rapid growth of those nanowires is enabled by the axial screw dislocation in combination with the VLS growth. Further growth of the dislocated nanowires attached to the substrates in the radial direction leads to the formation of mesoscale crystals with a discrete and periodic twist with atomically sharp twist boundaries. The twist rates of those twisted structures are constant during the radial growth, which is defined by the radii of nanowires first grown by the VLS process.

We previously demonstrated that the twisting topologies of the twisted GeS can be tailored by controlling their radial size. With increasing radial size, the twisting of the structure gradually transitions from continuous twisting to discrete twisting that processes twist boundaries. Tuning the twist rate and the period of those crystals has not been demonstrated. Twist rate not only affect the strain in the material but also affect the magnitude of the twist between the layers (the twist angles of the layers). Tuning the twist rate/period of those twisted crystals would enable the tailoring of numerous physics properties including optoelectronic properties, chiroptical response and thermoelectric properties.

3.2 Approach to tuning the twist rates

The twist rate and period of the twisted crystal is determined by the radii of the twisted nanowires initially grown by the VLS process. The twist rate can be therefore tailored by controlling the radii of the dislocated nanowire. This can be achieved through controlling the size of catalyst droplets that catalyses the VLS growth of the nanowires. In a typical VLS growth, a low-melting point eutectic droplet is formed; gaseous precursor species incorporate through the surface of the droplet and supersaturates the droplet, resulting in growth at the droplet-nanowire interface. The droplet acts as a channel for the VLS growth mechanism, defining the radius of the nanowire.

The supersaturation of the constituent elements comprising the nanowire in the eutectic alloy droplet is the driving force for one-dimensional growth at the growth front (the droplet-nanowire interface) significantly affecting the growth kinetics of the VLS process and the diameters of the nanowires.[48-50] The size of the droplet is correlated with the supersaturation of the elements comprising the droplet, which is known as Gibbs-Thomson effect. This correlation is

expressed by $ln\left(\frac{C_s}{C_0}\right) = \frac{4\Omega\gamma}{RTd}$, where d is the diameter of catalytic alloy droplet, γ is the average surface energy density of the droplet and Ω is molar volume of the material. This thermodynamic effect not only governs the size-dependent growth of nanowires but also limits the smallest diameter of the nanowires that can be grown using the VLS method.[48,51] Controlling the supersaturation of the elements in the alloy droplet has been previously utilized to synthesize silicon, germanium and gallium arsenide nanowires with controlled diameters. [48,51,52]

3.3 Overview

In this work, we first show that the droplets that catalyze the growth of the dislcocated GeS nanowires are binary Au-Ge alloy. The size of the alloy droplet is correlated with the supersaturation/concentration of Ge in the droplet, consistent with the Gibbs-Thomson effect. Adding GeSe into the GeS precursor in the growth increases the size of the droplets, increasing diameters of the twisted nanowires and decreasing twist rates (increasing twisting period) of the helical GeS crystals. The increase in the droplet size results from the increase in the surface energy of the droplets with the presence of GeSe. The addition of GeSe significantly modulated the supersaturation of Ge in the alloy droplet. In contrast to the growth of pure GeS nanowires, different dependence of droplet size on the concentration of Ge in the droplet was identified for growth using GeSe. Analysis based on the Gibbs-Thomson effect further confirms that the adding GeSe increases the surface energy of the droplets. Increasing the Se concentration from x=0 to x=0.11 in the $GeS_{1-x}Se_x$ decreases the twist rate from 0.59 rad/μm to 0.22 rad/μm, increasing the period from 8μm to 15 μm. The chemical modulation demonstrates good potential to tailor the twist rates of helical vdW crystals, enabling a new freedom to modulate optoelectronic properties and chiral light-matter interactions.

3.4 Synthesis

The growth of twisted GeS was performed using the same method used in our earlier work. Slightly different growth parameters were used for the CVD growth though. GeS (Sigma-Aldrich) was used as source material. Si (100) wafers with 3 nm thick gold that are patterned into bars were used as the substrates. The furnace was pumped and flushed with forming gas (4% H_2 in Ar) for several times to approach a minimal base pressure of 5 mTorr before each growth. During the growth, the mixture powder at the center of the tube was heated to sublimate at a given pressure. The substrates were placed 10-12 cm downstream from the source material. The parameters for growth were pressures of 1-2 Torr, mass flow rates of 20-50 standard cubic centimeter (sccm), source temperatures of 450 °C, deposition temperatures of 430 °C and a growth time of 20 minutes.

The growth of twisted $GeS_{1-x}Se_x$ was performed using the same growth parameters as the twisted GeS except that the source materials were mixtures of GeS and GeSe.. The source material, GeS (Sigma-Aldrich) and GeSe (BOC sciences) powder were weighed and mixed according to stoichiometry of $GeS_{1-x}Se_x$ (x=0~0.06). The chemical compositions of product are related to but different from the chemical composition of the source mixture. For the sake of convenience, we refer the chemical compositions of product using the chemical composition of the mixture, which is so called normal composition of the product.

3.5 Twisted GeS nanowires and the size-dependent composition of the droplets

Our synthesis conditions yield GeS nanowires with a growth direction along the [001] direction. Almost all nanowires have an Eshelby twist. Figure 3.1 presents TEM characterization of a representative GeS nanowire. Convergent beam electron diffraction （CBED） analysis shows that the crystal orientation of the wire rotates 34.3 degree of rotation from [100] direction to [120] direction along the c-axis over an approximate distance of 0.968 micrometer. This gives rise to a twist rate of 0.61 rad/μm. High resolution TEM imaging (Figure 1c) confirms that the growth direction of the nanowire is along [001] direction with a screw dislocation in the middle of the wire.

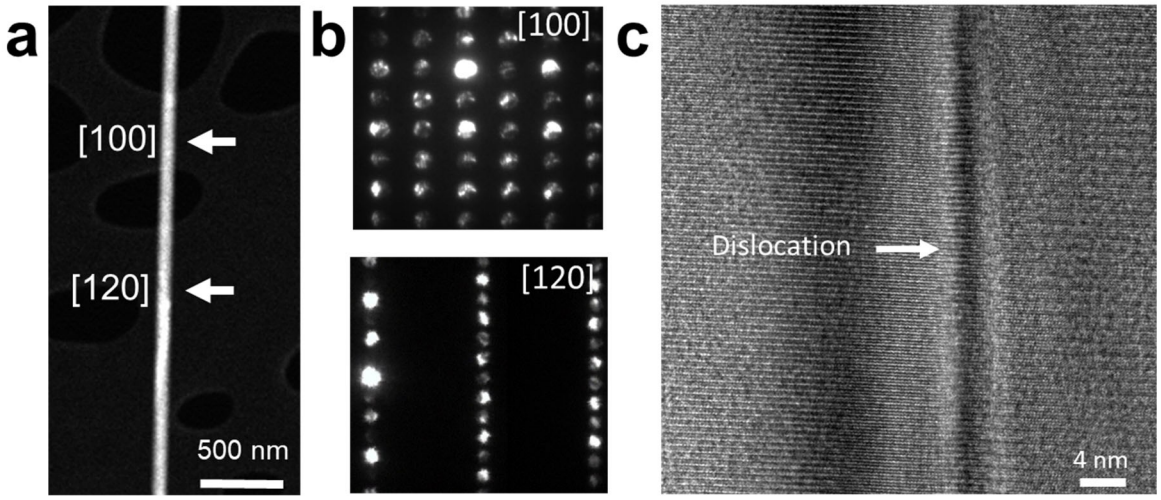

Figure 3.1(a)STEM image of the GeS nanowire with an Eshelby twist . (b)CBED patterns taken at different locations suggesting that the crystal orientation changes from the [100] direction to the [120] direction. The locations where those CBED patterns were obtained are marked with white arrows in (a). Note there is a rotation of the CBED pattern with respect to the orientation of nanowire. (c) HRTEM image of the dislocation in the GeS nanowire.

Those twisted GeS nanowires were growth by the VLS process and the diameter of those nanowires were defined by the size of the catalyst droplet. A thorough understanding of the catalyst droplet would provide crucial insights into engineering the diameters and the twist of the nanowires. We thus performed chemical analysis on the catalyst droplet of those nanowires. Figure 3.2 shows a representative high-angle annular dark-field scanning transmission electron microscopy (HAADF-STEM) image of a VLS grown GeS nanowire. The catalyst seed at the tip of the wire is evident by the different Z-contrast arising from different chemical compositions in comparison to the nanowire. Quantitative scanning transmission electron microcopy-energy dispersive X-ray spectroscopy (STEM-EDS) analysis suggests that the wire consists of Ge and S with an approximate ratio of 1:1 whereas the catalyst seed is a binary Au-Ge alloy with 33.9 atom.% Ge and 66.1 atom.% Au (Figure 3.2b). The inset image in Figure 3.2b highlights the energy window in the EDS spectrum where the K-α EDX peak of sulfur (centered at 2.3 keV) is covered. No sulfur is detected, suggesting a low-solubility of sulfur in the catalyst seed. This finding is consistent with a number of studies on the Au-catalyzed growth of other compound semiconductor nanowires including GaSe[53], GaAs[54,55] and CdS/CdSe/CdTe[56] NWs. The catalyst seeds in those

studies were determined to be either binary Ga-Au or Cd-Au alloys with low solubility of anions (Se, As, S or Te). However, our results starkly contrast a previous study on the VLS growth of the GeS nanowires, which suggests that the catalyst is a ternary Au-Ge-S alloy.[57]

Our chemical analysis further reveals the dependence of the diameter of the GeS nanowires on the Ge supersaturation/concentration in the catalyst droplet. The dependence was established through EDS analysis on a number of catalyst droplets on GeS nanowires. Figure 3.3 shows the change in droplet size versus the Ge concentration in the droplet, showing that Ge concentration of the catalyst particle drops with increasing size. The result can be understood by the fact that in a binary Ge-Au droplet, the droplet size is correlated to Ge concentration with the size of droplet (eq.(2)) through the Gibbs-Thomson effect.

$$ln\left(\frac{C_{Ge}}{C_0}\right) = \frac{4\Omega\gamma}{RTd} \text{ or equivalently, } \ln C_s = lnC_0 + \frac{4\Omega\gamma}{RT}\cdot\frac{1}{d}$$

where d is the diameter of catalyst droplet, γ is the average surface energy of the droplet and Ω is molar volume of the material, C_{Ge} is the concentration of Ge in the droplet and C_0 is the equilibrium concentration of Ge. The results are good fit to the Gibbs-Thomson equation as is suggested by the good the linear relationship between $\ln C_{Ge}$ and 1/d, as is shown in the inset of Figure 3.3. In the fitting, we use a molar volume of Germanium ($\Omega=2.26\times10^{-23}cm^3$)13, R of 8.314 $J\cdot mol^{-1}\cdot K^{-1}$ and temperature of T=703 K at substrate. This leads to $\gamma=0.51\times10^{-4}$ $J\cdot cm^{-2}$ and C_0=28.2%. The correlation between the Ge concentration in the droplet and the droplet size that defines the diameter of the nanowires indicates that the droplet sizes and nanowire diameters could be engineered by tuning the supersaturation of Ge in the droplet.

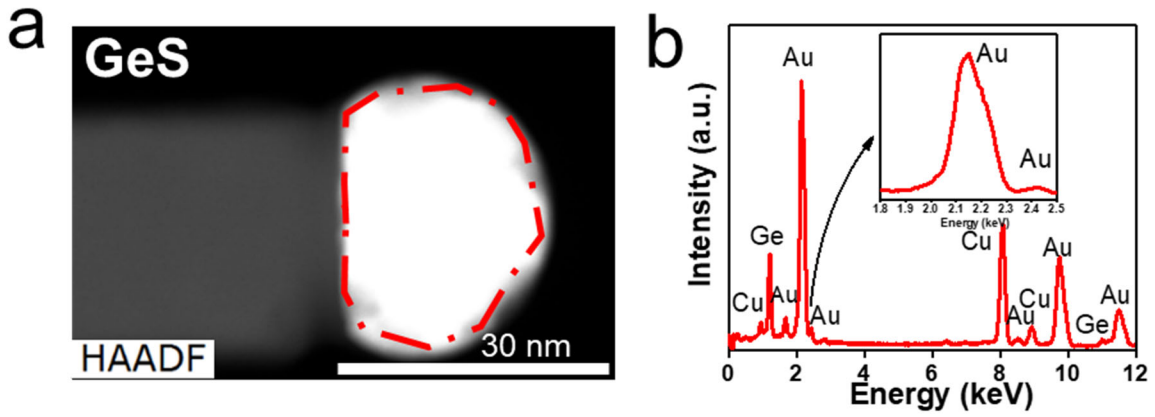

Figure 3.2 (a) HAADF-STEM image of a twisted GeS nanowire with a catalyst droplet, and (b) corresponding EDS spectra obtained from the highlighted area of the catalyst droplet, giving rise to a composition of 66.1 atom. % Au and 33.9 atom. % Ge. The copper signal in the spectrum is from the copper TEM grid.

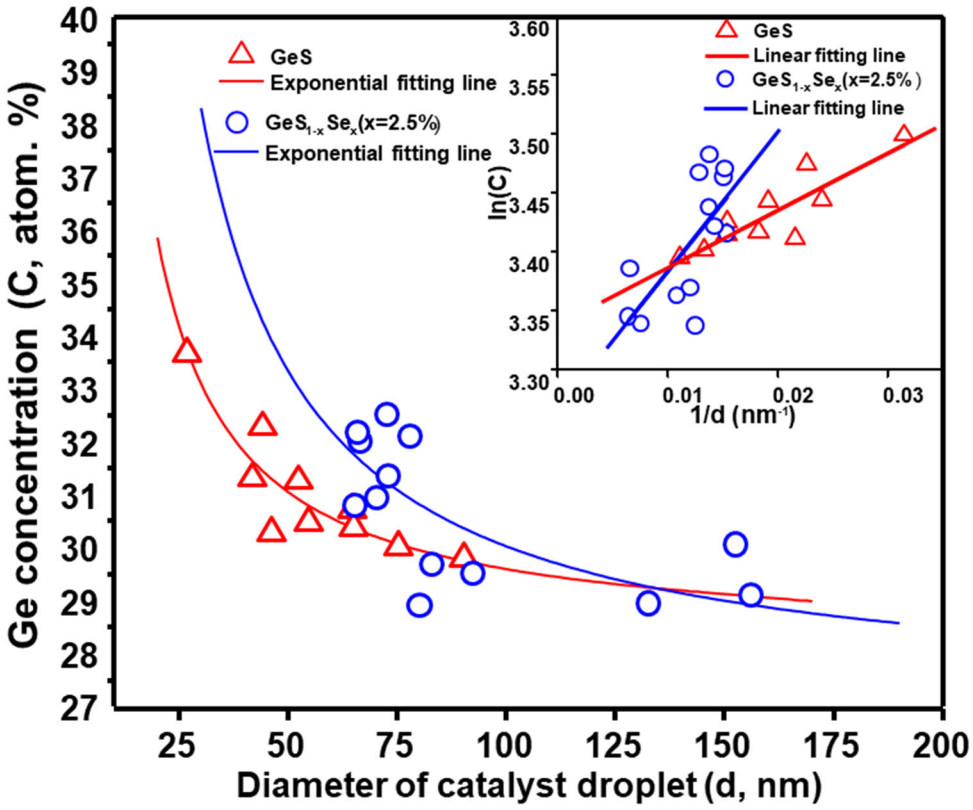

Figure 3.3 Ge concentrations (in atomic %) of the catalyst droplets at the tip of GeS nanowires and $GeS_{1-x}Se_x$ nanowires versus the diameters of the catalyst droplet. Measured concentrations for GeS and $GeS_{1-x}Se_x$ nanowires are shown with red triangles and blue circles respectively. Red and blue lines are fits for GeS nanowires and $GeS_{1-x}Se_x$ nanowires based on the Gibbs-Thomson effect, $C_{Ge} = C_0 exp\,(\frac{4\Omega\gamma}{RTd})$ (see text). The inset shows lnC_{Ge} versus $\frac{1}{d}$. The linear fits are based on $lnC_s = lnC_0 + \frac{4\Omega\gamma}{RT} \cdot \frac{1}{d}$

3.6 $GeS_{1-x}Se_x$ nanowires

The addition of GeSe into the source material yields $GeS_{1-x}Se_x$ nanowires. Our chemical analysis reveals a difference between the composition of source material (the nominal composition) and composition of the synthesized $GeS_{1-x}Se_x$ nanowires. Figure 3.4 shows the chemical analysis of a $GeS_{1-x}Se_x$ nanowire produced at a source composition of $GeS_{0.95}Se_{0.05}$ using a scanning transmission electron microcopy-energy dispersive X-ray spectroscopy (STEM-EDS). The nanowire shows a uniform distribution of Ge, S and Se, with a composition of 51.67 atom. % Ge, 5.61 atom. % Se and 42.72 atom. % S, corresponding to $GeS_{0.88}Se_{0.12}$. The analysis suggests that the concentrations of Se in the $GeS_{1-x}Se_x$ nanowires are higher than the concentration of Se in the precursor. We speculate that the difference between the composition of nanowires and the composition of source material results from vaporization of the precursor. The composition of vaporized gaseous precursors may deviate from the composition of the source material; at the source temperature, the vapor pressure of GeS and GeSe may not scale with the composition of the GeSe and GeS in the source material. Despite this difference, we refer to the growth product based on the composition of GeSe in the source material rather than its actual composition for the

sake of convenience since the composition of $GeS_{1-x}Se_x$ nanowires is correlated with the composition of the source material.

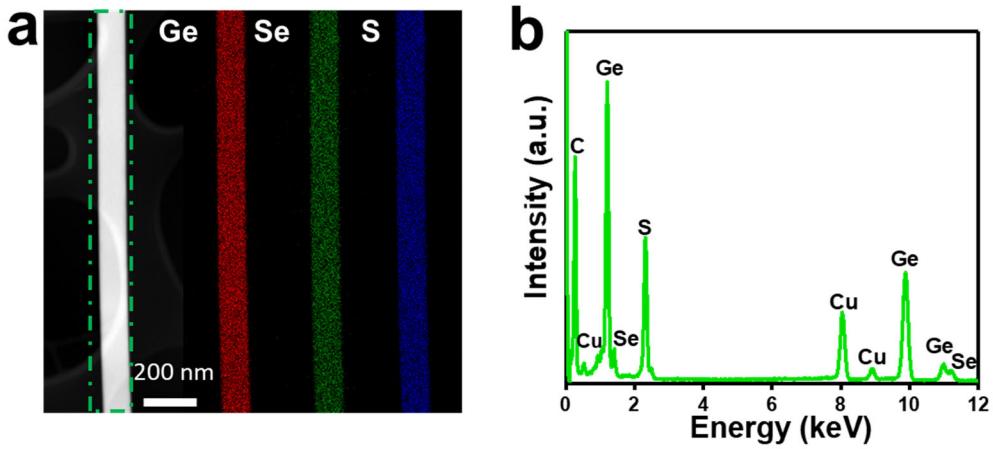

Figure 3.4 (a)Representative HAADF-STEM image of a nominally $GeS_{0.95}Se_{0.05}$ twisted NW and EDX mappings of the $GeS_{0.95}Se_{0.05}$ twisted NW showing the uniform distribution of Ge (blue), Se (red), and S (green). (b) EDS spectrum collected from area highlighted by the green dashed box in (a), yielding a composition of 51.67 atom. % Ge, 5.61 atom % Se and 42.72 atom % S.

$GeS_{1-x}Se_x$ nanowires retain the structure and growth direction of the GeS nanowires. This could be understood given the fact that GeSe is isostructural with GeS. Figure 3.5 shows the crystal structure of GeSe which is in the same space group as GeS, Pcmn. Like the GeS nanowires, almost all $GeS_{1-x}Se_x$ nanowires have Eshelby twist as well. Figure 3.6 show the TEM studies of a representative twisted $GeS_{1-x}Se_x$ nanowire produced at a nominal composition (source composition) of $GeS_{0.95}Se_{0.05}$, which verifies the existence of an axial screw dislocation in the middle of the wire. CBED analysis (Figure 3.6b) confirms the Eshelby twist in the nanowire. The crystal orientation rotates 23.8 degree of rotation from [120] direction to [210] direction along the c-axis over an approximate 184 distance of 1.3 micrometer. This twist rate of 0.32 rad/μm is significantly smaller than that of the twisted GeS nanowire (Figure 3.1)

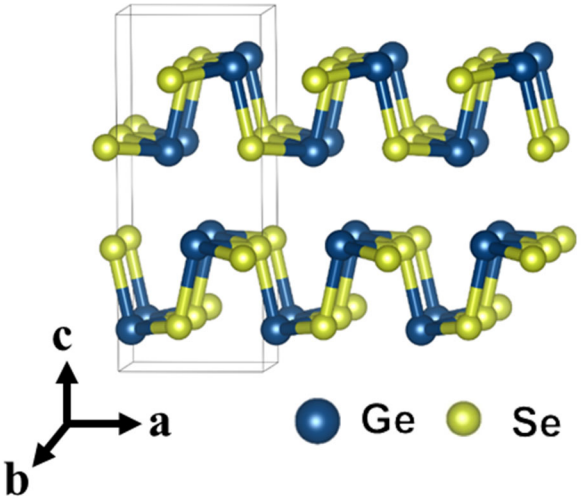

Figure 3.5 Crystal structure of layered GeSe. The box denotes the unit cell.

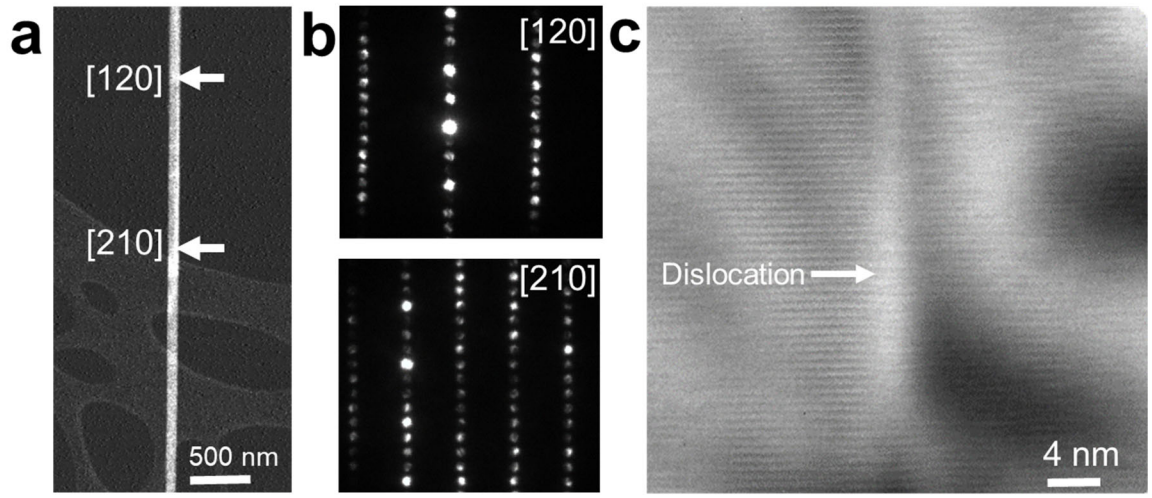

Figure 3.6 Twisted $GeS_{1-x}Se_x$ wire. (a) STEM image of a $GeS_{1-x}Se_x$ wire produced at the nominal composition of $GeS_{0.95}Se_{0.05}$ nanowire . (b)CBED patterns taken at different locations suggesting the crystal orientation aligned with electron beam changes from the [120] direction to the [210] direction. (b) HRTEM image of the dislocation in the $GeS_{0.95}Se_{0.05}$ nanowire.

3.7 Modulation of droplet sizes by adding Se in the growth

The addition of GeSe into the GeS precursor yields twisted $GeS_{1-x}Se_x$ nanowires with increasing diameters. Chemical analysis on the catalyst droplet of the $GeS_{1-x}Se_x$ nanowires reveals the mechanism for the chemical modulation of the nanowire diameters. Representative STEM-EDS analysis $GeS_{0.95}Se_{0.05}$ nanowire are shown in Figure 3.7. The catalyst droplet of the $GeS_{1-x}Se_x$ nanowire is a nanoparticle of binary Ge-Au alloy, with no detectable sulfur or selenium (Inset of Figure 3.7b), which is consistent with the result obtained from pure GeS wire. The size of the catalyst particle (154 nm in diameter) in the $GeS_{0.95}Se_{0.05}$ wire is significantly larger than the size of the catalyst particle in the GeS wire (27 nm). Interestingly, EDS analysis shows that the catalyst particle in $GeS_{1-x}Se_x$ wire has a Ge concentration of 27.8 atom%, which is lower than the Ge concentration (33.9 atom%) in the catalyst particle of GeS wire. These results imply that the adding GeSe into the precursor modulates the size and chemical composition of the Au-Ge catalyst particle, although no detectable selenium incorporates into the catalyst particle.

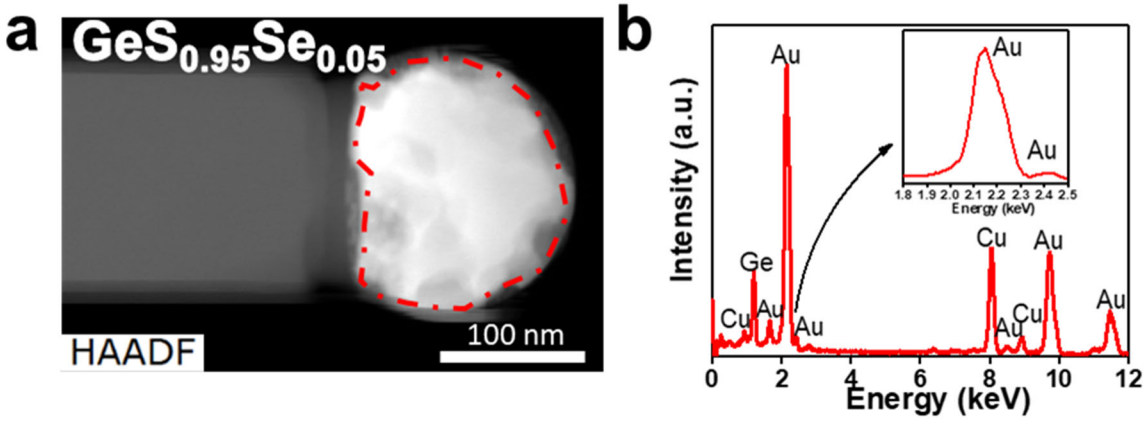

Figure 3.7 (a) Representative HAADF-STEM image of $GeS_{1-x}Se_x$ with a catalyst droplet, and (b) corresponding EDS spectra obtained from the highlighted area of the catalyst droplet, yielding a composition of 72.2 atom. % Au and 27.8 atom. % Ge. The copper signal in the spectrum is from the copper TEM grid. The $GeS_{1-x}Se_x$ nanowire was synthesized at a source composition of $GeS_{0.95}Se_{0.05}$.

In contrast to GeS nanowires, $GeS_{1-x}Se_x$ nanowires have different dependence of their droplet sizes on the Ge supersaturation/concentration in the droplets. We measured the chemical composition of a number of catalyst particles on $GeS_{1-x}Se_x$ nanowires produced at a nominal concentration of $GeS_{0.975}Se_{0.025}$. The dependence of the Ge concentration on the droplet size is shown in Figure 3.3. In contrast to GeS, the Ge concentration in the droplet of $GeS_{1-x}Se_x$ nanowires changes faster with droplet sizes, as is suggested by a steeper slope in the plot of $\ln C_{Ge}$ versus 1/d. The fitting using the Gibbs-Thomson equation gives rise to a surface energy of 1.11×10^{-4} J·cm^{-2} which is larger than the surface energy extracted for the droplets of GeS nanowires. However, the equilibrium concentration of germanium is almost same as the result obtained for GeS nanowires (C_0=28.2%.). The chemical modulation of the droplet sizes is therefore attributed to the increase in the surface energy due to the presence of GeSe. The increased surface energy promotes the formation of alloy droplets with larger sizes, which could occur via particle coalescence or Ostwald ripening. To verify this, we performed growth using $GeS_{1-x}Se_x$ precursors with increasing concentrations of GeSe. These growths were intentionally performed using a shortened growth time (5 minutes) such that alloy seed particles were formed while almost no nanowires were grown. Figure 3.8 shows the SEM images and size distribution of the alloy catalyst particles synthesized at different GeSe concentrations. With no addition of the GeSe, the distribution shows a single peak at 20 nm. With increased GeSe concentration to be $GeS_{0.975}Se_{0.025}$, the peak in the size distribution increased to 34 nm. Further increasing concentration to be $GeS_{0.95}Se_{0.05}$ gives rise to a binodal distribution with a small peak appearing on right the side of the large peak (Figure S5f). This binodal distribution can be well fitted by a log-normal function (peak at 36 nm) and Gaussian function (peak at 53 nm) which suggests that particle coalescence and Ostwald ripening account for the increased particle sizes.[58] This result implies that GeSe increased the surface energy of the

catalyst droplet in the course of the VLS growth of the nanowires, increasing the size of droplets and modifying the supersaturation of Ge in the droplets.

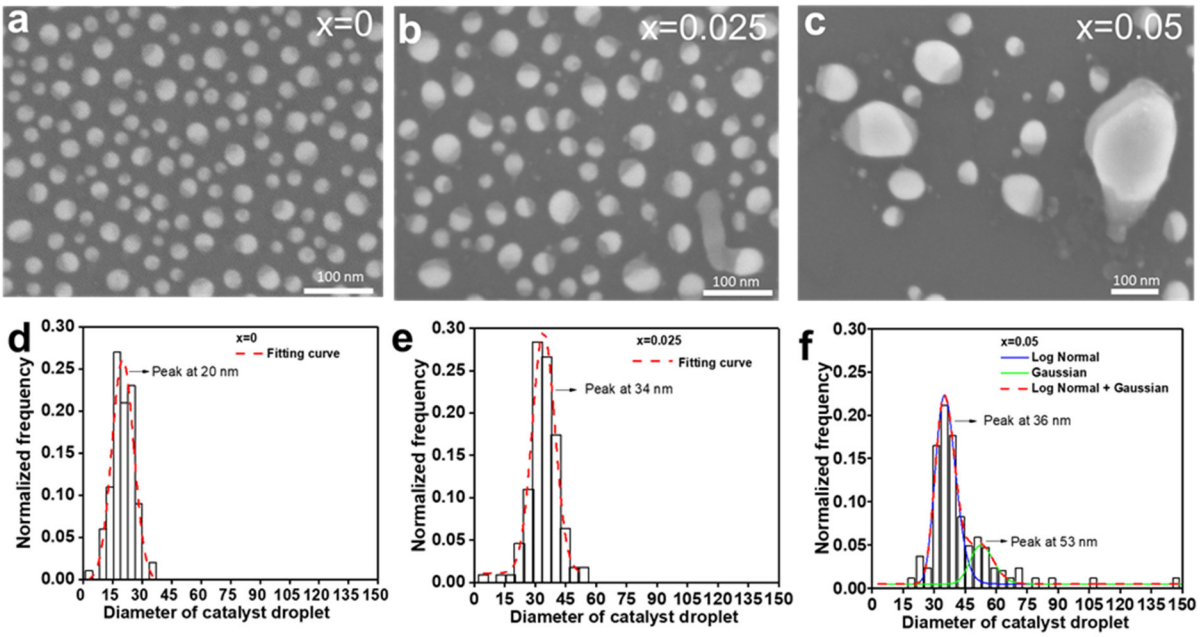

Figure 3.8 Representative SEM images of the catalyst droplets on the silicon substrates formed with a reaction time of 5 minutes in response to the source materials with different compositions of GeSe (a) GeS, (b) $GeS_{0.975}Se_{0.025}$ and (c) $GeS_{0.95}Se_{0.05}$. (d-f) Corresponding histograms showing the diameter distribution of the nanodroplets for GeS(d), $GeS_{0.975}Se_{0.025}$ (e) and $GeS_{0.95}Se_{0.05}$ (f); Dashed curves show the fits using the combined log-normal-Gaussian function.

3.8 Chemical modulation of the twist rates of helical $GeS_{1-x}Se_x$ crystals

The modification of the diameter and twist rate of the twisted vdW nanowires by GeSe is unambiguously verified by the varying twisting period of the mesoscale structures resulting from the twisted nanowires. Those mesoscale structures are $GeS_{1-x}Se_x$ alloy crystals created by following radial growth of the twisted alloy nanowires fixed to the substrate. Since those nanowires are fixed by the substrate, further radial growth of the nanowires would not lead to untwisting, and the total twist rate of the nanowires is preserved in the mesoscale structure. The twist rate of the mesoscale crystals is therefore defined by the twist rate of the nanowires.

The twist rates of those mesoscale crystals are determined from the number of nanoplates or interfaces per period formed, given the fact that one period (The distance between adjacent locations with minimum widths) corresponds to a cumulative twist angle of 180º.[59] Figure 3.9a displays the twist rates and periods of the mesoscale crystals versus the concentration of GeSe in the $GeS_{1-x}Se_x$ precursor (nominal composition). The results are generated by analyzing the periods of over 100 structures for each nominal composition. With the nominal concentration of the GeSe increasing from 0 to 5 mol.%, the average of the twisting period increases from 8 μm to 15 μm and the average of twist rates reduces from 0.59 rad/μm to 0.22 rad/μm. Figure 3.9b shows SEM images of representative $GeS_{1-x}Se_x$ structures produced at three different normal compositions of GeSe, showing increased periodicity with increasing Se concentration. The mesoscale $GeS_{1-x}Se_x$ crystals possess discrete twisting like the mesoscale twisted GeS crystals in which twist boundaries are present. The twist angles of those twist boundaries of $GeS_{1-x}Se_x$ crystals have been evaluated by counting the number of twist interfaces per period. The results suggest that the distribution of twist angles of those twist boundaries does not significantly vary with the addition of GeSe, as shown in Figure 3.10.

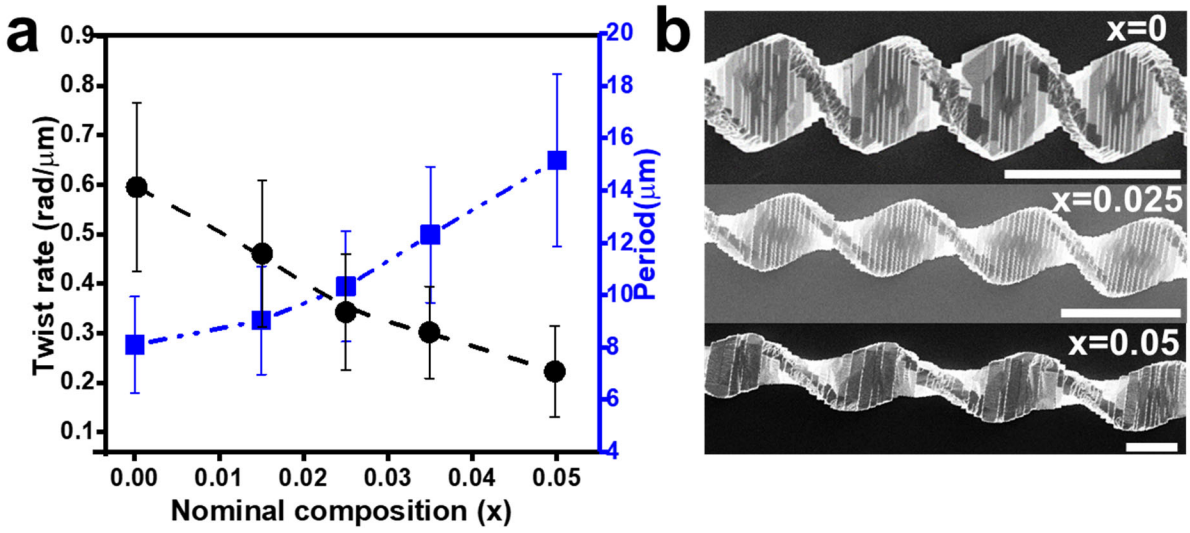

Figure 3.9 (a) Twist rate and twisting period of mesoscale $GeS_{1-x}Se_x$ as function of GeSe composition. For each data point, more than 100 samples were measured, and the error bars represent the standard deviation. (b) Representative SEM images of mesoscale $GeS_{1-x}Se_x$ (x=0, 0.025, 0.05). Scale bars are 10 μm.

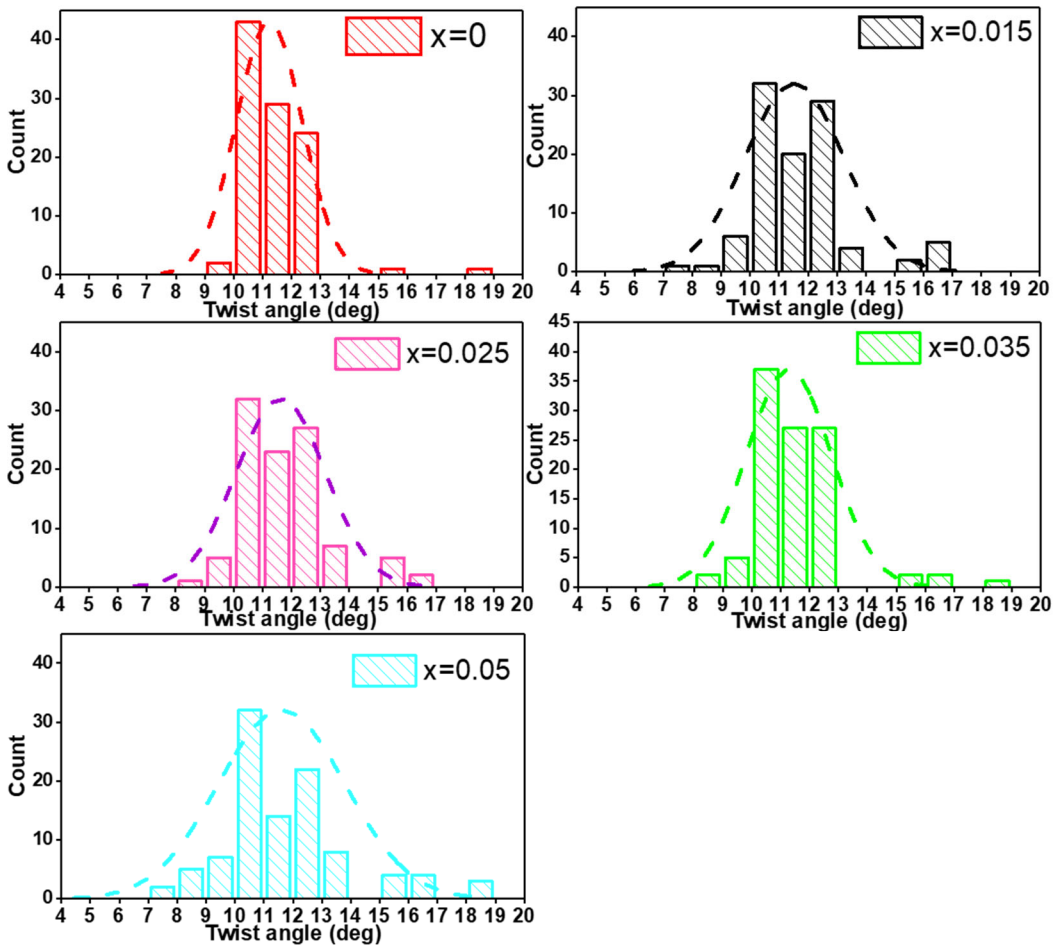

Figure 3.10 Distribution of twist angles in mesoscale $GeS_{1-x}Se_x$ crystals with different compositions.

The decreased twist rate of the mesoscale $GeS_{1-x}Se_x$ structures suggests the reduced twist rates of the dislocated $GeS_{1-x}Se_x$ nanowires. At the tip of most mesoscale structures, catalyst particle that first catalyzed the growth of the dislocated nanowires are still present (Figure 3.11a,b). The size of the particle at the tip well approximates the diameter of the nanowire defining the twist rate.[59] The correlation between the size of the catalyst particle and the twist rate has allowed us to detect the Eshelby twist in the twisted GeS structures. Figure 3.11c shows that the diameters of the catalyst particles at the tip of the mesoscale structures increase with increasing compositions of GeSe. With nominal concentration of the GeSe increasing from 0 to 5 mol.%, the average diameter of the catalyst particle significantly increases from 87 nm to 156 nm. The increase in the catalyst droplet size suggests the increase in the diameter of the dislocated nanowires grown by the VLS process, which is consistent with the decrease in the twist rate of the Eshelby twist. This result clearly demonstrates that adding GeSe in the growth modulates the size of the droplet catalyzing the VLS growth of nanowires with the Eshelby twist.

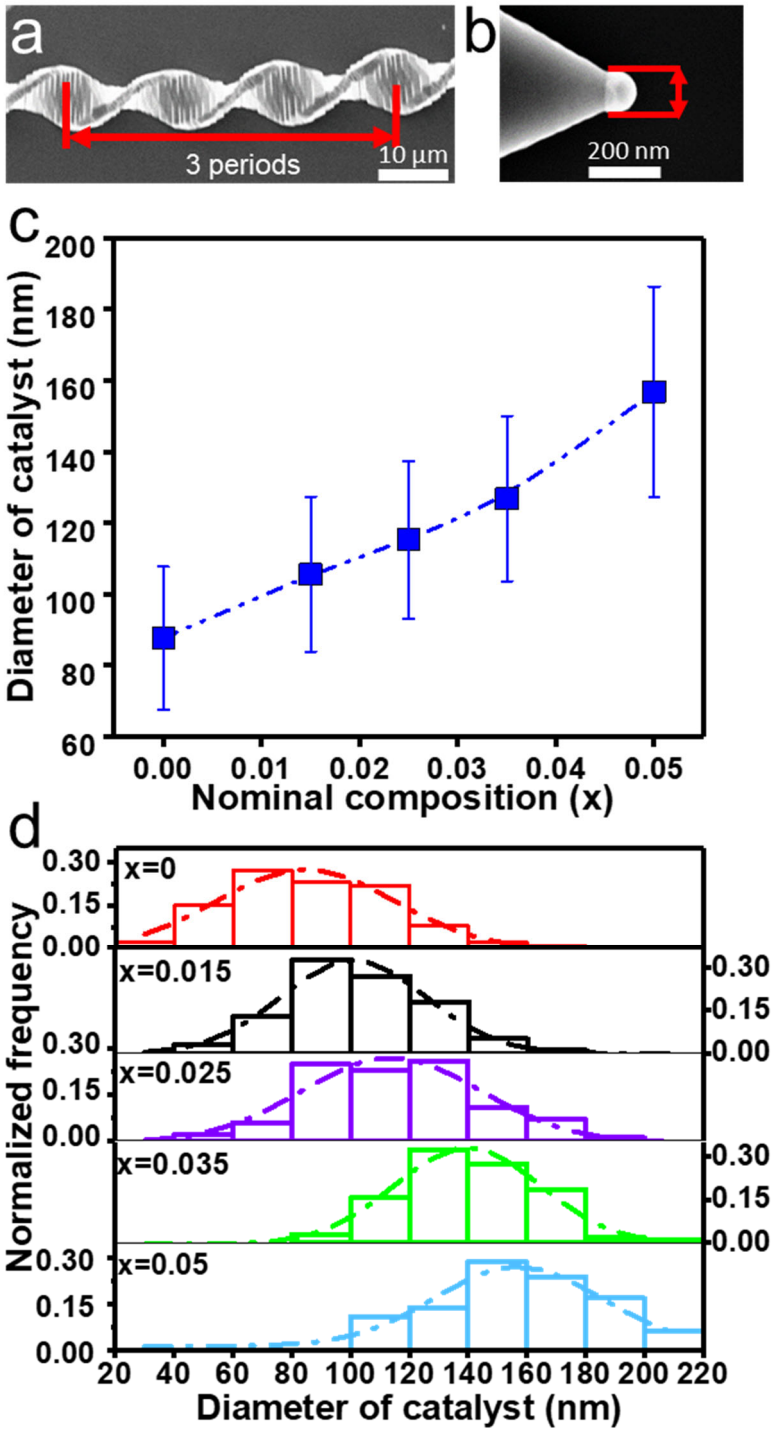

Figure 3.11 (a) SEM image of a mesoscale $GeS_{1-x}Se_x$ structure with a nominal composition of $GeS_{0.95}Se_{0.05}$. (b) SEM image of the Au-Ge alloy particle at the tip of the structure shown in (a). The diameter of the particle is marked by a red arrow (c) Diameter of the catalyst particle at the tip of mesoscale $GeS_{1-x}Se_x$ structure as a function of GeSe compositions. For each data point, more than 100 samples were measured, and the error bars represent standard deviation. (d) Histogram showing the diameter distribution of catalyst particles for mesoscale $GeS_{1-x}Se_x$ structure with different GeSe concentrations.

We further established the correlation between the twist rate in the mesoscale $GeS_{1-x}Se_x$ structures and the inversed contact area between the catalyst particle and the tip. Good linear fits are observed for $GeS_{1-x}Se_x$ structure synthesized at different nominal compositions of GeSe (Figure 3.12a-e), which allows us to extract magnitude of κ•b (The product of geometric prefactor with the magnitude of the Burgers vector) based on Eshelby's theory. The obtained magnitudes of κ•b are in a reasonable range of 0.88~1.2 nm (Figure 3.12f), which is consistent with one lattice constant along the c-axis (c=1.04 nm). Given that κ has a value close to 1, these magnitudes agree with the basic understanding that the Burgers vector is the shortest lattice vector which reduces the elastic energy. The magnitude of the Burgers vector remains almost constant at different compositions of GeSe. We therefore exclude the possibility that the addition of GeSe changes the twist rates through altering the Burgers vector of the screw dislocation in the nanowire. The significant change in the twist rates can therefore be attributed to the change of the droplet sizes and its resultant change in diameters of the nanowires.

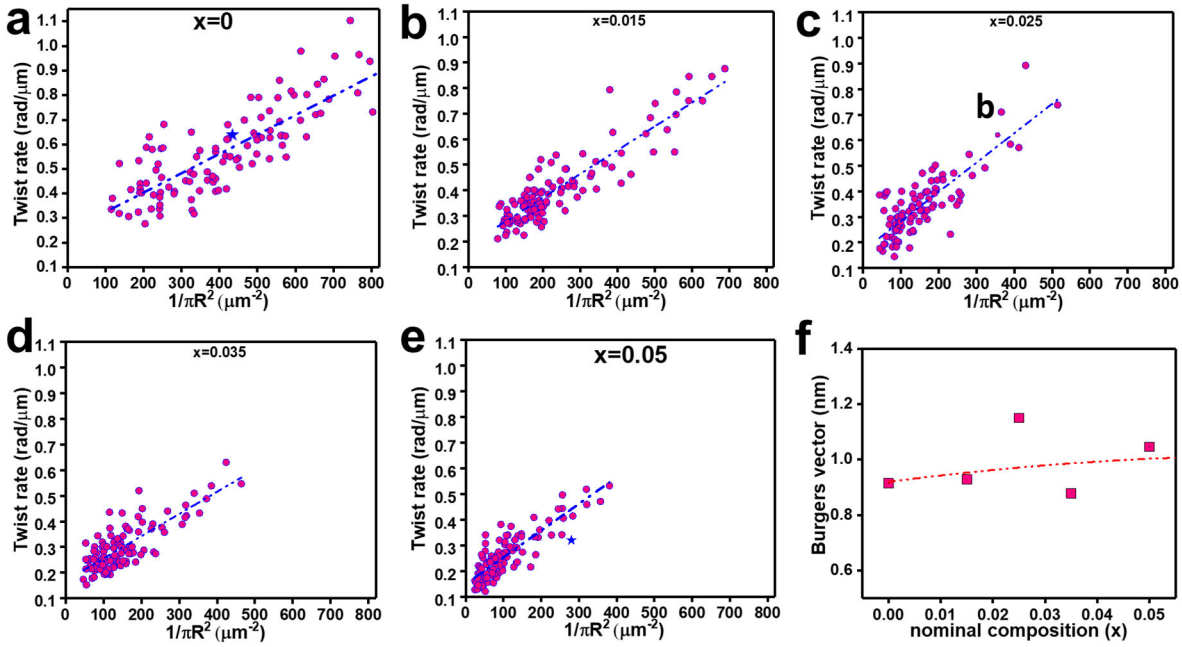

Figure 3.12 (a-e) Scatterplots of twist rates of mesoscale $GeS_{1-x}Se_x$ crystals synthesized at different nominal compositions in which x=0 (a), x=0.015 (b), x=0.025 (c), x=0.025 (d) and x=0.05 (e) against the inversed contact areas $(\pi R^2)^{-1}$ between catalyst nanoparticles and the tip . At each composition 100 individual structures were measured. The dash blue lines are linear fits through the data based on Eshelby's model. The blue stars represent the data obtained from TEM measurements of dislocated $GeS_{1-x}Se_x$ NW produced at same nominal composition (f) Scatterplot of Burgers vector obtained from those fittings versus nominal composition (0~0.05).

3.9 Compositional engineering of twisted $GeS_{1-x}Se_x$ crystals

In addition to tuning the twist rates, adding GeSe into the growth provides a means to tuning the composition of the nanowires and mesoscale twisted crystals. Through varying the composition of GeSe in the source materials, we synthesized twisted $GeS_{1-x}Se_x$ crystals with a range of compositions from x =0 to x = 0.11. The compositions were measured using SEM-EDS (Figure 3.13a). The compositional limit to form twisted $GeS_{1-x}Se_x$ crystals is x = 0.11, beyond which no twisted structures could form. This compositional limit was reached when the source materials with a composition of $GeS_{0.94}Se_{0.06}$ crystals was used for the growth. Beyond this limit, no twisted $GeS_{1-x}Se_x$ crystals was observed in the growth product; Those growth yielded alloyed flakes and leaves with no twist.

The composition engineering of twisted alloy structures enables tuning the optoelectronic properties, which is revealed by the Raman and photoluminescence (PL) measurement. Figure 3.13b shows the Raman spectra of mesoscale twisted $GeS_{1-x}Se_x$ crystals using a 785 nm laser as excitation source with different compositions. The Raman spectra of $GeS_{1-x}Se_x$ exhibit two-mode characteristics which simultaneously shows two set of Raman peaks that can be respectively assigned to GeS and GeSe. Six peaks at ~111 cm^{-1}, 238 cm^{-1}, 269 cm^{-1}, 95 cm^{-1}, 131 cm^{-1} and 212 cm^{-1} are Raman modes of GeS, whereas the two peaks at around 188 cm^{-1} correspond to $A_g^{(1)}$ and $A_g^{(2)}$ Raman modes of GeSe. This observed two-mode behavior can be understood by the modified random element isodisplacement (MREI) model [60,61], in which strong S-Se interactions in the $GeS_{1-x}Se_x$ crystals gives rise to two sets of eigenenergies for atomic vibration, one GeS-like and one GeSe-like in the alloy. Figure 3.13c presents PL spectra of the mesoscale helical GeS_xSe_{1-x} crystals with different compositions (x=0~0.11). GeS has a bandgap of 1.66 eV whereas GeSe have a narrower band gap of 1.16 eV. The PL peak due to the band-edge emission shifts from 1.66 eV to 1.59 eV with increasing concentration of GeSe from x =0 to x = 0.11. Figure 3.13d shows the change of band gaps with varying GeSe concentrations in twisted $GeS_{1-x}Se_x$ crystals, assuming that their bandgaps are very close to the energies of PL peaks. This variation of bandgaps in GeS_xSe_{1-x} follows Vegard's law[62] , $E_{g,GeS_{1-x}Se_x} = (1-x)E_{g,GeS} + Bx(1-x) + xE_{g,GeSe}$, where B is the bowing parameter. The fit of the results to Vegard's law leads to B=-1.43654eV. The results demonstrate good potential to use alloying to tune the optoelectronic properties and chiroptical response of twisted vdW crystals.

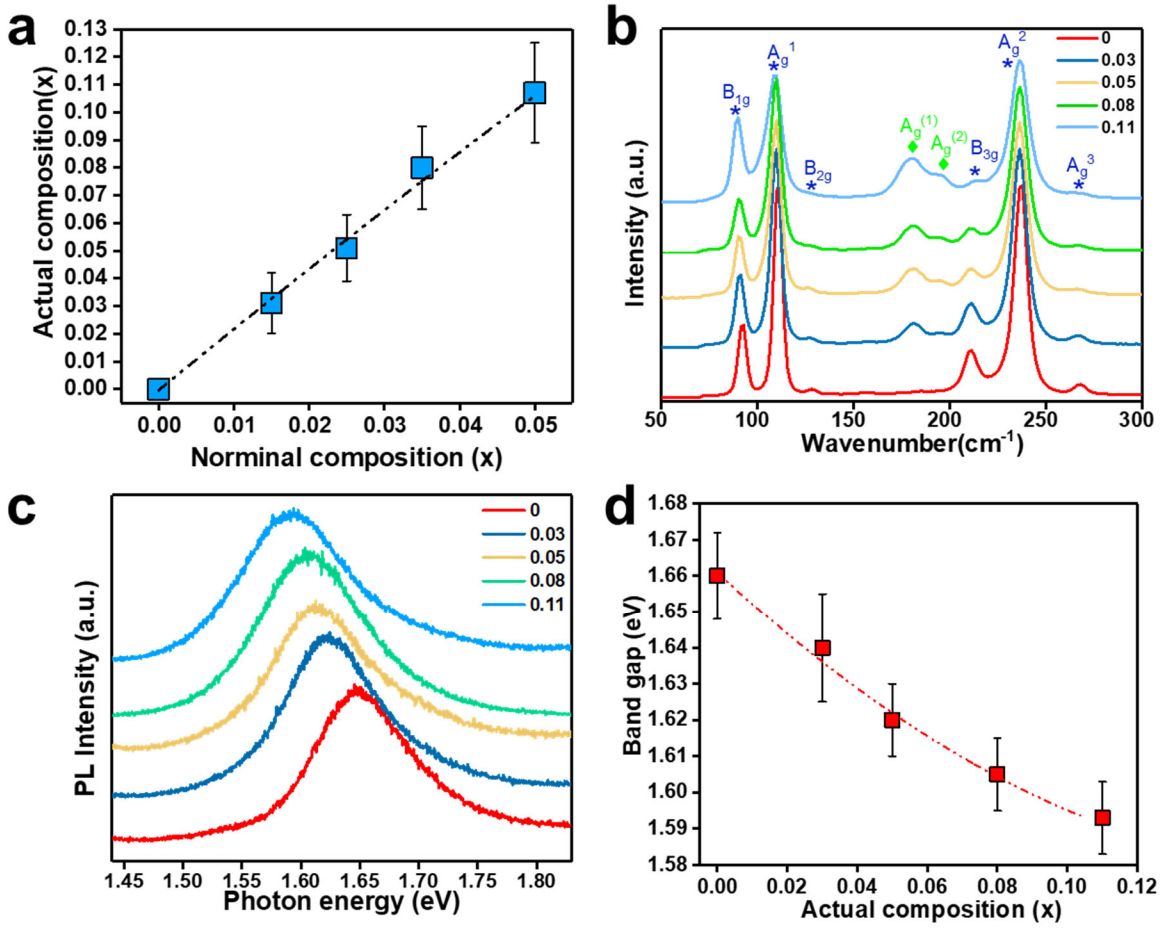

Figure 3.13 (a) Measured compositions of mesoscale twisted versus the compositions of the $GeS_{1-x}Se_x$ source (nominal compositions) for the growth. The dashed line is the linear fit of the data. (b) Raman spectra of mesoscale $GeS_{1-x}Se_x$ crystals under 785nm excitation with various compositions. (b) Photoluminescence (PL) spectra of mesoscale helical $GeS_{1-x}Se_x$ crystals (x=0~0.11) under 532nm excitation. (c) Band gaps of mesoscale $GeS_{1-x}Se_x$ as a function of composition x, and the error bars represent standard deviation.

Chapter 4 Strongly anisotropic surface phonon polaritons in layered GeS

4.1 Introduction to surface phonon polaritons

In polar crystals, a frequency band with negative permittivity extensively exists in the far-infrared and mid-infrared range. This band, also known as Reststrahlen band results from the oscillation of optical phonons, which is present between the frequency of transverse optical phonons (TO) and the frequency of longitudinal optical phonons (LO). In the Reststrahlen band, electromagnetic waves couple with ionic polarization of the crystal to form polariton modes which is supported at the interface between the polar crystal with negative permittivity and a material with positive permittivity.[63] These polaritons are confined electromagnetic surface waves in the far- and mid-infrared with their electric and magnetic field components exponentially decaying from the interface, which are so called surface phonon polaritons (SPhPs). Surface phonon polaritons in the far-infrared to mid-infrared range are analogous to the surface plasmon polaritons (SPPs) in the visible and near-infrared range propagating at the interface of a dielectric with positive permittivity and metal with negative permittivity.[64] The loss associated with SPhPs propagation can be much smaller in contrast to the loss of SPP propagation the propagation of SPhPs eliminates the Ohmic loss due to electrons present in the SPPs . These features render SPhPs attractive for applications including terahertz photonics, molecular sensing, second harmonic generation (SHG), coherent mid-infrared emission, heat conduction and radiative heat transfer[63,65-70]. Although great progress has been made in understanding and maneuvering the SPhPs, prior studies were primarily focused on isotropic polar crystals such as silicon carbide, silica and III-V semiconductors on which the SPhPs propagate in a uniform way.[66,67,69,71] In contrast to these isotropic SPhPs, anisotropic SPhPs can propagate in crystals with anisotropic structures. Unique benefits can be derived from the directional propagation of the SPhPs including strongly anisotropic optical and thermal properties. SPhPs nevertheless have been rarely explored in anisotropic uniaxial and biaxial crystals.

4.2 Hyperbolic phonon polaritons in anisotropic crystals

In uniaxial and biaxial crystals, permittivity is described by a second-rank tensor in which the components of permittivity for different principal directions can be significantly distinct. In an uniaxial material, the permittivity tensor is given by

$$\overline{\overline{\varepsilon}} = \begin{pmatrix} \varepsilon_{\perp} & 0 & 0 \\ 0 & \varepsilon_{\perp} & 0 \\ 0 & 0 & \varepsilon_{\parallel} \end{pmatrix}$$

where $\varepsilon_{\perp}$ is the principal component of the permittivity tensor perpendicular to the optical axis and is $\varepsilon_{\parallel}$ is the component of the permittivity tensor in directions along the optical axis. The isofrequency surface for the extraordinary electromagnetic waves in an uniaxial material is given by,

$$\frac{k_{\parallel}^{2}}{\varepsilon_{\perp}} + \frac{k_{\perp}^{2}}{\varepsilon_{\parallel}} = k_{0}^{2}$$

Where $k_{\parallel}$ is the wave vector component parallel to the optical axis, $k_{\perp}$ is the wave vector component parallel to the optical axis. At certain frequencies, the material can have an extremely large optical birefringence where one principal component of permittivity has opposite sign with others ($\varepsilon_{\perp} \cdot \varepsilon_{\parallel} < 0$). Under such circumstance, the isofrequency surface becomes a hyperboloid, giving rise to extremely anisotropic propagation of the phonon polaritons within the crystal. Phonon polaritons with such hyperbolic isofrequency surfaces are called Hyperbolic photon polaritons (PhPs). In addition to being highly directional, hyperbolic PhPs can confine mid-infrared and far-infrared light at the nanoscale beyond the diffraction limit, and also generate high photon density of states(PDOS).[72] These advantages boost a variety of useful applications including enhancing the spontaneous emission, negative refraction, superlensing and non-linear optics.[73-75]

Hyperbolic PhPs have been first explored in layered vdW materials, which possess strong structural anisotropy between the in-plane directions (parallel to the layers) and out-plane direction (along the norm of the layers). Highly confined hyperbolic PhPs with low loss have been uncovered in hexagonal boron nitride (hBN)[73], an uniaxial vdW 2D material. hBN exhibits an extremely large crystalline anisotropy between the in-plane directions and the out-plane direction, resulting in a large optical birefringence. This gives rise to two distinct spectral windows where the components of dielectric permittivity along different principle crystal axes (the out of plane direction and the in-plane direction) have different signs. The two frequency windows are referred to as the lower band ($\sim$760-820 cm^{-1}) and upper band(UR, $\sim$1365-1610 cm^{-1}), where the hyperbolic PhPs are supported. The hyperbolic PhPs are tunable, with their dispersion strongly dependent on the thickness of the hBN. The hyperbolic PhPs in hBN have enabled a number of intriguing optical applications in the mid-infrared range including optical resonators with high quality factors, imaging and nanofocusing with subwavelength resolution beyond diffraction limit.[76-78] Hyperbolic SPhPs in hBN also provide good potential to achieve thermal management in electronics using vdW materials and heterostructures.[79] A recent study shows that encapsulation of graphene device with hBN enables efficient out-of-plane energy transfer through the coupling of hyperbolic SPhPs to the hot charge carriers in graphene.[79]

4.3 Hyperbolic surface phonon polaritons

Despite those great opportunities for nanophotonics and thermal engineering provided by hyperbolic phonon polaritons, the hyperbolic PhPs such as PhPs in hBN are confined within the volume of the material which are bulk electromagnetic modes rather than surface polaritons.[73,78] In contrast, hyperbolic isofrequency surfaces could be realized for surface phonon polaritons, yielding hyperbolic SPhPs confined at the surface of the material. The planar hyperbolic SPhPs can provide unique advantages in contrast to either the isotropic SPhPs or the volume-confined hyperbolic PhPs. For example, the surface and planar nature of the hyperbolic surface phonons are desirable for in-chip integrated photonics.[80] The in-plane propagation is highly directional and is well-suited to be used for planar imaging with resolution beyond the diffraction limit. The hyperbolic propagation of SPhPs results in enhanced electric fields and large photon density of states (PDOS) at the surface, which is advantageous to enhance the spontaneous emission from an external emitter from an emitter and enhance near-field radiative heat transfer.[80] In contrast, these applications cannot be easily enabled by the volume confined PhPs since the high PDOS associated with those PhPs largely exists inside the material, limiting their coupling with external emitter and materials. Despite these advantages, hyperbolic SPhPs have been rarely studied compared to isotropic SPhPs and hyperbolic PhPs. [81]

4.4 Overview

This work theoretically investigates the SPhPs in thin films of GeS, a layered compound which possess strong optical anisotropy between in-plane armchair direction and the zigzag direction. Using semi-analytical analysis and numerical full-wave simulations, we demonstrate GeS films at thickness of a few hundred nanometers support strongly anisotropic SPhPs in the far-infrared range. Two kinds of surface confined phonon polaritons namely hyperbolic SPhPs and elliptic SPhPs, are respectively identified in the frequency ranges of ~210-250 cm^{-1} and ~260-290 cm^{-1}. The hyperbolic SPhPs propagate along directions with limited angles with respect to the zigzag direction. Over the angular range, there is no propagation of SPhPs. The elliptic SPhPs are also strongly anisotropic, channeling as a narrow beam along the armchair direction. These SPhPs show strongly dependence on the film thickness. As the thickness of the film decreases, dispersion of the SPhPs markedly changes and the SPhPs become more confined.

4.5 Far-infrared optical property of GeS

Hyperbolic in-plane propagation of the SPhPs in a material can be supported under the condition that the two in-plane components of permittivity tensor are opposite in sign. This is possible in materials with strong in-plane anisotropy of the structures. Germanium monosulfide, a layered material with strong in-plane anisotropy between the armchair direction (a-axis) and the zigzag direction (b-axis) could be desirable material for anisotropic SPhPs (Figure 4.1a). Far-infrared optical property of GeS is governed by the oscillation of the optical phonons. The structural anisotropy in GeS results in distinct frequencies of optical phonons along different crystal axes, giving rise to strong optical anisotropy in the far-infrared range. Previous studies have extracted the optical permittivity of GeS in the far-infrared range through Kramers-Kronig (KK) analysis of the measured reflection spectra. [82,83] Principal components of the permittivity along different crystal directions are given by,

$$\varepsilon_j(\omega) = \varepsilon_\infty + \sum_k \frac{\omega_{TO,k}^2 S_k}{\omega_{TO,k}^2 - \omega^2 - i\omega\omega_{TO,k}\gamma_k}$$

Where ε_j is the principal component of the permittivity along j axis, $\omega_{TO,k}$, S_k, and γ_k are the frequency of transverse optical phonons, the oscillation strength, and the damping ratio associated with k th oscillation, respectively. Using those parameters from the previous study[83], the imaginary parts and the real parts of complex components of the permittivity along a-axis, b-axis and c-axis are plotted as a function of frequency (in wavenumbers), which are shown in Figure 4.1b. We note there are two frequency bands, one band (~210-250 cm^{-1}) and the other band (~260-290 cm^{-1}) in which the real parts of the permittivity component for the in-plane a-axis and b-axis have opposite signs. These bands are expected to support anisotropic SPhPs.

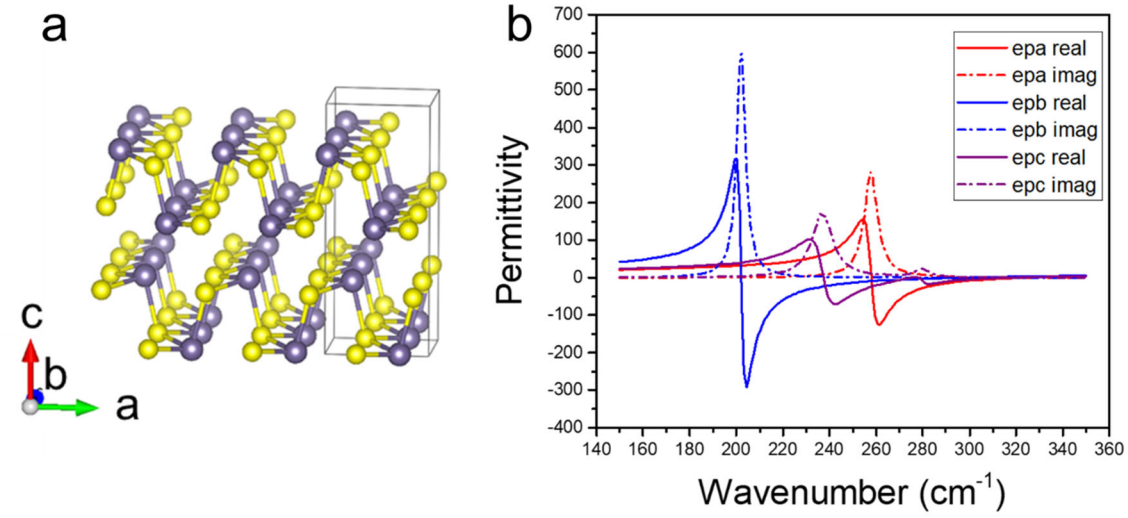

Figure 4.1 (a) Crystal structure of GeS. The unit cell is shown with a framed box. a-axis, b-axis and c-axis are the armchair direction, the zigzag direction and vdW stacking direction, respectively. (b) Permittivity of GeS versus frequency in the far-infrared range.

4.6 Transfer matrix method for calculating dispersion of surface polaritons

The transfer-matrix method is a semi-analytical method widely used in optics to analyze the propagation of electromagnetic waves through a stack of layers with distinct optical and magnetic properties. This method has been used as a powerful tool for calculating the dispersion relation of surface and volumetric polariton modes including surface plasmon polaritons, hyperbolic PhPs and SPhPs. In these calculations, evanescent plane waves with different lateral wavevectors are typically used to excite polaritons in the materials and the dispersion relation of the polaritons can be revealed by the calculated reflection coefficients associated with reflected wave. This method is used to calculate the dispersion of SPhPs in GeS films propagating in varying directions.

Here, we provide our transfer matrix analysis in full detail. The propagation of electromagnetic plane waves in a material is governed by Maxwell's equations. we use the expression $e^{i(\vec{k}\cdot\vec{r}-\omega t)}$ for the plane wave. In cases where there is no free charge or free current, we have

$$\nabla \times \vec{E} = i\omega \overline{\overline{\mu}} \cdot \vec{H}$$
$$\nabla \times \vec{H} = -i\omega \overline{\overline{\varepsilon}} \cdot \vec{E}$$

where $\bar{\bar{\mu}}$ is the permeability tensor and $\bar{\bar{\varepsilon}}$ is the permittivity tensor.

Since GeS is not magnetic,

$$\overline{\overline{\mu}} = \begin{pmatrix} \mu_0 & 0 & 0 \\ 0 & \mu_0 & 0 \\ 0 & 0 & \mu_0 \end{pmatrix}$$

In our calculation, we are interested in polaritons propagating within the plane defined by a-axis and b-axis. The surface normal of the GeS film is always aligned with the c-axis of the crystal (vdW stacking direction). This gives,

$$\overline{\overline{\varepsilon}} = \begin{pmatrix} \varepsilon_{xx} & \varepsilon_{xy} & 0 \\ \varepsilon_{yx} & \varepsilon_{yy} & 0 \\ 0 & 0 & \varepsilon_{zz} \end{pmatrix}$$

Plug these tensors into the Maxwell equations, we have

$$\frac{\partial E_z}{\partial y} - \frac{\partial E_y}{\partial z} = i\omega\mu_0 H_x$$
$$\frac{\partial E_x}{\partial z} - \frac{\partial E_z}{\partial x} = i\omega\mu_0 H_y$$
$$\frac{\partial E_y}{\partial x} - \frac{\partial E_x}{\partial y} = i\omega\mu_0 H_z$$
$$\frac{\partial H_z}{\partial y} - \frac{\partial H_y}{\partial z} = -i\omega\varepsilon_{xx}\varepsilon_0 E_x - i\omega\varepsilon_{xy}\varepsilon_0 E_y$$
$$\frac{\partial H_x}{\partial z} - \frac{\partial H_z}{\partial x} = -i\omega\varepsilon_{yy}\varepsilon_0 E_y - i\omega\varepsilon_{yx}\varepsilon_0 E_y$$
$$\frac{\partial H_y}{\partial x} - \frac{\partial H_x}{\partial y} = -i\omega\varepsilon_{zz}\varepsilon_0 E_z$$

The incident plane wave propagates along z-axis. Since the structure is homogeneous in the lateral x-y plane, $\frac{\partial}{\partial x} = ik_x, \frac{\partial}{\partial y} = ik_y$ where k_x and k_y are the component of wavevector of the incidence wave along the x and y direction. This simplifies the equations and after some algebra, we get

$$\frac{d}{dz}\begin{pmatrix} E_x \\ E_y \\ H_x \\ H_y \end{pmatrix} = \begin{pmatrix} 0 & 0 & i\frac{k_x k_y}{\omega\varepsilon_0\varepsilon_{zz}} & i(-\frac{k_x^2}{\omega\varepsilon_0\varepsilon_{zz}} + \omega\mu_0) \\ 0 & 0 & i(\frac{k_y^2}{\omega\varepsilon_0\varepsilon_{zz}} - \omega\mu_0) & -i\frac{k_x k_y}{\omega\varepsilon_0\varepsilon_{zz}} \\ -i(\frac{k_x k_y}{\omega\mu_0} + \omega\varepsilon_{yx}) & i(\frac{k_x^2}{\omega\mu_0} - \omega\varepsilon_0\varepsilon_{yy}) & 0 & 0 \\ i(-\frac{k_y^2}{\omega\mu_0} + \omega\varepsilon_0\varepsilon_{xx}) & i(\frac{k_x k_y}{\omega\mu_0} + \omega\varepsilon_0\varepsilon_{xy}) & 0 & 0 \end{pmatrix}\begin{pmatrix} E_x \\ E_y \\ H_x \\ H_y \end{pmatrix}$$

We denote the vector formed by E_x E_y H_x and H_y as $\vec{V}$, and the 4 by 4 matrix as $\overline{\overline{H}}$. Solving $\vec{V}$ solves the magnetic fields and electrical fields since E_z and H_z can be solved from E_x E_y H_x and H_y and all components of the electric and magnetic fields are known.

$$i\omega\mu_0 H_z = ik_x E_y - ik_y E_x$$
$$-i\omega\varepsilon_{zz}\varepsilon_0 E_z = ik_x H_y - ik_y H_x$$

The electrical fields within the film can be solved by solving $\frac{d}{dz}\vec{V} = \overline{\overline{H}}\,\vec{V}$ .The solution can be expanded with four eigenmodes. The four eigenmodes corresponds to incident and reflective waves with different polarizations , that is an incident TE wave, an incident TM wave, a reflected TE wave and a reflected TM wave respectively. The expansion is given by,

$$\vec{V}(z) = A_1\vec{a}_1 e^{i\beta_1 z} + A_2\vec{a}_2 e^{i\beta_2 z} + A_3\vec{a}_3 e^{-i\beta_3 z} + A_4\vec{a}_4 e^{-i\beta_4 z} = \begin{pmatrix}\vec{a}_1 & \vec{a}_2 & \vec{a}_3 & \vec{a}_4\end{pmatrix}\cdot\begin{pmatrix} e^{i\beta_1 z} & 0 & 0 & 0 \\ 0 & e^{i\beta_2 z} & 0 & 0 \\ 0 & 0 & e^{-i\beta_3 z} & 0 \\ 0 & 0 & 0 & e^{-i\beta_4 z}\end{pmatrix}\cdot\begin{pmatrix} A_1 \\ A_2 \\ A_3 \\ A_4\end{pmatrix}$$

A_i and β_i are the amplitude and wavevector of the i th eigenmode, $\vec{a}_i$ is the i th eigenvector of $\overline{\overline{H}}$.

This formalism allows us to connect the field at any propagation length with in a film to the field at a known propagation length.

$$\overline{V}(z) = \overline{\overline{P}}(z, z')\cdot\overline{V}(z')$$

where

$$P(z,z') = \begin{pmatrix}\overline{a_1} & \overline{a_2} & \overline{a_3} & \overline{a_4}\end{pmatrix}\cdot\begin{pmatrix} e^{i\beta_1(z-z')} & 0 & 0 & 0 \\ 0 & e^{i\beta_2(z-z')} & 0 & 0 \\ 0 & 0 & e^{-i\beta_3(z-z')} & 0 \\ 0 & 0 & 0 & e^{-i\beta_4(z-z')}\end{pmatrix}\cdot\begin{pmatrix}\overline{a_1} & \overline{a_2} & \overline{a_3} & \overline{a_4}\end{pmatrix}^{-1}$$

which is the transfer matrix.

In this position, the transfer matrix analysis is readily to be applied to study the GeS film. In the calculation, we calculate the reflection coefficients of a GeS film at thickness of d, sitting on a substrate with isotropic optical permittivity such as air or fused silica. Electromagnetic wave is incident from the air. There are 4 eigenmodes in air (medium 1), incident TM wave, a reflected TE wave and a reflected TM wave. The interface between air and the GeS film is located at z=0. The electric and magnetic fields in GeS (medium 2) also consists of 4 eigenmodes. While in the substrate (medium 3), there are only 2 eigenmodes, both are transmitted waves. Appling the boundary conditions for electromagnetic fields, we have

$$\begin{pmatrix} A_1^{(3)} \\ A_2^{(3)} \\ 0 \\ 0 \end{pmatrix} = \begin{pmatrix} \overline{a}_1^{(3)} & \overline{a}_2^{(3)} & \overline{a}_3^{(3)} & \overline{a}_4^{(3)} \end{pmatrix}^{-1} \cdot \overline{\overline{P}}(d,0) \cdot \begin{pmatrix} \overline{a}_1^{(1)} & \overline{a}_2^{(1)} & \overline{a}_3^{(1)} & \overline{a}_4^{(1)} \end{pmatrix} \cdot \begin{pmatrix} A_1^{(1)} \\ A_2^{(1)} \\ A_3^{(1)} \\ A_4^{(1)} \end{pmatrix}$$

which connects the amplitudes of reflected waves($A_3^{(1)}$ and $A_4^{(1)}$) and transmitted waves($A_1^{(3)}$ and $A_2^{(3)}$) to the amplitudes of incident waves($A_1^{(1)}$ and $A_2^{(1)}$). Given the amplitudes of incident waves ($A_1^{(1)}$ and $A_2^{(1)}$), reflection and transmission coefficients can be calculated.

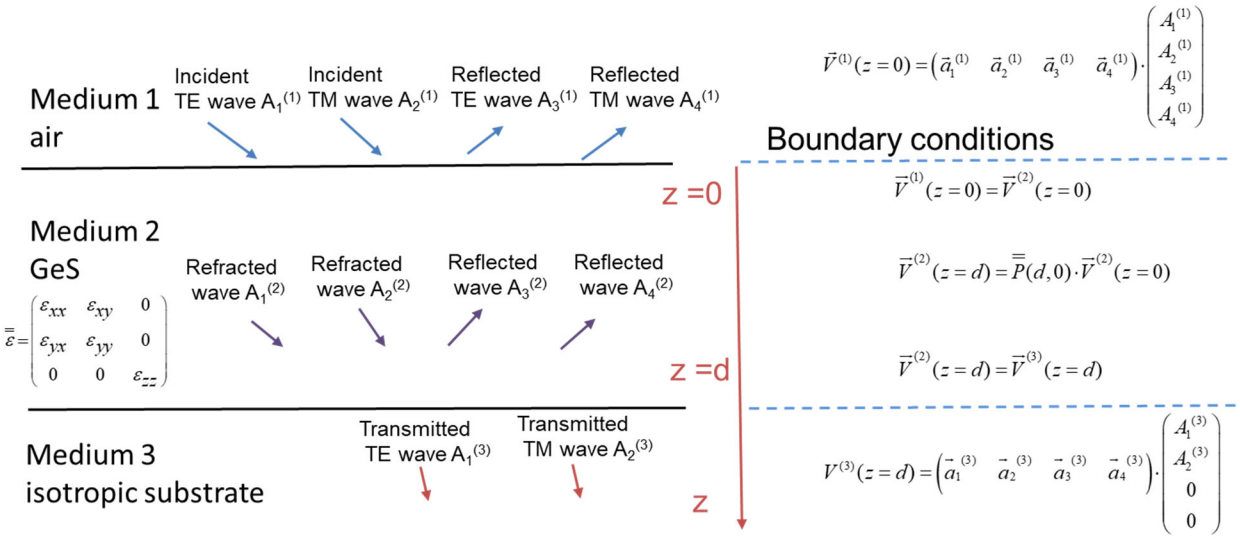

Figure 4.2 Diagram showing how transfer matrix method was applied to GeS film on an substrate with isotropic permittivity

In the calculation, transfer matrix method may not be numerically stable. Instead, we used modified formalism of transfer matrix method, which is called scattering matrix method. In the scattering matrix method, the amplitudes of the incident, reflected and transmitted mode are resorted in the matrix formalism,

$$\begin{pmatrix} A_3^{(1)} \\ A_4^{(1)} \\ A_1^{(3)} \\ A_2^{(3)} \end{pmatrix} = \begin{pmatrix} \overline{\overline{S}}_{11} & \overline{\overline{S}}_{12} \\ \overline{\overline{S}}_{21} & \overline{\overline{S}}_{22} \end{pmatrix} \cdot \begin{pmatrix} A_1^{(1)} \\ A_2^{(1)} \\ 0 \\ 0 \end{pmatrix}$$

where the S matrix is the scattering matrix. Scattering matrix method has stronger numerical stability in contrast to the transfer matrix method. Following Rumpf's algebra[84], we calculated the scattering matrix to obtain the dispersion relation of the GeS films.

To reveal the anisotropic SPhPs in GeS, we calculated the dispersion relation of SPhPs along different directions within the ab plane of the crystal. The incident plane (the plane containing the incident wave and surface normal) of far-infrared electromagnetic waves is fixed, which is defined by x-axis and z-axis. z-axis is along the surface normal of the GeS film which is aligned with the c-axis (vdW stacking direction) of GeS crystal. To calculate dispersion of polariton along an arbitrary in-plane direction, say a direction at angle φ with respect to a-axis, GeS crystal is rotated about the c axis such that the angle between the xz plane and a-axis is φ. The rotation of the crystal leads to a change of the permittivity tensor, $\bar{\bar{\varepsilon}}_{xyz} = R^T \bar{\bar{\varepsilon}}_{abc} \mathrm{R}$ where R is the rotation matrix associated with φ . This is schematically shown in Figure 4.3.

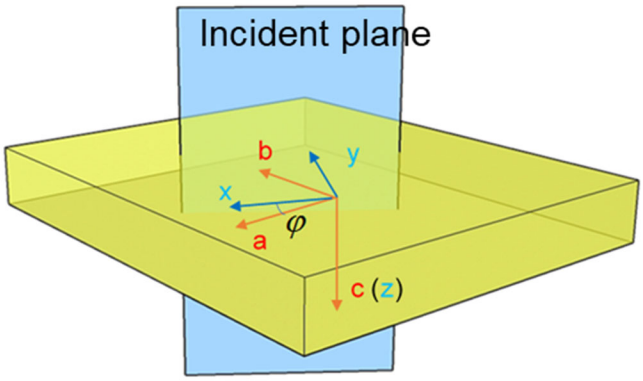

Figure 4.3 Diagram showing how to calculate the dispersion of polaritons along arbitrary direction.

4.7 Dispersion relation of anisotropic SPhPs in GeS

Using scattering matrix calculation, we calculated the reflection coefficients of the GeS film. The phonon polariton modes are revealed by the imaginary part of the complex reflection coefficients, r = r(k,ω). Figure 4.4 shows the dispersion relations for phonon polaritons in free-standing GeS film with a thickness of 20 nm. Polaritons modes exist in two frequency bands, the low band (~210-250 cm^{-1}) and a upper band (~260-290 cm^{-1}). These two bands correspond to the frequency range where the real part of the permittivity component for the in-plane a-axis and b-axis have opposite signs, suggesting these phonon polaritons are strong anisotropic with the ab plane. The dispersion relation of the polaritons propagating within ab plane shows strong dependence on the propagation direction, which significantly changes with varying φ (Figure 4.4). Note that φ is the angle between the propagation direction and a-axis of the crystal. Phonon polaritons in the lower band propagate along b-axis (at φ=90°) but not along a-axis (at φ=0°); whereas phonon polaritons in the upper band propagate along a-axis but not along b-axis. To clearly reveal the anisotropic propagation of the phonon polaritons, we plot the dispersion relations of phonon polaritons in the lower band as a function of φ. In this band, phonon polaritons can only propagate within a range of φ with wavevectors depending on the propagation direction. For instance, at the frequency of 222 cm^{-1}, phonon polaritons can propagates in directions that are at

angles between 50° and 90° with respect to a-axis. Considering the two-fold symmetry of the crystal structure, propagation of the phonon polaritons is supported within φ=50° to φ=130° .

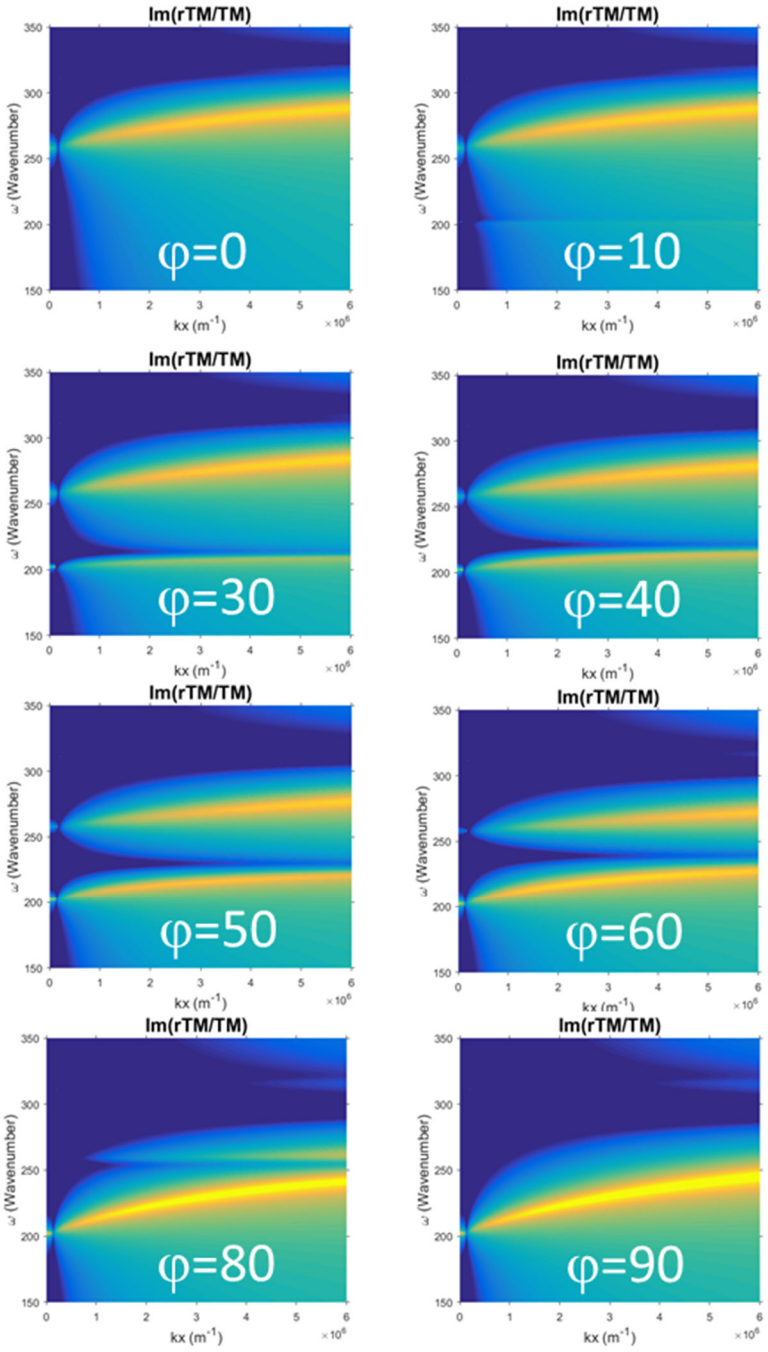

Figure 4.4 Dispersions for SPhSs in a 20 nm thick GeS film for different propagation directions. φ is angle between the propagation direction and a-axis. At φ = 0°, the propagation direction is aligned with a-axis; At φ = 90°, the propagation direction is aligned with b-axis.

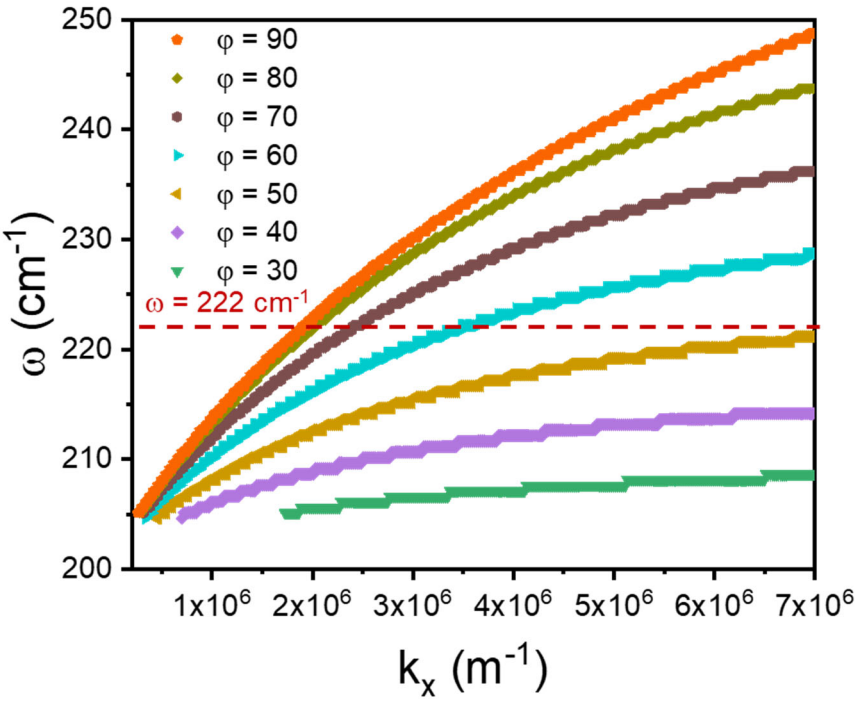

Figure 4.5 Angular-dependent dispersion relation of phonon polaritons in the 20nm-thick GeS film. Red dashed line marks the frequency of 222 cm^{-1}. At this frequency, phonon polaritons can only propagate in directions with φ between 50° and 90°.

Through calculating the angular-dependent dispersion relations, we could construct the isofrequency surfaces of the phonon polaritons at different frequencies in the lower band and in the upper band, showing the dependence of the wavevector on the propagation direction. Figure 4.6 shows the isofrequency surfaces at different frequencies in the lower band. These isofrequency surfaces are hyperbolic. The result suggests the in-plane propagation of hyperbolic phonon polaritons in the 20 nm thick GeS film. The shape of the hyperboloid varies with varying frequency, resulting from changes of in-plane permittivity components with the frequency. Figure 4.7 shows the isofrequency surfaces at different frequencies in the upper band. In contrast to the isofrequency surfaces for frequencies in the lower band, the isofrequency surfaces for frequencies in the upper band are relatively "flat" and elliptic. This result can be understood by considering in-plane principal components of the permittivity. In the upper band, the ratio of magnitude of in-plane components of the permittivity tensor ($|\mathrm{Re}(\varepsilon_b)|/|\mathrm{Re}(\varepsilon_a)|$) is very small, resulting in the flat and elliptic topology of the isofrequency surfaces. Since the energy flow of the polaritons that is determined by their group velocities $V_g = \nabla_k \omega(k)$ is perpendicular to the isofrequency surfaces, the flat isofrequency surfaces lead to formation of a narrow beam channeling along the direction normal to the flat surface. These anisotropic phonon polaritons are analogous to directional surface plasmonic polaritons that have been previously identified in black phosphorus. [85,86] These SPP modes exist at frequencies where in-plane components of the permittivity tensor have very

different magnitudes. These highly directional modes are therefore termed as anisotropic elliptical modes.[85]

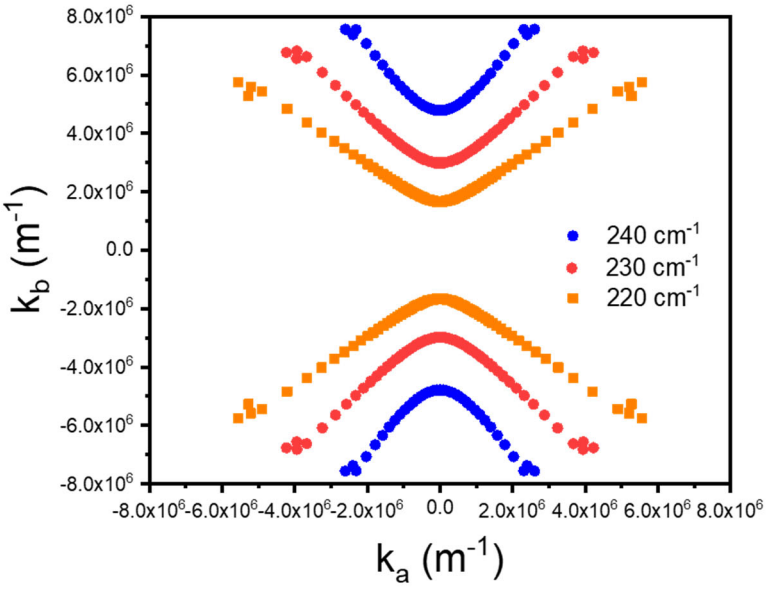

Figure 4.6 Isofrequency surfaces at different frequencies in the lower band.

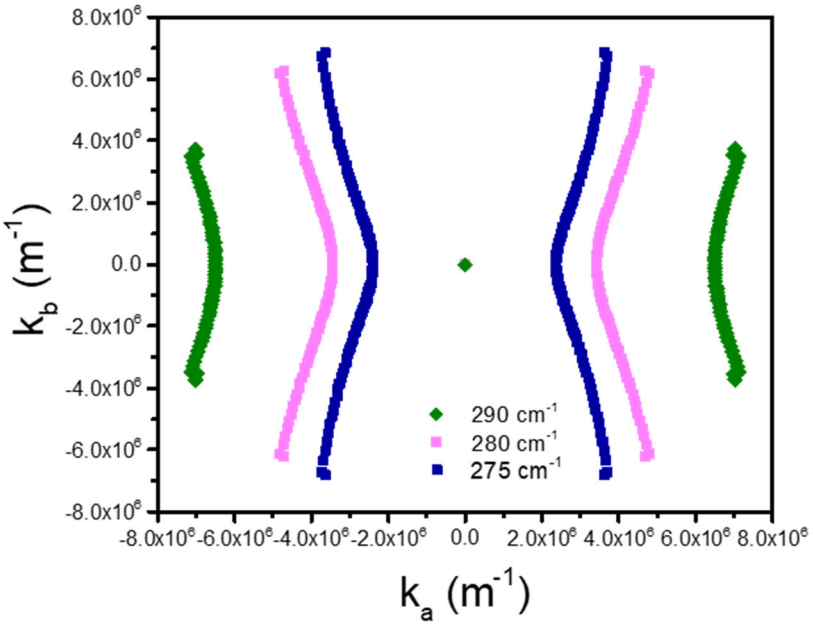

Figure 4.7 Isofrequency surfaces at different frequencies in the upper band.

4.8 FDTD (finite-difference time-domain) simulation

Our study using transfer matrix method has revealed that highly anisotropic propagation of phonon polaritons are supported in GeS thin flims. The method has yielded dispersion relation and isofrequency surfaces for the polaritons, which are essential for understanding the propagation of the polaritons. This method, nevertheless, fails to provide further information on whether the polaritons are surface-confined or volume-confined. To address this question, we performed three-dimensional FDTD simulations to visualize the mode profiles of the phonon polaritons. This numerical study was performed using a commercial software CST microwave studio. In the FDTD simulation, a dipole is used as near-field source to excite the polaritons in the GeS film. Figure 4.8 and Figure 4.9 show the mode distribution of the phonon polaritons in a 20 nm thick film at frequencies in the lower band and upper band respectively. The modes are visualized by the z-component of the electric field (E_z) associated with phonon polaritons, which are in good agreement with the isofrequency surfaces obtained from transfer matrix calculation (Figure 4.6 and Figure 4.7). These anisotropic modes in both lower band and in the upper band are further identified to be the surface mode, which is suggested by the electrical field distribution in the cross section containing the propagation direction and the z-axis. In the E_z distribution , the magnitude of Ez shows maximum at the surface of the film and drops with distance from the surface, suggesting the these modes are confined at the surface. To illustrate this, we show the Ez distribution in the bc-plane at 220 cm^{-1} in the bc plane and the Ez distribution in the ac plane at 280 cm^{-1} in Figure 4.10 , both of which show maximum Ez at the surface of the film. The three-dimensional FDTD simulations demonstrate that those anisotropic phonon polaritons revealed by transfer matrix calculation are anisotropic surface phonon polaritons.

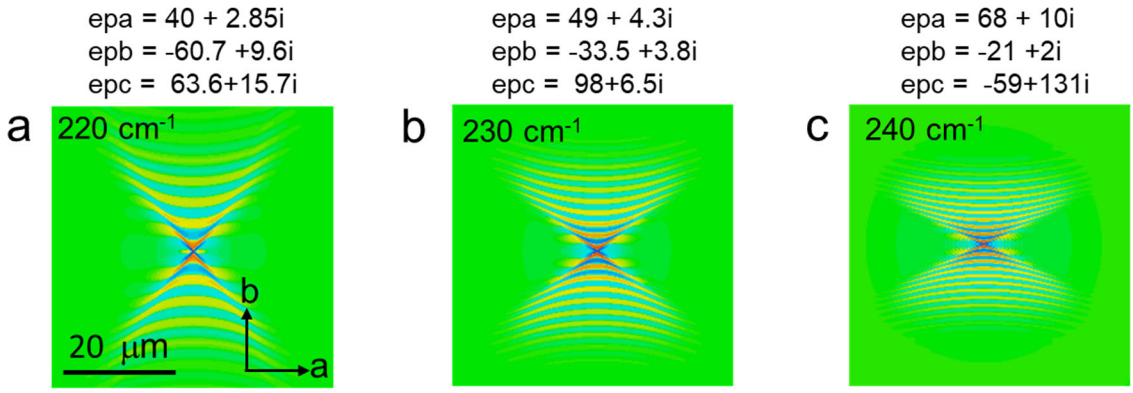

Figure 4.8 Color maps showing the distribution of E_z associated with phonon polaritons at frequencies of 220 cm^{-1} (a), 230 cm^{-1} (b), and 240 cm^{-1} (c), respectively. The modes are excited by a dipole located 50 nm above the surface of the GeS film. The principal components of the permittivity at corresponding frequencies are shown above the maps.

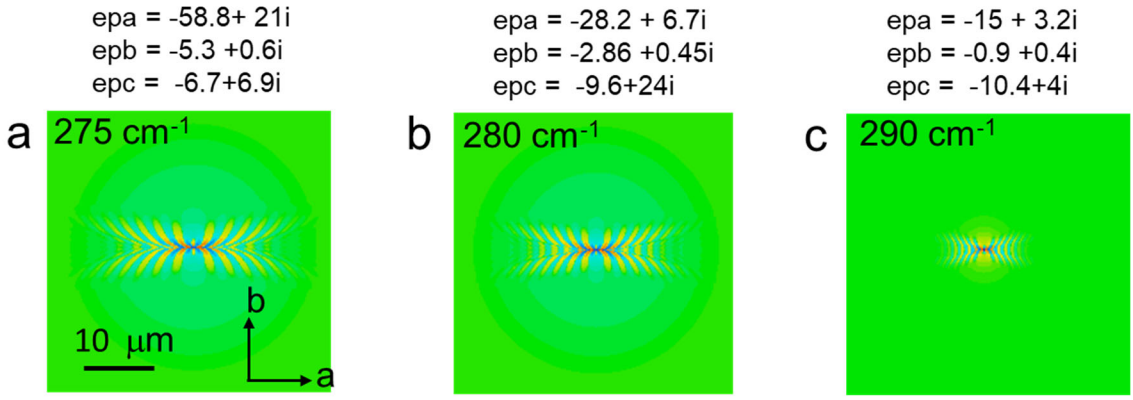

Figure 4.9 Color maps showing the distribution of E_z associated with phonon polaritons at frequencies of 275 cm^{-1} (a), 280 cm^{-1} (b), and 290 cm^{-1} (c), respectively. The modes are excited by a dipole located 50 nm above the surface of the GeS film. The principal components of the permittivity at corresponding frequencies are shown above the maps.

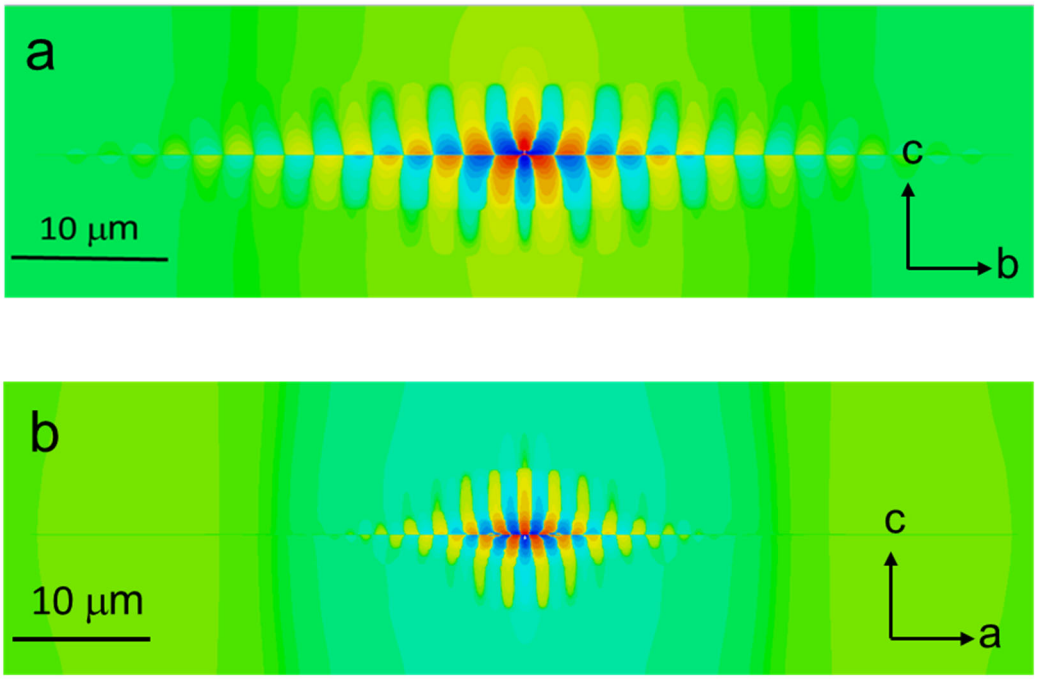

Figure 4.10 Color maps showing the distribution of z-component of the electric field associated with phonon polaritons in the bc plane at 220 cm^{-1} (a) and in the ac plane at 280 cm^{-1} (b), respectively. The modes are excited by a dipole located 50 nm above the surface of the GeS film.

4.9 Dependence of the SPhPs on the thickness of the film

The anisotropic SPhPs in GeS shows a strong dependence on the thickness of the films. Figure 4.11 shows the varying topology of the isofrequency surfaces with varying thickness of the film. As the film thickness increases, the wavevector of the polaritons becomes larger, resulting in worse confinement. This effect is also confirmed by the FDTD simulation (Figure 4.22). These

results suggest that the phonon polaritons of the desired wavelength and confinement can be engineered by varying thickness of the GeS film, which could be easily achieved through the mechanical exfoliation.

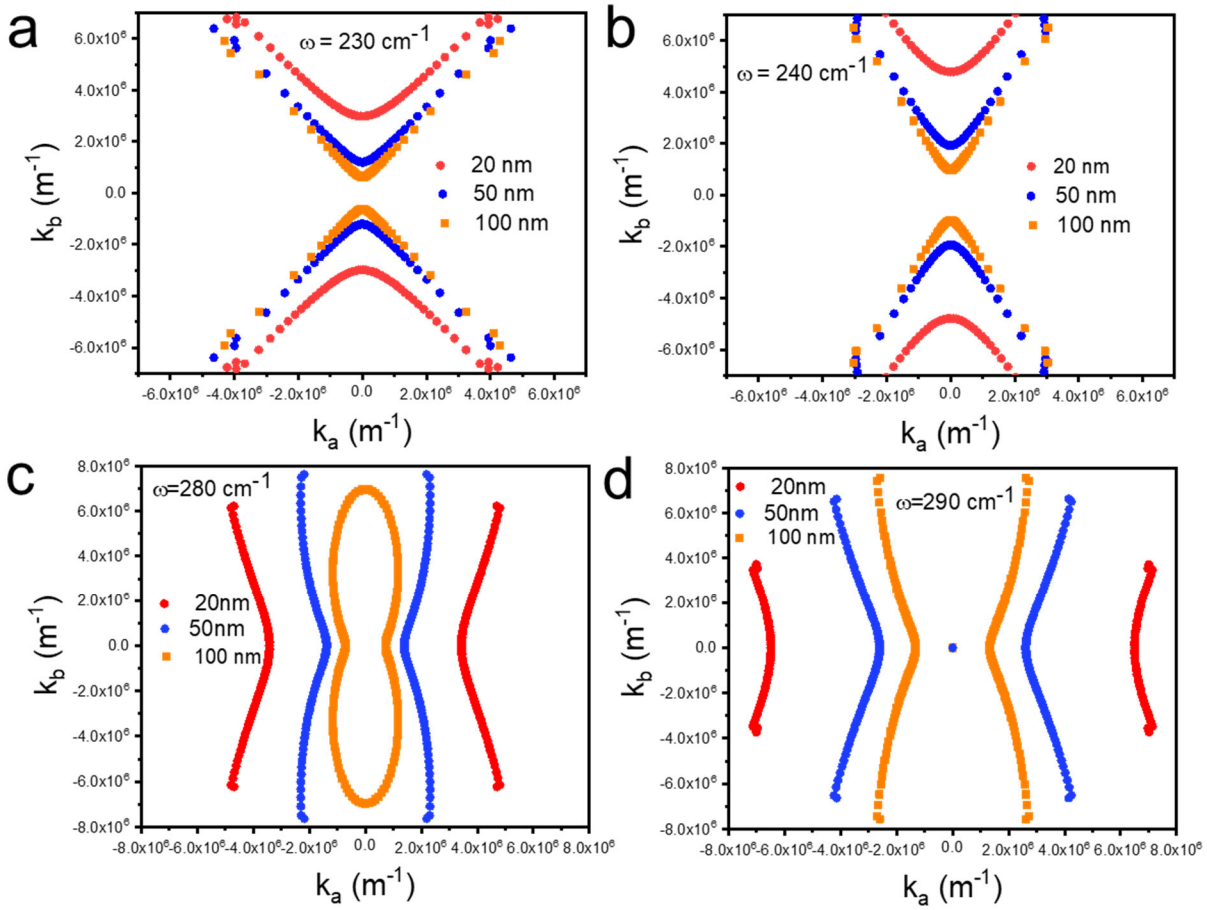

Figure 4.11 Isofrequency surfaces for GeS films with different thicknesses of 20 nm, 50 nm and 100 nm at 230 cm^{-1}, 240 cm^{-1}, 280 cm^{-1} and 290 cm^{-1}.

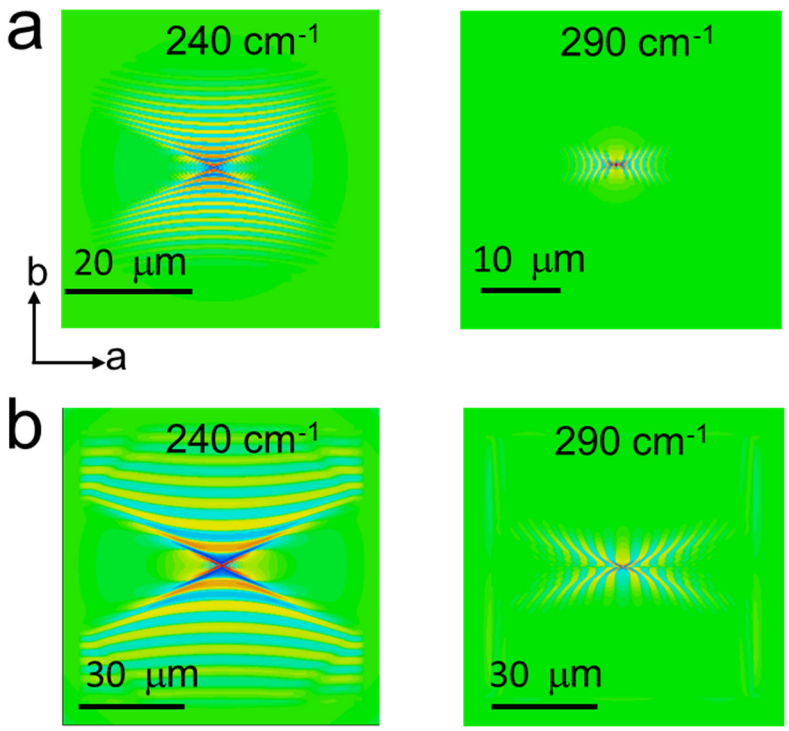

Figure 4.12 Color maps showing the distribution of E_z associated with surface phonon polaritons at frequencies of 240 cm^{-1} and 290 cm^{-1} for GeS films with thickness of 20 nm (a) and 100 nm (b). respectively.

Chapter 5 Conclusion and outlook

5.1 Conclusion

This dissertation is focused on the study of germanium monosulfide (GeS), a layered two-dimensional semiconductor in the family of IV-VI monochalcogenides.

First, we show that GeS is a prototypical 2D material which can be grown into twisted form through the mechanism of the Eshelby twist associated with a screw dislocation. We demonstrate that screw dislocations can drive the formation of twisted GeS on scales ranging from the nanoscale to the mesoscale. In the synthesis method, GeS nanowires with axial screw dislocations are first grown along the stacking direction, yielding vdW nanowires with Eshelby twist. These wires possess continuous twists in which the total twist rates are defined by the radii of the nanowires, consistent with Eshelby's theory. Further radial growth of those twisted nanowires that are attached to the substrate leads to an increase in elastic energy, as the total twist rate is fixed by the substrate. The stored elastic energy can be reduced by accommodating the fixed twist rate in a series of discrete jumps in the twisting profile. This yields mesoscale twisting structures consisting of a helical assembly of nanoplates demarcated by atomically sharp interfaces with a range of twist angles.

The twisting morphology of the structures are tunable. We show that the twisting profile can be tailored by controlling the radial size of the structure. The twisting morphology gradually transitions from continuous twisting to intermediate twisting (consisting of both continuous twisting between the twist boundaries and discrete twisting at the boundaries) and eventually to discrete twisting with increasing radial size. This allows us to control the twisting profile and angles at twist interfaces by controlling the radial growth of the structure. The twist rates and periods of the structures are determined by the radii of the dislocated nanowires, which are defined by the size of the droplets catalyzing the VLS process. Our chemical analysis reveals that the growth of twisted GeS nanowires is catalyzed by the droplets of Au-Ge alloy. The size of the catalyst droplets was tailored by introducing GeSe into the growth. The addition of GeSe significantly increases the surface energy of the droplets, increasing the size of the droplets and therefore decreasing the twist rate of the structures. The chemical modulation of the droplet size is correlated with the change of germanium concentration (supersaturation) in the alloy droplets, consistent with the Gibbs-Thomson effect. The chemical modulation demonstrates good potential to tailor the twist rate and period of helical vdW crystals, enabling a new freedom to modulate optoelectronic properties and chiral light-matter interactions.

Last, we explored the anisotropic propagation of surface phonon polaritons in the GeS, motivated by the strong in-plane anisotropy of the crystal structure. Through semi-analytical transfer matrix analysis and numerical full-wave simulations, we demonstrate GeS films at thickness of tens of nanometers support strongly anisotropic SPhPs in far-infrared range. Two kinds of surface confined phonon polaritons namely hyperbolic SPhPs and elliptic SPhPs, are respectively identified in the frequency ranges of ~210-250 cm^{-1} and ~260-290 cm^{-1}. The hyperbolic SPhPs propagate along directions with limited angles with respect to the zigzag direction, over which there is no propagation of SPhPs. The elliptic SPhPs are also strongly

anisotropic, channeling as a narrow beam along the armchair direction. These SPhPs show strongly dependence on the film thickness. Surface phonon polaritons of the desired wavelength and confinement can be engineered by varying thickness of the film.

5.2 Outlook

The bottom-up scheme provides an approach to manipulate the twisting morphology and to realize defect engineering in vdW materials, providing new opportunities to tailor their electrical, optical and thermal properties. Through controlling the radial growth, atomically sharp twist interfaces with a wide and tunable range of twist angles can be created, providing ways to explore 'twistronic' effects in these materials. In contrast to planar and twisted structures, axial structures formed by helical stacking of atomic layers or nanoplates can have a large and modulated chiroptical response due to the periodicity and increased interaction length with light. The twisted nanowires could support optical modes with helical phase front. This enables generating light carrying orbital angular momentum (OAM), which can be used for optical communication and imaging.[87] Moreover, the axial screw dislocation spirally threads the vdW layers, which can improve the electron conductivity along the cross-plane direction[88]. The presence of the dislocation and the twist also enhance the scattering of phonons, lowering the thermal conductivity[89]. The combination of increasing electron conductivity while decreasing thermal conductivity is attractive for thermoelectrics.

The growth mode for the growth of twist GeS is likely to be generic and could be used to produce twisted structure in other vdW materials. In addition to GeS, other layer materials such as indium selenide(In_2Se_3) and bismuth selenide (Bi_2Se_3) have been reported to grow into nanowires with the growth direction to be the vdW stacking direction (cross-plane), akin to the GeS nanowires.[30,31] We could seek to grow these 2D materials into twisted form via the mechanism of Eshelby twist. Effort will be required to explore the optimal growth condition promoting the growth of the dislocated nanowires with growth direction to be along stacking direction.

References

(1) Kim, C.-J.; Sánchez-Castillo, A.; Ziegler, Z.; Ogawa, Y.; Noguez, C.; Park, J. Chiral atomically thin films. *Nature nanotechnology* **2016,** *11* (6), 520.

(2) Kim, K.; DaSilva, A.; Huang, S.; Fallahazad, B.; Larentis, S.; Taniguchi, T.; Watanabe, K.; LeRoy, B. J.; MacDonald, A. H.; Tutuc, E. Tunable moiré bands and strong correlations in small-twist-angle bilayer graphene. *Proceedings of the National Academy of Sciences* **2017,** *114* (13), 3364.

(3) Jin, C.; Regan, E. C.; Yan, A.; Utama, M. I. B.; Wang, D.; Zhao, S.; Qin, Y.; Yang, S.; Zheng, Z.; Shi, S. Observation of moiré excitons in WSe 2/WS 2 heterostructure superlattices. *Nature* **2019**, 1.

(4) Cao, Y.; Fatemi, V.; Demir, A.; Fang, S.; Tomarken, S. L.; Luo, J. Y.; Sanchez-Yamagishi, J.; Watanabe, K.; Taniguchi, T.; Kaxiras, E. Correlated insulator behaviour at half-filling in magic-angle graphene superlattices. *Nature* **2018**.

(5) Cao, Y.; Fatemi, V.; Fang, S.; Watanabe, K.; Taniguchi, T.; Kaxiras, E.; Jarillo-Herrero, P. Unconventional superconductivity in magic-angle graphene superlattices. *Nature* **2018,** *556* (7699), 43.

(6) Song, J. C.; Gabor, N. M. Electron quantum metamaterials in van der Waals heterostructures. *Nature nanotechnology* **2018,** *13* (11), 986.

(7) Yoo, H.; Engelke, R.; Carr, S.; Fang, S.; Zhang, K.; Cazeaux, P.; Sung, S. H.; Hovden, R.; Tsen, A. W.; Taniguchi, T. Atomic and electronic reconstruction at the van der Waals interface in twisted bilayer graphene. *Nature materials* **2019,** *18* (5), 448.

(8) Sharpe, A. L.; Fox, E. J.; Barnard, A. W.; Finney, J.; Watanabe, K.; Taniguchi, T.; Kastner, M. A.; Goldhaber-Gordon, D. Emergent ferromagnetism near three-quarters filling in twisted bilayer graphene. *Science* **2019,** *365* (6453), 605.

(9) Carr, S.; Massatt, D.; Fang, S.; Cazeaux, P.; Luskin, M.; Kaxiras, E. Twistronics: Manipulating the electronic properties of two-dimensional layered structures through their twist angle. *Physical Review B* **2017,** *95* (7), 075420.

(10) Kang, P.; Zhang, W.-T.; Michaud-Rioux, V.; Kong, X.-H.; Hu, C.; Yu, G.-H.; Guo, H. Moiré impurities in twisted bilayer black phosphorus: Effects on the carrier mobility. *Physical Review B* **2017,** *96* (19), 195406.

(11) Naik, M. H.; Jain, M. Ultraflatbands and Shear Solitons in Moir\'e Patterns of Twisted Bilayer Transition Metal Dichalcogenides. *Physical Review Letters* **2018,** *121* (26), 266401.

(12) Kennes, D.; Xian, L.; Claassen, M.; Rubio, A. A New Twist in the Realization of One-Dimensional Physics. *arXiv preprint arXiv:1905.04025* **2019**.

(13) Kim, K.; Yankowitz, M.; Fallahazad, B.; Kang, S.; Movva, H. C.; Huang, S.; Larentis, S.; Corbet, C. M.; Taniguchi, T.; Watanabe, K. van der Waals heterostructures with high accuracy rotational alignment. *Nano letters* **2016,** *16* (3), 1989.

(14) Pizzocchero, F.; Gammelgaard, L.; Jessen, B. S.; Caridad, J. M.; Wang, L.; Hone, J.; Bøggild, P.; Booth, T. J. The hot pick-up technique for batch assembly of van der Waals heterostructures. *Nature communications* **2016,** *7*, 11894.

(15) Ribeiro-Palau, R.; Zhang, C.; Watanabe, K.; Taniguchi, T.; Hone, J.; Dean, C. R. Twistable electronics with dynamically rotatable heterostructures. *Science* **2018,** *361* (6403), 690.

(16) Jin, C.; Regan, E. C.; Yan, A.; Utama, M. I. B.; Wang, D.; Zhao, S.; Qin, Y.; Yang, S.; Zheng, Z.; Shi, S. Observation of moiré excitons in WSe 2/WS 2 heterostructure superlattices. *Nature* **2019,** *567* (7746), 76.

(17) Shtukenberg, A. G.; Punin, Y. O.; Gujral, A.; Kahr, B. Growth actuated bending and twisting of single crystals. *Angewandte Chemie International Edition* **2014,** *53* (3), 672.

(18) Cordier, P.; Heidelbach, F. Origin of twist in 'gwindel'quartz crystals from the Alps: a transmission electron microscopy study. *European Journal of Mineralogy* **2013,** *25* (2), 145.
(19) Moloney, M. P.; Govan, J.; Loudon, A.; Mukhina, M.; Gun'ko, Y. K. Preparation of chiral quantum dots. *Nature protocols* **2015,** *10* (4), 558.
(20) Bierman, M. J.; Lau, Y. A.; Kvit, A. V.; Schmitt, A. L.; Jin, S. Dislocation-driven nanowire growth and Eshelby twist. *Science* **2008,** *320* (5879), 1060.
(21) Jin, S.; Bierman, M. J.; Morin, S. A. A new twist on nanowire formation: Screw-dislocation-driven growth of nanowires and nanotubes. *The Journal of Physical Chemistry Letters* **2010,** *1* (9), 1472.
(22) Zhu, J.; Peng, H.; Marshall, A.; Barnett, D.; Nix, W.; Cui, Y. Formation of chiral branched nanowires by the Eshelby Twist. *Nature nanotechnology* **2008,** *3* (8), 477.
(23) Tizei, L.; Craven, A.; Zagonel, L.; Tencé, M.; Stéphan, O.; Chiaramonte, T.; Cotta, M.; Ugarte, D. Enhanced Eshelby twist on thin wurtzite InP nanowires and measurement of local crystal rotation. *Physical review letters* **2011,** *107* (19), 195503.
(24) Eshelby, J. Screw dislocations in thin rods. *Journal of Applied Physics* **1953,** *24* (2), 176.
(25) Eshelby, J. The twist in a crystal whisker containing a dislocation. *Philosophical Magazine* **1958,** *3* (29), 440.
(26) Burton, W.-K.; Cabrera, N.; Frank, F. The growth of crystals and the equilibrium structure of their surfaces. *Phil. Trans. R. Soc. Lond. A* **1951,** *243* (866), 299.
(27) Wu, H.; Meng, F.; Li, L.; Jin, S.; Zheng, G. Dislocation-driven CdS and CdSe nanowire growth. *ACS nano* **2012,** *6* (5), 4461.
(28) Hacialioglu, S.; Meng, F.; Jin, S. Facile and mild solution synthesis of Cu 2 O nanowires and nanotubes driven by screw dislocations. *Chemical Communications* **2012,** *48* (8), 1174.
(29) Sutter, E.; Sutter, P. 1D Wires of 2D Layered Materials: Germanium Sulfide Nanowires as Efficient Light Emitters. *ACS Applied Nano Materials* **2017**.
(30) Peng, H.; Xie, C.; Schoen, D. T.; Cui, Y. Large anisotropy of electrical properties in layer-structured In2Se3 nanowires. *Nano letters* **2008,** *8* (5), 1511.
(31) Kong, D.; Randel, J. C.; Peng, H.; Cha, J. J.; Meister, S.; Lai, K.; Chen, Y.; Shen, Z.-X.; Manoharan, H. C.; Cui, Y. Topological insulator nanowires and nanoribbons. *Nano letters* **2009,** *10* (1), 329.
(32) Hsueh, H. C.; Li, J. X.; Ho, C. H. Polarization Photoelectric Conversion in Layered GeS. *Advanced Optical Materials* **2018,** *6* (4), 1701194.
(33) Tan, D.; Lim, H. E.; Wang, F.; Mohamed, N. B.; Mouri, S.; Zhang, W.; Miyauchi, Y.; Ohfuchi, M.; Matsuda, K. Anisotropic optical and electronic properties of two-dimensional layered germanium sulfide. *Nano Research* **2017,** *10* (2), 546.
(34) Ulaganathan, R. K.; Lu, Y.-Y.; Kuo, C.-J.; Tamalampudi, S. R.; Sankar, R.; Boopathi, K. M.; Anand, A.; Yadav, K.; Mathew, R. J.; Liu, C.-R. High photosensitivity and broad spectral response of multi-layered germanium sulfide transistors. *Nanoscale* **2016,** *8* (4), 2284.
(35) Tan, D.; Zhang, W.; Wang, X.; Koirala, S.; Miyauchi, Y.; Matsuda, K. Polarization-sensitive and broadband germanium sulfide photodetectors with excellent high-temperature performance. *Nanoscale* **2017,** *9* (34), 12425.
(36) Wu, M.; Zeng, X. C. Intrinsic ferroelasticity and/or multiferroicity in two-dimensional phosphorene and phosphorene analogues. *Nano letters* **2016,** *16* (5), 3236.
(37) Li, C.; Yu, Y.; Chi, M.; Cao, L. Epitaxial nanosheet–nanowire heterostructures. *Nano letters* **2013,** *13* (3), 948.
(38) Tamura, N.; London: Imperial College Press, 2014.
(39) Eshelby, J. D. Screw Dislocations in Thin Rods. *Journal of Applied Physics* **1953,** *24* (2), 176.
(40) Albrecht, M.; Lymperakis, L.; Neugebauer, J. Origin of the unusually strong luminescence of a-type screw dislocations in GaN. *Physical Review B* **2014,** *90* (24), 241201.
(41) Akatyeva, E.; Kou, L.; Nikiforov, I.; Frauenheim, T.; Dumitrica, T. Electrically active screw dislocations in helical ZnO and Si nanowires and nanotubes. *ACS nano* **2012,** *6* (11), 10042.
(42) Ertekin, E.; Greaney, P. A.; Chrzan, D.; Sands, T. D. Equilibrium limits of coherency in strained nanowire heterostructures. *Journal of Applied Physics* **2005,** *97* (11), 114325.

(43) Lothe, J. P. H. a. J. *Theory of dislocations*; Krieger Pub. Co., 1992., 1992.
(44) Eshelby, J.; Read, W.; Shockley, W. Anisotropic elasticity with applications to dislocation theory. *Acta metallurgica* **1953,** *1* (3), 251.
(45) Foreman, A. Dislocation energies in anisotropic crystals. *Acta metallurgica* **1955,** *3* (4), 322.
(46) De Jong, M.; Chen, W.; Angsten, T.; Jain, A.; Notestine, R.; Gamst, A.; Sluiter, M.; Ande, C. K.; Van Der Zwaag, S.; Plata, J. J. Charting the complete elastic properties of inorganic crystalline compounds. *Scientific data* **2015,** *2*, 150009.
(47) Liu, Y.; Wang, J.; Kim, S.; Sun, H.; Yang, F.; Fang, Z.; Tamura, N.; Zhang, R.; Song, X.; Wen, J.et al. Helical van der Waals crystals with discretized Eshelby twist. *Nature* **2019,** *570* (7761), 358.
(48) Dayeh, S. A.; Picraux, S. Direct observation of nanoscale size effects in Ge semiconductor nanowire growth. *Nano letters* **2010,** *10* (10), 4032.
(49) Biswas, S.; O'Regan, C.; Petkov, N.; Morris, M. A.; Holmes, J. D. Manipulating the growth kinetics of vapor–liquid–solid propagated Ge nanowires. *Nano letters* **2013,** *13* (9), 4044.
(50) Han, N.; Wang, F.; Hou, J. J.; Yip, S.; Lin, H.; Fang, M.; Xiu, F.; Shi, X.; Hung, T.; Ho, J. C. Manipulated growth of GaAs nanowires: controllable crystal quality and growth orientations via a supersaturation-controlled engineering process. *Crystal Growth & Design* **2012,** *12* (12), 6243.
(51) Dubrovskii, V.; Sibirev, N.; Cirlin, G.; Soshnikov, I.; Chen, W.; Larde, R.; Cadel, E.; Pareige, P.; Xu, T.; Grandidier, B. Gibbs-Thomson and diffusion-induced contributions to the growth rate of Si, InP, and GaAs nanowires. *Physical Review B* **2009,** *79* (20), 205316.
(52) Kashchiev, D. Dependence of the growth rate of nanowires on the nanowire diameter. *Crystal growth & design* **2006,** *6* (5), 1154.
(53) Peng, H.; Meister, S.; Chan, C. K.; Zhang, X. F.; Cui, Y. Morphology Control of Layer-Structured Gallium Selenide Nanowires. *Nano Lett* **2007,** *7* (1), 199.
(54) Ek, M.; Filler, M. A. Atomic-Scale Choreography of Vapor–Liquid–Solid Nanowire Growth. *Acc. Chem. Res* **2018,** *51* (1), 118.
(55) Kratzer, P.; Sakong, S.; Pankoke, V. Catalytic Role of Gold Nanoparticle in GaAs Nanowire Growth: A Density Functional Theory Study. *Nano Lett* **2012,** *12* (2), 943.
(56) Chen, X.; Liu, R.; Qiao, S.; Mao, J.; Du, X. Synthesis of cadmium chalcogenides nanowires via laser-activated gold catalysts in solution. *Mater. Chem. Phys* **2018,** *212*, 408.
(57) Sutter, E.; Sutter, P. 1D Wires of 2D Layered Materials: Germanium Sulfide Nanowires as Efficient Light Emitters. *ACS Appl. Nano. Mater* **2018,** *1* (3), 1042.
(58) Lotty, O.; Hobbs, R.; O'Regan, C.; Hlina, J.; Marschner, C.; O'Dwyer, C.; Petkov, N.; Holmes, J. D. Self-Seeded Growth of Germanium Nanowires: Coalescence and Ostwald Ripening. *Chem. Mater* **2013,** *25* (2), 215.
(59) Liu, Y.; Wang, J.; Kim, S.; Sun, H.; Yang, F.; Fang, Z.; Tamura, N.; Zhang, R.; Song, X.; Wen, J. Helical van der Waals crystals with discretized Eshelby twist. *Nature* **2019,** *570* (7761), 358.
(60) Chen, Y.; Dumcenco, D. O.; Zhu, Y.; Zhang, X.; Mao, N.; Feng, Q.; Zhang, M.; Zhang, J.; Tan, P.-H.; Huang, Y.-S. Composition-dependent Raman modes of Mo1− xWxS2 monolayer alloys. *Nanoscale* **2014,** *6* (5), 2833.
(61) Zhang, M.; Wu, J.; Zhu, Y.; Dumcenco, D. O.; Hong, J.; Mao, N.; Deng, S.; Chen, Y.; Yang, Y.; Jin, C. Two-dimensional molybdenum tungsten diselenide alloys: photoluminescence, Raman scattering, and electrical transport. *ACS nano* **2014,** *8* (7), 7130.
(62) Vegard, L. Die konstitution der mischkristalle und die raumfüllung der atome. *Zeitschrift für Physik A Hadrons and Nuclei* **1921,** *5* (1), 17.
(63) Caldwell, J. D.; Lindsay, L.; Giannini, V.; Vurgaftman, I.; Reinecke, T. L.; Maier, S. A.; Glembocki, O. J. Low-loss, infrared and terahertz nanophotonics using surface phonon polaritons. *Nanophotonics* **2015,** *4* (1), 44.
(64) Maier, S. A. *Plasmonics: fundamentals and applications*; Springer Science & Business Media, 2007.
(65) Chen, D.-Z. A.; Narayanaswamy, A.; Chen, G. Surface phonon-polariton mediated thermal conductivity enhancement of amorphous thin films. *Physical Review B* **2005,** *72* (15), 155435.

(66) Shen, S.; Narayanaswamy, A.; Chen, G. Surface phonon polaritons mediated energy transfer between nanoscale gaps. *Nano letters* **2009,** *9* (8), 2909.
(67) Taubner, T.; Korobkin, D.; Urzhumov, Y.; Shvets, G.; Hillenbrand, R. Near-field microscopy through a SiC superlens. *Science* **2006,** *313* (5793), 1595.
(68) Greffet, J.-J.; Carminati, R.; Joulain, K.; Mulet, J.-P.; Mainguy, S.; Chen, Y. Coherent emission of light by thermal sources. *Nature* **2002,** *416* (6876), 61.
(69) Tranchant, L.; Hamamura, S.; Ordonez-Miranda, J.; Yabuki, T.; Vega-Flick, A.; Cervantes-Alvarez, F.; Alvarado-Gil, J. J.; Volz, S.; Miyazaki, K. Two-Dimensional Phonon-Polariton Heat Transport. *Nano letters* **2019**.
(70) St-Gelais, R.; Zhu, L.; Fan, S.; Lipson, M. Near-field radiative heat transfer between parallel structures in the deep subwavelength regime. *Nature nanotechnology* **2016,** *11* (6), 515.
(71) Huber, A.; Deutsch, B.; Novotny, L.; Hillenbrand, R. Focusing of surface phonon polaritons. *Applied Physics Letters* **2008,** *92* (20), 203104.
(72) Poddubny, A.; Iorsh, I.; Belov, P.; Kivshar, Y. Hyperbolic metamaterials. *Nature photonics* **2013,** *7* (12), 948.
(73) Dai, S.; Fei, Z.; Ma, Q.; Rodin, A.; Wagner, M.; McLeod, A.; Liu, M.; Gannett, W.; Regan, W.; Watanabe, K. Tunable phonon polaritons in atomically thin van der Waals crystals of boron nitride. *Science* **2014,** *343* (6175), 1125.
(74) Jacob, Z. Nanophotonics: hyperbolic phonon–polaritons. *Nature materials* **2014,** *13* (12), 1081.
(75) Basov, D.; Fogler, M.; De Abajo, F. G. Polaritons in van der Waals materials. *Science* **2016,** *354* (6309), aag1992.
(76) Li, P.; Lewin, M.; Kretinin, A. V.; Caldwell, J. D.; Novoselov, K. S.; Taniguchi, T.; Watanabe, K.; Gaussmann, F.; Taubner, T. Hyperbolic phonon-polaritons in boron nitride for near-field optical imaging and focusing. *Nature communications* **2015,** *6*, 7507.
(77) Dai, S.; Ma, Q.; Andersen, T.; Mcleod, A.; Fei, Z.; Liu, M.; Wagner, M.; Watanabe, K.; Taniguchi, T.; Thiemens, M. Subdiffractional focusing and guiding of polaritonic rays in a natural hyperbolic material. *Nature communications* **2015,** *6*, 6963.
(78) Caldwell, J. D.; Kretinin, A.; Chen, Y.; Giannini, V.; Fogler, M. M.; Francescato, Y.; Ellis, C. T.; Tischler, J. G.; Woods, C. R.; Giles, A. J. Sub-diffractional, volume-confined polaritons in a natural hyperbolic material: hexagonal boron nitride. *Nature communications* **2014,** *5*.
(79) Tielrooij, K.-J.; Hesp, N. C.; Principi, A.; Lundeberg, M. B.; Pogna, E. A.; Banszerus, L.; Mics, Z.; Massicotte, M.; Schmidt, P.; Davydovskaya, D. Out-of-plane heat transfer in van der Waals stacks through electron–hyperbolic phonon coupling. *Nature nanotechnology* **2018,** *13* (1), 41.
(80) Gomez-Diaz, J.; Alu, A. Flatland optics with hyperbolic metasurfaces. *ACS Photonics* **2016,** *3* (12), 2211.
(81) Ma, W.; Alonso-González, P.; Li, S.; Nikitin, A. Y.; Yuan, J.; Martín-Sánchez, J.; Taboada-Gutiérrez, J.; Amenabar, I.; Li, P.; Vélez, S. In-plane anisotropic and ultra-low-loss polaritons in a natural van der Waals crystal. *Nature* **2018,** *562* (7728), 557.
(82) Wiley, J.; Buckel, W.; Schmidt, R. Infrared reflectivity and Raman scattering in GeS. *Physical Review B* **1976,** *13* (6), 2489.
(83) Yu, L.-M.; Degiovanni, A.; Thiry, P.; Ghijsen, J.; Caudano, R.; Lambin, P. Infrared optical constants of orthorhombic IV-VI lamellar semiconductors refined by a combined study using optical and electronic spectroscopies. *Physical Review B* **1993,** *47* (24), 16222.
(84) Rumpf, R. C. Improved formulation of scattering matrices for semi-analytical methods that is consistent with convention. *Progress In Electromagnetics Research* **2011,** *35*, 241.
(85) Correas-Serrano, D.; Gomez-Diaz, J.; Melcon, A. A.; Alù, A. Black phosphorus plasmonics: anisotropic elliptical propagation and nonlocality-induced canalization. *Journal of Optics* **2016,** *18* (10), 104006.
(86) Nemilentsau, A.; Low, T.; Hanson, G. Anisotropic 2D materials for tunable hyperbolic plasmonics. *Physical review letters* **2016,** *116* (6), 066804.

(87) Zhang, Y.; Bai, Z.; Fu, C.; Liu, S.; Tang, J.; Yu, J.; Liao, C.; Wang, Y.; He, J.; Wang, Y. Polarization-independent orbital angular momentum generator based on a chiral fiber grating. *Optics letters* **2019,** *44* (1), 61.
(88) Ly, T. H.; Zhao, J.; Kim, H.; Han, G. H.; Nam, H.; Lee, Y. H. Vertically conductive MoS2 spiral pyramid. *Advanced Materials* **2016,** *28* (35), 7723.
(89) Al-Ghalith, J.; Ni, Y.; Dumitrică, T. Nanowires with dislocations for ultralow lattice thermal conductivity. *Physical Chemistry Chemical Physics* **2016,** *18* (15), 9888.